Aachener Verfahrenstechnik Series
AVT.CVT – Chemical Process Engineering
Volume 50 (2025)

Lea Maria Steinbeck

Tailoring the Characteristics of Complex-Shaped Microgels

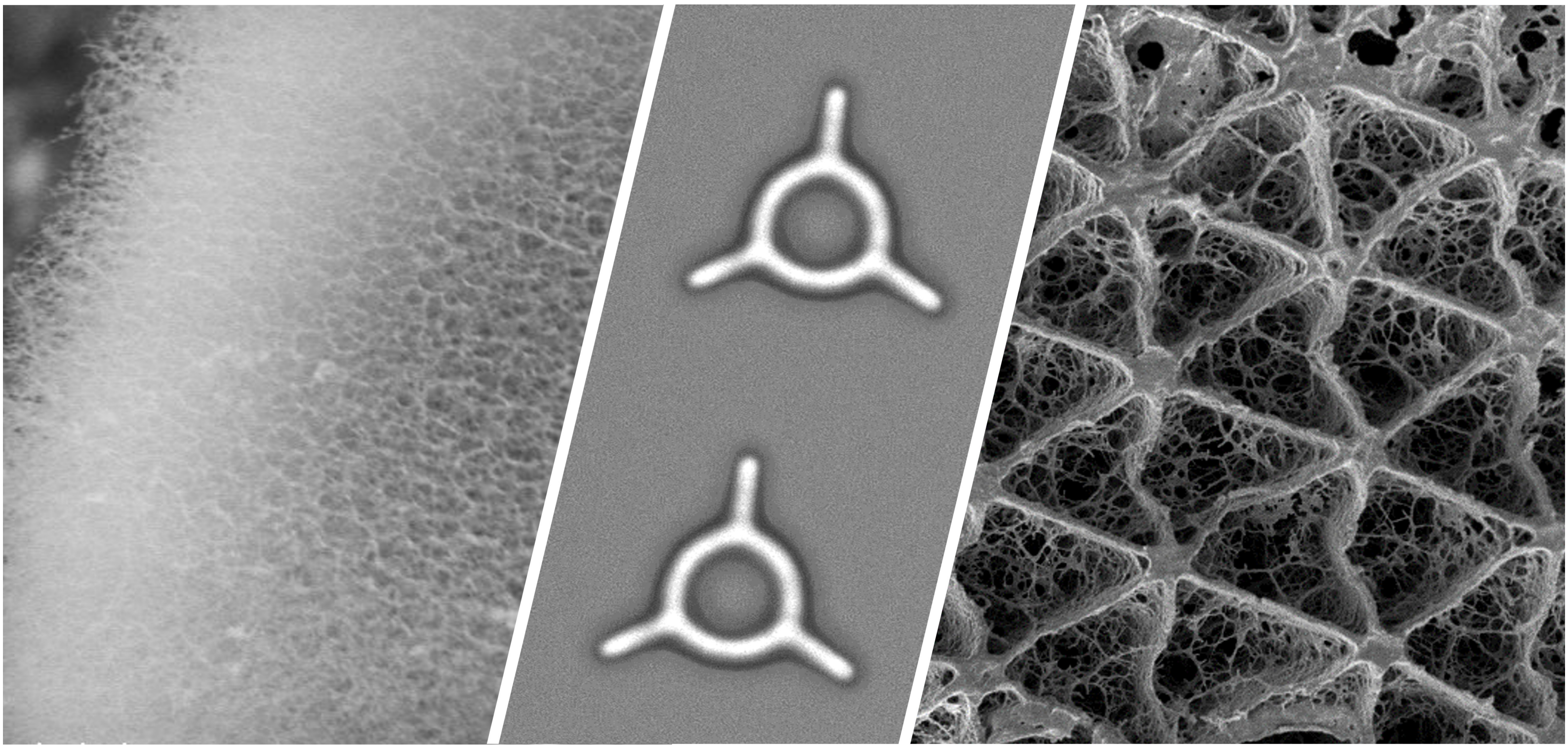

Tailoring the Characteristics of Complex-Shaped Microgels

Gezielte Einstellung der Eigenschaften komplex geformter Mikrogele

Von der Fakultät für Maschinenwesen
der Rheinisch-Westfälischen Technischen Hochschule Aachen
zur Erlangung des akademischen Grades
einer Doktorin der Ingenieurwissenschaften
genehmigte Dissertation

vorgelegt von

Lea Maria Steinbeck

Berichter/in:
Univ.-Prof. Dr.-Ing. Matthias Wessling
Univ.-Prof. Dr.-Ing. Laura De Laporte

Tag der mündlichen Prüfung: 13.02.2025

Parts of this dissertation have been published. Reproduced with permission from:

Lea Steinbeck, Dominik L. Braunmiller, Hanna J. M. Wolff, Vincent Hüttche, Julia Wang, Matthias Wessling, Jérôme J. Crassous, John Linkhorst
Magnetically Actuable Complex-Shaped Microgels for Spatio-Temporal Flow Control, Advanced Materials Technologies, 2023
DOI: 10.1002/admt.202300044

Lea Steinbeck, Hanna J. M. Wolff, Maximilian Middeldorf, John Linkhorst, Matthias Wessling,
Porous Anisometric PNIPAM Microgels: Tailored Porous Structure and Thermal Response, Macromolecular Rapid Communications, 2024
DOI: 10.1002/marc.202300680

Lea Steinbeck, Richard Paul, Julia Litke, Isabel Karkoszka, G. Philip Wiese, John Linkhorst, Laura De Laporte, Matthias Wessling,
Hierarchically Structured and Tunable Hydrogel Patches: Design, Characterization, and Application, SMALL, 2024
DOI: 10.1002/smll.202407311

Titel: Tailoring the Characteristics of Complex-Shaped Microgels

Gezielte Einstellung der Eigenschaften komplex geformter Mikrogele

Autor: Lea Maria Steinbeck

Reihe: Aachener Verfahrenstechnik Series
AVT.CVT - Chemical Process Engineering
Volume 50 (2025)

Herausgeber: Aachener Verfahrenstechnik
Forckenbeckstraße 51
52074 Aachen
Tel.: +49 (0)241 8095470
Fax.: +49 (0)241 8092252
E-Mail: secretary.cvt@avt.rwth-aachen.de
www.avt.rwth-aachen.de/AVT

Volltext verfügbar: 10.18154/RWTH-2025-03604

Acknowledgement

Die Fertigstellung meiner Dissertation erfüllt mich mit Freude, Stolz und Dankbarkeit. Ohne die Menschen um mich herum wäre dieser Schritt nicht möglich gewesen.

Dafür möchte ich mich zu aller erst bei meinem betreuendem Professor Matthias Wessling bedanken, insbesondere für sein Vertrauen in meine Arbeit und die damit verbundene Freiheit, die ich während meiner Forschung genießen durfte. Außerdem danke ich Laura De Laporte als Zweitgutachterin meiner Dissertation, die mir zusätzlich mit ihrem Rat zur Seite stand. John Linkhorst danke ich dafür, dass er mir ein verlässlicher Ansprechpartner war und stets hilfreichen Input für meine Forschungsideen parat hatte. Bei Georg, Arne und Hanna möchte ich mich für ihre Betreuung zu Studi- und Newbie-Tagen bedanken und, dass sie mich für die Promotion motiviert haben. Meinen Kolleg:innen und mittlerweile Freund:innen am Lehrstuhl für Chemische Verfahrenstechnik danke ich für ihre Beratung, Unterstützung und das einzigartige Arbeitsklima, das mich bereits als Studentin begeistert hatte. Zusätzlich möchte ich mich bei allen Festangestellten der CVT bedanken, die die Konstante des Lehrstuhls sind. Danke an die Laboranten und die Teams der IT, Werkstatt, E-Werkstatt, Buchhaltung und des Sekretariats für ihre oft unsichtbare aber essenzielle Hintergrundarbeit. Dabei möchte ich Susanne Offermann besonders hervorheben für ihre Hilfsbereitschaft und ihre wichtige Weitsicht im Hinblick auf die zwischenmenschliche Komponente am Lehrstuhl. Allen anderen Kooperationspartnern, den Kursleitenden zahlreicher Weiterbildungsprogramme und den anderen Promovierenden des TandemDok Programms danke ich für ihren Anteil an meiner persönlichen Weiterentwicklung und Fertigstellung dieser Dissertation. Auch wenn nicht alle Studierendenarbeiten in dieser Dissertation inhaltliche Erwähnung finden, haben alle Studierenden, die ich betreuen durfte, einen Anteil an dieser Arbeit geleistet, weshalb ich gerne allen von ihnen danken möchte.

Der letzte und persönlichste Dank gilt meiner Familie und meinen Freund:innen, allen voran meiner Mutter und Flo. Danke für eure bedingungslose Unterstützung, ermutigenden Worte und die Kraft und den Halt, den ihr mir gebt. Dabei spielt Flo eine ganz besondere Rolle, sowohl als mein Kollege als auch als mentale Stütze, Motivationsredner und größter Unterstützer.

Danke!

Contents

Abstract

Microgels are micrometer-sized polymer networks swollen in water or a similar solvent. They are used in various areas, such as water treatment, soft robotics, and tissue engineering. In order to fully exploit the potential of microgels, their properties need to be precisely adjusted in line with their application. In this regard, non-spherical microgels attract increasing interest as they extend the microgels' properties through their anisometry. However, fabricating complex-shaped anisometric microgels is still more challenging than producing spherical ones and, therefore, much rarer. This thesis examines the fabrication of such complex-shaped microgels and the customization of selected microgel characteristics. The aim is to establish a fabrication platform with a repertoire of tailorable microgel characteristics that enables the combination and reliable regulation of the properties of a microgel.

Stop-flow lithography (SFL) served as a fabrication method for complex-shaped microgels. This fabrication was modified in this thesis to tailor the characteristics of the microgels. The porous structure of the microgels was altered by using a cononsolvent in the reaction solution, which changed the polymer interactions during polymerization. This altered microgel structure influenced the thermal response of the poly(*N*-isopropyl acrylamide) (PNIPAM) microgels. These showed a significantly higher collapsing degree, modified collapsing and swelling kinetics, and inhomogeneous patterns during the swelling process. Adding ellipsoidal magnetic nanoparticles to the reaction solution resulted in magnetic microgels. By aligning the nanoparticles prior to polymerization, the microgels possessed a pre-defined magnetic moment, determining their alignment direction in a magnetic field. This alignment allowed the microgels to rotate in solution or rotate fixed in a microfluidic channel, actively mixing the surrounding solution. The limits of microgel fabrication via radical projection lithography have been exploited to create so-called patches with a novel technique. The patches are millimeter-sized hydrogels with highly crosslinked features connected to each other by a weaker crosslinked and flatter polymer network. The exact geometry, porosity, mechanical stability, and other properties of these patches can be adjusted.

This work shows how porosity, thermal response, magnetic actuation, and architecture of complex-shaped microgels can be precisely tuned via SFL fabrication. Thus, microgel characteristics can be extended and better tailored, which enables customization for future applications of microgels, such as scaffolds for tissue engineering, which are one of their most promising applications.

Zusammenfassung

Mikrogele sind mikrometergroße Polymernetzwerke, die in Wasser oder einem ähnlichen Lösungsmittel gequollen vorliegen. Sie finden Anwendung in diversen Bereichen wie der Wasseraufbereitung, der Robotik (soft robotics) oder der Gewebezüchtung. Um das Potential der Mikrogele voll ausschöpfen zu können, ist es wichtig, ihre Eigenschaften präzise und anwendungsbezogen einstellen zu können. Insbesondere nichtkugelförmige Mikrogele haben an Interesse gewonnen, da diese durch ihre Anisometrie die Eigenschaften der Mikrogele erweitern. Die Herstellung komplex geformter anisometrischer Mikrogele ist jedoch weiterhin herausfordernder und damit deutlich seltener. Diese Arbeit befasst sich mit der Herstellung solcher komplex geformter Mikrogele und der gezielten Anpassung ausgewählter Mikrogeleigenschaften. Dabei soll eine Herstellungsplattform mit einem Repertoire an einstellbaren Mikrogeleigenschaften aufgebaut werden, die die Kombination der Eigenschaften in einem Mikrogel ermöglicht.

Stop-Flow Lithographie (SFL) diente zur Herstellung der komplex geformten Mikrogele, welche im Rahmen der Arbeit angepasst wurde, um die Eigenschaften der Mikrogele gezielt einzustellen. Die poröse Struktur der Mikrogele wurde verändert, indem eine Mischung aus zwei Lösungsmitteln in der Reaktionslösung verwendet wurde, in der das Polymer nicht löslich ist und die somit für veränderte Polymerinteraktionen während der Polymerisation führte. Diese veränderte Mikrogelstruktur beeinflusste zusätzlich die thermische Reaktion der Poly(*N*-Isopropylacrylamid) (PNIPAM) Mikrogele. Diese zeigten einen deutlich stärkeren Kollabierungsgrad, eine veränderte Kollabierungs- und Quellungskinetik und interne Polymermuster während des Quellvorgangs. Durch das Hinzufügen von elliptischen, magnetischen Nanopartikeln zur Reaktionslösung wurden magnetische Mikrogele hergestellt. Durch die Ausrichtung der Nanopartikel vor der Polymerisation besaßen die Mikrogele ein gerichtetes magnetisches Moment, anhand dessen sie sich in einem magnetischen Feld ausrichteten. Diese Ausrichtung ermöglichte die Rotation der Mikrogele, sowohl in Lösung als auch räumlich fixiert in einem mikrofluidischen Kanal zur Durchmischung der umgebenden Lösung. Die Grenzen der Mikrogelherstellung über radikalische Projektionslithographie wurden ausgenutzt, um in einem neuen Verfahren so genannte Patches zu erschaffen. Dabei handelt es sich um millimetergroße Hydrogele mit stark vernetzten Polymerregionen, die durch ein schwächer vernetztes und niedrigeres Polymernetzwerk miteinander verbunden sind. Die exakte Geometrie, die Porosität, die mechanische Stabilität und weitere Eigenschaften dieser Patches können spezifisch angepasst werden.

Diese Arbeit zeigt wie Porosität, thermische Reaktion, magnetische Aktuierung und geometrische Strukturierung von komplex geformten Mikrogelen gezielt über SFL eingestellt werden können. Damit können Mikrogeleigenschaften erweitert und besser eingestellt werden, was ein Maßschneidern für zukünftige Anwendungen der Mikrogele ermöglicht, beispielsweise als Gerüststrukturen für die Gewebezüchtung als eine der vielversprechendsten Anwendungen.

1 Introduction

1.1 Microgels and Their Applications

In the last decades, the research interest in hydrogels has been and is still enormous. This interest is based on their responsive, tunable, and biocompatible nature, rendering them suitable for various applications, particularly in the biomedical field. [Alke2021] Hydrogels are three-dimensional polymer networks that are highly swollen in water and familiar solvents and occur in various sizes. Hydrogels in the micrometer scale are defined as microgels. [Alza2021] The characteristics of microgels depend on their polymer network and can be adjusted and expanded, for example, by copolymerization of more than one polymer kind or by integration of covalently or physically attached additives. Tailoring the characteristics of microgels broadens their possible applications and customizes their use. [Karg2019; Baro2006]

Microgels address various application fields like soft robotics, sensors, bioimaging, wound dressing, emulsifiers, and wastewater treatment, among others. [Thor2011; Fu2019] The probably largest and most researched field of application of microgels is their biomedical use. Several biomedical applications have been investigated and demonstrated in the literature, ranging from cell imaging over immunoassays to drug delivery. In the medical and bio-engineering field, regenerating damaged tissue with the help of biological substitutes has gained high interest over the last decades. This field is called tissue engineering and aims to construct artificial tissues based on cultured cells. Since microgels exhibit similar properties as natural tissue, their use as scaffolds for cells in tissue engineering represents one major biomedical application of microgels: repairing or replacing damaged tissues. In the literature, suitable materials have been invented and extensively studied to address the needs of the cells. However, the ongoing research field still lacks a full understanding of these cell needs and accurate cell-scaffold interactions. [Chir2015; Liu2024; News2019; OBri2011]

When applied as cell scaffolds, microgels must fulfill certain mandatory criteria, such as biocompatibility, nutrient supply, and void space for cell growth. Their porous structure allows the efficient mass transfer of oxygen, nutrients, growth factors, and metabolic products, supporting cell growth, proliferation, and differentiation. Cell-material interactions and cell adhesion must be assured by the scaffolds as the basis for tissue formation. Furthermore, mechanical stability needs to be considered during scaffold design. In addition to influencing tissue growth, this stability allows injection of the tissue to desired locations by minimally invasive insertion or implantation. The architecture and topography of scaffolds mimic the cellular microenvironment and guide multicellular processes. [OBri2011; Babu2021; Janm2020]

Mammalian cells are highly specialized, resulting in deviating demands on the scaffold dependent on the origin and function of the tissue. To address the individual criteria of various tissues, the microgel scaffold must be tunable to these characteristics, such as porosity, stability, or geometry. Additionally, depending on the desired functionality of the scaffold, its response to external stimuli needs to be implementable by material adaption or additive integration. To achieve this tailoring of microgels, the microgel materials and their fabrication with customized properties are extensively explored. [OBri2011; El-S2013]

1.2 Fabrication

The fabrication of microgels mainly determines their characteristics. The choice of incorporated polymer provides the basis, and the reaction mechanism and the fabrication method impact the polymeric structure of the microgels. The fabrication method further defines the shape of the microgels. Hence, controlling the fabrication of microgels enables tailoring their characteristics. Complex-shaped microgels benefit in various applications over classically spherical microgels and are particularly addressed in this thesis. [Liu2024]

1.2.1 Polymers

Microgels are not limited to one material but comprise several polymers that can be natural or synthetic. The advantages of natural polymers are their high biological acceptance and physiological cell interactions. In contrast, synthetic polymers are often highly chemically stable and more versatile in terms of their tuning abilities. Some exemplary and often used materials for microgel fabrication are the native polymers alginate, collagen, and agarose and the synthetic polymers poly(ethylene glycol) (PEG), poly(*N*-isopropyl acrylamide) (PNIPAM), and poly(*N*-vinyl caprolactam) (PVCL). [Alza2021; Gera2023]

Particularly, PEG and PNIPAM are some of the most studied and common microgel polymers. PEG is proven to be highly biocompatible and well-established. For the fabrication of PEG-based microgels, typically, the pre-polymer poly(ethylene glycol) diacrylate (PEGDA) is crosslinked. [Deut2024] The structural formula of PEGDA is shown in Figure 1.1. PNIPAM microgels are widely spread due to their thermo-responsiveness. These microgels collapse when they exceed a certain temperature. When being cooled again, PNIPAM microgels swell and regain their initial volume (see

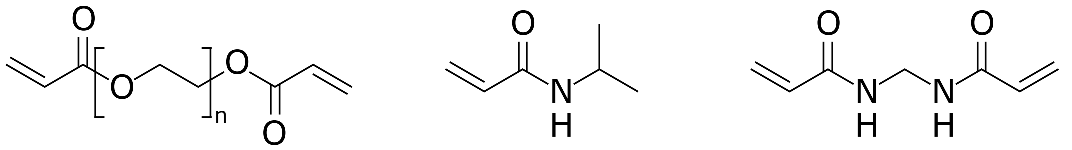

Poly(ethylene glycol) diacrylate
(PEGDA)

N-Isopropyl acrylamide
(NIPAM)

N, *N*'-Methylene bisacrylamide
(BIS)

Figure 1.1: Structural formula of the pre-polymer PEGDA, the monomer NIPAM, and its commonly used crosslinker BIS.

Section 1.3.2 for detailed information on thermo-responsiveness). [Pich2010; Haq2017]

In contrast to PEGDA-based microgels, PNIPAM microgels need a crosslinker to achieve a crosslinked polymer network since the monomer NIPAM only has one reactive double bond in its acrylamide group (CH_2=CH–CONH-R) (compare Figure 1.1). Hence, NIPAM molecules form polymer chains but cannot form crosslinked polymer networks alone. Therefore, molecules with two acrylate groups (CH_2=CH–COOR) like PEGDA are needed or the crosslinker *N*, *N*'-methylene bisacrylamide (BIS), which is commonly added to NIPAM for microgel fabrication. BIS has two acrylamide groups (compare Figure 1.1) and crosslinks polymer chains within the microgel network without majorly influencing the characteristics of the arisen microgel when added in a small quantity. To facilitate the polymerization of both material systems, the reactions have to be initiated. Therefore, an initiator is added to the pre-polymer molecules, which can be activated by an external stimulus like temperature or light. Polymerization reactions based on light-induced initiation are called photopolymerization reactions. [Alza2021; Dend2008]

1.2.2 Free-Radical Photopolymerization

Polymerization methods to convert pre-polymer molecules into microgels are versatile. Photopolymerization is a process that provides significant advantages over other methods, such as mild solvent-free reaction conditions at room temperature and atmospheric pressures, rapid curing, and high resolution of defined, complex microgel shapes. Photoinitiation, which starts these polymerization reactions, may be based on cationic systems or free-radical initiation. [Dend2008; Baro2006] In this thesis, the focus lies on free-radical photopolymerization.

Both material systems, PEGDA and NIPAM with BIS, can be initiated by light if a photo-inducible initiator is used. Lithium phenyl-2,4,6-trimethylbenzoyl phosphinate (LAP) is a possible photo-initiator activated at UV light, as shown in Figure 1.2. LAP shows higher reaction rates at the commonly used 365 nm wavelength than other photoinitiators such as I2959 or Darocur 1173. Additionally, LAP shows better water solubility and can be activated by visible light as well, which can be beneficial for synthesizing cell-encapsulated materials. [Fair2009; Wolf2021]

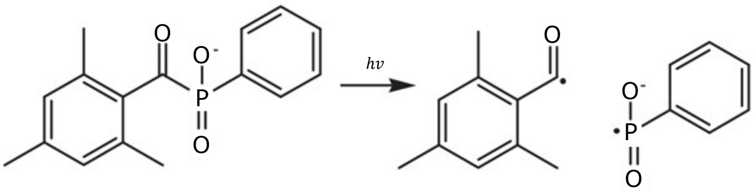

Figure 1.2: Initiation reaction of LAP using UV light. Adapted from [Fair2009].

By reacting with photons of light, the photo-initiator (PI) LAP forms highly reactive free radicals ($\dot{\mathrm{R}}$) due to photo-induced cleavage of a bond, which is the first mechanism step called photolysis. The basic reaction steps of the simplified reaction mechanism to describe free-radical photopolymerization are displayed in Table 1.1. The radicals originating from the PI initiate the polymer chain growth by reacting with a double bond in the acrylate group of one of the pre-polymer molecules (M) PEGDA, NIPAM, or BIS. As a result, a reactive radical intermediate ($\mathrm{R\dot{M}}$) forms, representing the initiation step of chain polymerization. PEGDA and BIS, which exhibit two reactive

Table 1.1: Reaction mechanism of free-radical photopolymerization with PI as photoinitiator, $\dot{\mathrm{R}}$ as radicals, M as pre-polymer molecule, $\mathrm{R\dot{M}}_i$ as reactive radical intermediates, $\mathrm{RM}_n\mathrm{M}_m$ as nonreactive polymer chain, and $\mathrm{RM}_n\mathrm{OO}$ as nonreactive oxidized entity. [Dend2008]

no.	reaction	mechanism step
1	$\mathrm{PI} \xrightarrow{hv} \dot{\mathrm{R}}$	photolysis
2	$\dot{\mathrm{R}} + \mathrm{M} \longrightarrow \mathrm{R\dot{M}}$	chain initiation
3	$\mathrm{R\dot{M}}_n + \mathrm{M} \xrightarrow{k_\mathrm{p}} \mathrm{R\dot{M}}_{n+1}$	chain propagation
4	$\mathrm{R\dot{M}}_n + \mathrm{R\dot{M}}_m \xrightarrow{k_\mathrm{t}} \mathrm{RM}_n\mathrm{M}_m$	chain termination
5	$\mathrm{R\dot{M}}_n + \mathrm{O}_2 \xrightarrow{k_\mathrm{o}} \mathrm{RM}_n\mathrm{OO}$	inhibition

groups on each molecule, enable two reaction sides and, thus, crosslinking reactions that result in solid polymer networks. The chain propagation proceeds by a further reaction with a pre-polymer molecule, forming a larger radical and a growing polymeric chain, in which the double bonds convert into two single bonds connecting the pre-polymers. Chain termination occurs if two radical species react with each other into a nonreactive polymer chain $\mathrm{RM}_n\mathrm{M}_m$, neglecting other kinds of termination in this simplified representation. [Dend2008] In addition to the reactions leading to polymer formation, the free-radical polymerization is inhibited by molecular oxygen. The oxygen reacts with reactive radical intermediates of a growing chain and forms nonreactive oxidized entities ($\mathrm{RM}_n\mathrm{OO}$), or it may quench the excited state of the initiator. Hence, the oxygen terminates or even prevents the acrylate polymerization. Especially in the initial reaction times, oxygen crucially inhibits the polymerization. [Dend2008; Ligo2014; Haki2014] However, oxygen inhibition can be advantageous, especially for microfluidic fabrication methods based on free-radical photopolymerization.

1.2.3 Stop-Flow Lithography

Microgels are fabricated using several diverse methods. The number of methods narrows down when fabricating non-spherical microgels on a micron scale, resulting in mostly photo-induced fabrication methods. [Liu2024; Tian2020] Stop-flow lithography (SFL) is one of these methods and a specialized form of microfluidic projection lithography, which was first reported by Dendukuri et al. [Dend2007b].

The basic principle of SFL is visualized in Figure 1.3. The photo-inducible precursor solution flows into a microfluidic channel by applying pressure on the inlet. Then, the solution is stopped by closing a valve between the pressure source and the microfluidic channel. Wolff et al. [Wolf2020] published a slightly adapted SFL setup compared to the first one of Dendukuri et al. [Dend2007b], for example, distinguishing by applying pressure on the in- and outlet instead of the inlet only. As soon as the solution is settled, the solution is exposed to UV light by opening a shutter [Dend2007b] or turning the light source on [Wolf2020], depending on the respective setup. The exposure areas are defined by a transparency mask positioned between the light source and the microfluidic channel. Afterward, the flow is activated again, flushing the arisen microgels out of the exposure area. This cycle of *stop*, *polymerize*, and *flow* (compare Figure 1.3b) is automatically repeated until the desired amount of microgels is achieved. Repeating this cycle allows the fabrication of microgels with any elongated 2D shape in high throughput. [Dend2007b; Wolf2020]

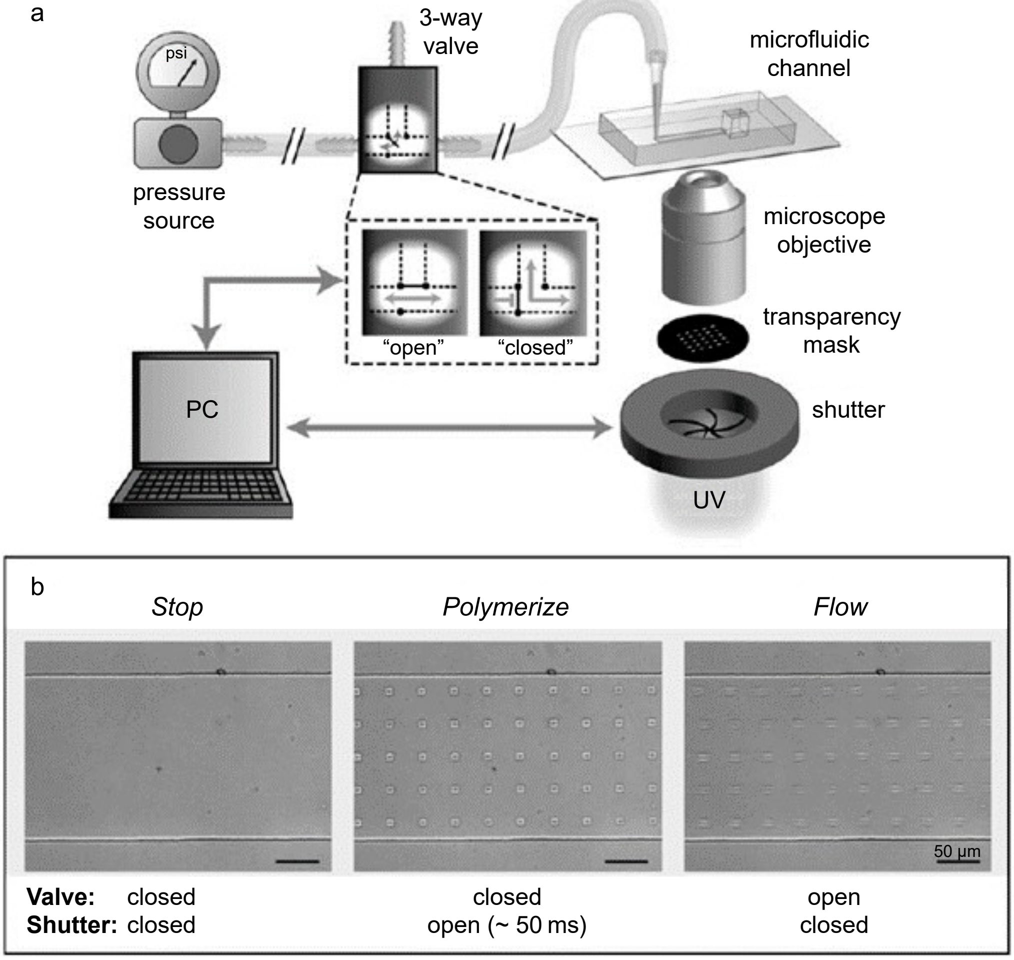

Figure 1.3: Anisometric microgel fabrication via stop-flow lithography (SFL). (a) Schematic setup and (b) micrographs of the three states of the process with scale bars showing 50 µm. [Dend2007b]

To obtain distinctly shaped microgels, the timing within the repetitive cycle must be precisely synchronized. The settling time defines the time between the flush of the previously fabricated microgels and the exposure of the next microgels, equaling the *stop* duration. An accurate settling time ensures a standing fluid during exposure, which is crucial for precise fabrication with detailed shapes. If the settling time is selected too short, the shapes blur. A settling time that is too long reduces the throughput, which applies to all time steps of the fabrication that are selected too long. The exposure time, as the *polymerize* duration, determines the energy input into the system and directly correlates with the characteristics of the microgels. After exposure, minor post-polymerizations occur. Hence, the microgels should rest for a defined buffer time, as the duration between *polymerize* and *flow*, before the flushing-induced force is applied to them. Otherwise, the polymeric microgel structure may be inhomogeneous due to a unilateral alteration resulting from the flush. The flush time describes the duration of the *flow* that needs to be sufficient to remove the microgels from the exposure window and ensure that only uncrosslinked pre-polymer molecules are exposed. A prolonged flush time reduces not only the throughput but also wastes educts. The force induced by the flush and the time it takes to achieve its desired effect can be adjusted by adapting the applied pressure or pressure difference. [Dend2007b]

1.2.4 Oxygen Inhibition

The microgel fabrication via SFL benefits from oxygen inhibition occurring during free-radical photopolymerizations. The oxygen inhibits the polymerization of the microgels since oxygen reacts with radical species and, thus, prevents or terminates the polymerization (compare Section 1.2.2). [Ligo2014] At the channel walls, oxygen permanently enters the solution by diffusion through the surrounding microfluidic chip material poly(dimethylsiloxane) (PDMS), as schematically displayed in Figure 1.4. As a result, microgel formation is inhibited at the channel walls by diffusing oxygen within a so-called oxygen inhibition layer (OIL), preventing the microgels from sticking to the channel walls and enabling stop-flow fabrication. [Dend2008] In addition, mass transfer by diffusion and scattering occurs. [Wolf2021]

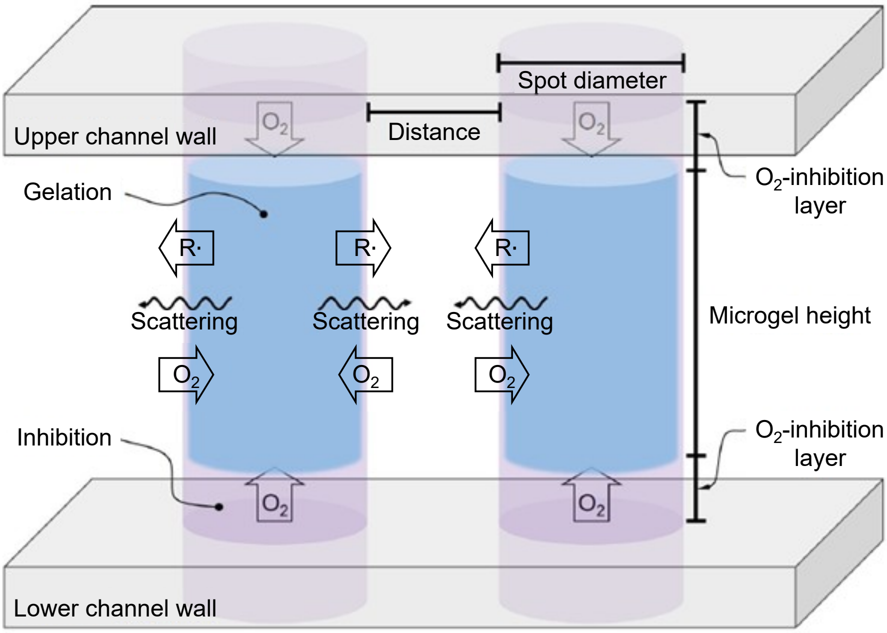

Figure 1.4: Schematically illustrated irradiation of two circle-shaped spots inside a microfluidic PDMS channel, inducing free-radical photopolymerization. [Wolf2021]

The polymerization proceeds from the center of the channel outward. One cause for this is the enhanced oxygen inhibition at the channel walls due to the continuous oxygen diffusion. The other cause is the focus of the light in the channel's center induced by the objective used in the microfluidic approach. However, the elongation of the shaped light is relatively unhindered and consistent through the reaction solution along the channel height. Furthermore, this effect has minor effects for channel heights below 100 µm with appropriate focus depths, assuming almost homogeneous curing of the microgels. [Dend2008; Wolf2021] The works from Dendukuri et al. [Dend2008] and Wolff et al. [Wolf2020; Wolf2021] discussed a variety of parameters that need to be considered for fabricating defined microgels using SFL. Furthermore, the works also demonstrate the advantages of SFL in the facile and continuous fabrication of complex-shaped microgels on the micron scale.

1.2.5 Shape Variance

During SFL, the shape of the microgels is assumed to be a direct elongation of the 2D shape on the transparency mask. However, effects like oxygen inhibition, light focus, mass transport by diffusion, light scattering, and energy distribution significantly influence the 3D shape of the microgels fabricated with projection lithography. [Dend2008; Kim2011; Haki2014; Wolf2021] Two studies [Kim2011; Haki2014] comprehensively investigated the impact of the focus depth and plane position within the microfluidic channel on the 3D shape of the microgels, as shown in Figure 1.5.

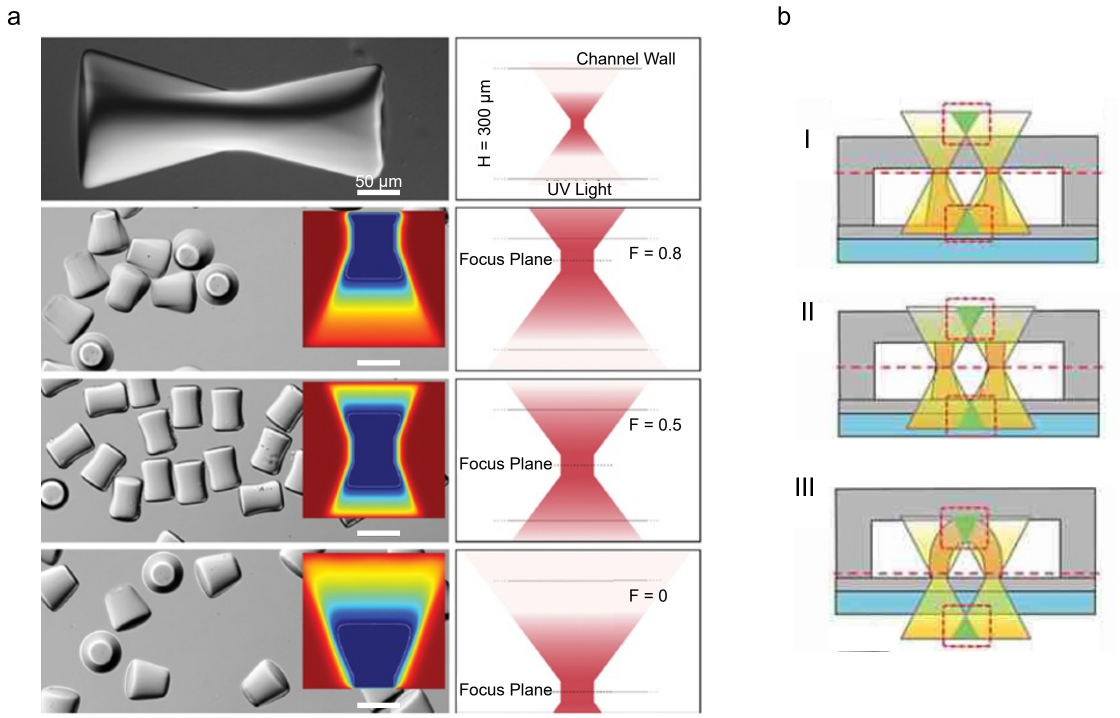

Figure 1.5: Impact of light focusing and focus plane position during projection lithography. Adapted from (a) [Haki2014] and (b) [Kim2011].

In a microfluidic projection setup, the objective lens enables micrometer-sized irradiation but also causes light focusing, resulting in an hourglass-shaped light path instead of being straight (compare Figure 1.5). The numerical aperture determines the focus depth and, thus, the degree of this hourglass shape by controlling the incident light angle. As a result, the light diverges in front of and behind the focus plane, resulting in a decreased radiant power with distance from the focus plane.

A uniform elongation and, thus, no shape variance of the microgels occurs when the focus depth as the narrowed part of the hourglass spans the whole channel height. If the focus depth is smaller than the channel height, the shape of the microgels follows the non-uniform shape of the light within the channel. Figure 1.5a shows an hourglass-shaped microgel resulting from this light focus effect by irradiating a circle-shaped spot. Hence, the third dimension of the microgels can be tuned. When the focus plane is shifted with regard to the channel height, the light path within the channel changes from hourglass to trapezoid. The addition of light-absorptive particles to the reaction solution may further increase this effect of out-of-focus propagation of light. [Haki2014]

Regarding more than an individual irradiation spot, light paths can further overlap as schematically displayed in Figure 1.5b. Thereby, the light intensifies in specific regions when the light paths of separated transparency mask spots interfere in the out-of-focus regions. As a result, 3D-shaped microgels are fabricated (compare Section 1.3.4) by polymerization between irradiation spots. [Kim2011; Haki2014]

A non-uniform light path is one cause for shape variance in the third dimension of projected 2D microgels. Another cause for shape variance is the energy distribution during polymerization. For constant radiant energy, the proportion of exposure time and radiant power significantly influence the elongated shape of the microgels. Figure 1.6 shows three microgels fabricated with the same radiant energy ($\approx 82\,\mathrm{mJ}$, corresponds $21\,\mathrm{mJ\,mm^{-2}}$ radiant exposure) but varying proportions of exposure time and radiant power. The shape of the microgels differs for variant radiant power. [Wolf2021] The higher the proportion of the radiant power, the straighter and the longer the microgels, corresponding to an almost ideal elongation of the mask shape. For low radiant power but long exposure time, the microgels are shorter and have an elliptical shape in the third dimension. [Wolf2021] In total, the same amount of radicals are formed due to constant radiant energy. However, the photolysis rate of the photoinitiator is proportional to the local radiant power, and thus, the radical formation spans over

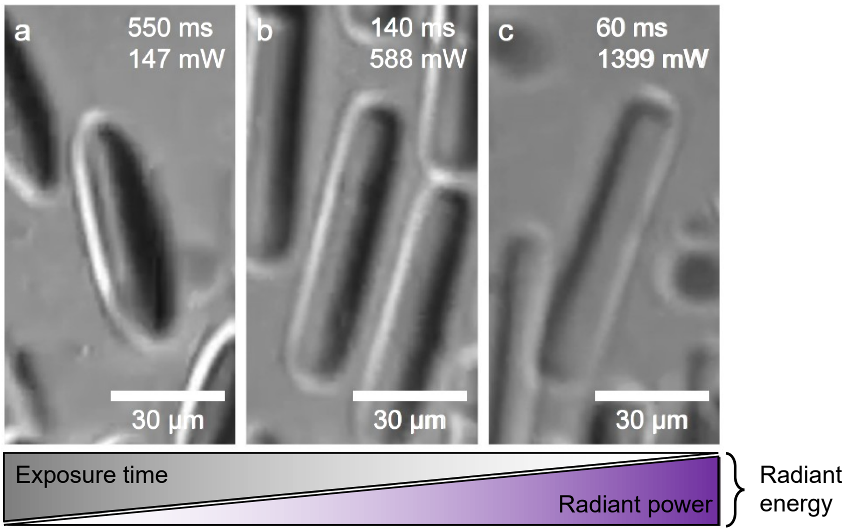

Figure 1.6: Rod-shaped microgels fabricated via SFL and their shape variance as a result of energy distribution settings, varying the exposure time and radiant power for constant radiant energy input. [Wolf2021]

a longer time for long exposure with low radiant power. [Haki2014] The microgel shape variance most likely results from a longer diffusion time that increases the radical and pre-polymer diffusion and widens the microgel's mid where the oxygen inhibition is low. Simultaneously, the microgel shortens due to increased oxygen inhibition at the channel walls. The lower radiant power causes fewer radials at a time, whereas the OIL most likely maintains its thickness because the longer exposure time enables the oxygen to re-diffuse through the channel walls and compete for radicals. As a result, less polymerization occurs towards the channel walls and the microgel height reduces. [Wolf2021; Dend2008]

Both observations induce contrary shape variances of the microgels. The focus effect results in a narrowed microgel shape in the focus plane at the middle of the channel, whereas the energy distribution effect causes an elliptical shape with a widened mid. As the focus-induced shape variance, the energy distribution-caused shape variance overcomes nearby irradiation gaps. However, the interconnection of polymer networks forming at individual irradiation spots occurs in focus in the middle of the channel instead of in the out-of-focus planes.

1.3 Microgel Characteristics

Materials that change their properties in response to external stimuli, such as certain microgels, are known as smart materials, enabling to change the microgels upon request. The environmental stimuli that can cause a microgel response are diverse and include temperature, pH, light, magnetic field, electricity, and more. [Haq2017; Agra2018] Furthermore, the microgels' porous structure and their shape significantly influence the responsive behavior of the microgels, for example, the velocity or the homogeneity of the responses. [Mou2014; Liu2024]

1.3.1 Porous Structure

The defining property of microgels is the absorption and preservation of high contents of water or other solvents in their swollen state. Therefore, the diffusion of 0.265 nm-sized water molecules into the microgels is essential and needs to be enabled by their porous structure to define them as microgels. However, the definition of porous microgels is not standardized. [Foud2023]

Commonly, the microgels are categorized according to their pore sizes. The IUPAC classification of porous materials defines pore sizes based on the adsorption mechanism via standard Brunauer-Emmett-Teller (BET) experiments (77 K, 1 atm) with nitrogen. According to this classification, micropores below 1.4 nm, mesopores of 3 - 50 nm, and macropores over 50 nm exist. However, for microgels, terms like "dense" or "nanoporous" are used in literature, which are not defined but usually refer to mesh sizes of 1 - 50 nm or below 100 nm, respectively. In addition, pore connectivity is included in some definitions, referring to closed and open pores. Even the definition of an open pore varies. Some define the interconnectivity by physical interconnections in the network, whereas others relate to the capillary action of the pores. [Foud2023] To conclude, the porosity of microgels is not easy to categorize. However, defining the aspects of the porous microgel network ensures comparability.

The pore size is only one parameter to be considered. Another is the classical definition of porosity as the ratio of the void volume fraction to the total volume. Furthermore, the pore size distribution, the pores' interconnectivity, the texture of the polymeric network, the pore arrangement, and the nature of the pores are relevant for comprehensively describing porous microgels. Thereby, the nature of the pores intends aspects like the tortuosity, shape or sphericality, and the directionality of the pores. [Foud2023] All these parameters define the porous structure of microgels.

The porous structure is a core parameter of microgels and is related to other characteristics of microgels, like stiffness, stimuli-responsiveness, or cell interaction. [Janm2020; Kitt2023; Foud2023] The porous structure directly depends on the degree of crosslinking and the mesh size of the microgels which is defined as the distance between crosslink points of a polymer chain segment. This mesh size affects the stiffness and mechanical properties of the microgels. [Kitt2023; Foud2023] The degree of crosslinking also determines the possible maximum swelling of the polymer network within a solvent. [Flor1943]

Furthermore, the porous structure of microgels is directly related to the velocity at which microgels respond to environmental stimuli. A high porosity results in a large surface area which causes a fast response. An exemplary stimulus is the temperature, and thus, the microgels' porosity influences the thermal response of thermoresponsive microgels. [Chu2007; Mou2014; Liu2024]

1.3.2 Thermal Response

Thermo-responsive microgels change their appearance and properties upon change of temperature. [Sier2014] This characteristic originates from the properties of the polymer of which the microgel consists. Thermo-responsive polymers exhibit a phase transition in solution according to their surrounding temperature, reversibly changing between a soluble and an insoluble state. These polymers can be divided into negatively and positively thermo-sensitive. Negatively thermo-sensitive polymers exhibit their insoluble state and contract above their so-called lower critical solution temperature (LCST). In contrast, positively thermo-sensitive polymers contract below a certain temperature, their upper critical solution temperature (UCST). [Haq2017]

PNIPAM is a negatively thermo-sensitive polymer with an LCST of 32 ℃ [Pelt2010; Haq2017; Sier2014], which was first described by Heskins and Guillet in 1968. [Hesk1968] Today, PNIPAM is a well-investigated polymer widely spread and often used for microgel synthesis due to its physiological LCST close to the human body temperature. [Haq2017]

The amphiphilic character of PNIPAM, and the temperature-dependency of hydrogen bonds lead to the phase transition of the polymer around its LCST. The oxygen- and nitrogen-rich domains of PNIPAM, originating from the acrylamide side of the monomer, are hydrophilic, whereas its isopropyl groups and the polymethylene backbones are hydrophobic (compare Figure 1.1). These domains cause either solvent-polymer or polymer-polymer interactions, being responsible for the occurring states of the polymer. For temperatures below the LCST, strong hydrogen bonds occur between the hydrophilic domains of the polymer and the aqueous solution. In this state, the polymer is surrounded by water with low polymer-polymer interactions, which leads to a random-coil structure of the polymer in solution. When the temperature is increased, the hydrogen-water bonds break, and the polymer-polymer interactions of the hydrophobic isopropyl groups become dominant. Hence, water is released, and the insoluble state with its globule form is favored above the LCST. Thus, changes in temperature cause altering solvent-polymer and polymer-polymer interactions due to a shift in hydrophilic and hydrophobic forces, determining the present state of the polymer in solution. [Pich2010; Pelt2010; Haq2017]

Microgels consisting of crosslinked thermo-sensitive polymers equal the polymers' thermo-sensitive properties, and their thermal response follows the same mechanism as the non-crosslinked polymers. However, due to their crosslinking, the microgels cannot dissolve in the solvent but show a collapsed and swollen state instead. The swelling is caused by the diffusion of water molecules into the polymer network, and the transition between these two microgel states is defined by their volume phase transition temperature (VPTT). The VPTT resembles the LCST of the polymer for microgels consisting of one polymer kind. Combining polymers with different LCSTs influences the VPTT of the microgels, enabling a temperature shift to a desired value. When the VPTT of PNIPAM is exceeded, the dissolved microgel expels water and decreases in size, changing from the swollen to the collapsed state, as schematically illustrated in Figure 1.7. [Pich2010; Hert2013; Foud2023]

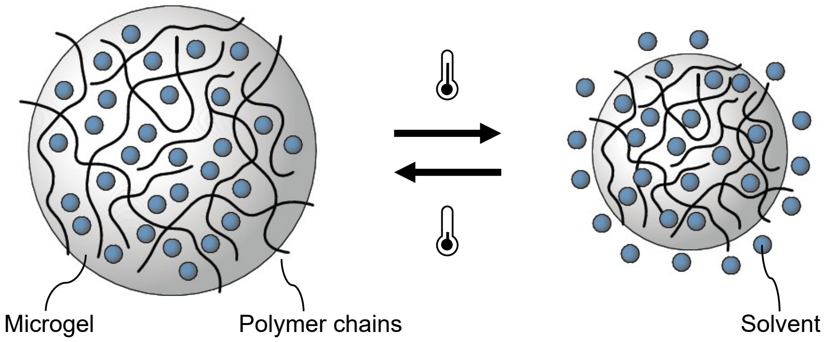

Figure 1.7: Volume phase transition (VPT) schematically demonstrated for a spherical microgel consisting of a polymer with LCST and expelling solvent during collapsing due to a temperature increase. Adapted from [Rodr2017].

In the swollen state, the high solvent content within the polymer network of the microgels results in an equal refractive index of the microgels to the surrounding solvent. In contrast, the refractive index difference is increased for increased temperatures since the gel contains less solvent and is significantly denser in the collapsed state. [Sier2014] The thermo-responsive process of collapsing and swelling of microgels is reversible, undergoing a change in size and sometimes structure that is recovered in the respective states. [Haq2017]

In 1943, Flory and Rehner described the theory of microgel swelling, establishing the well-known Flory-Rehner theory. [Flor1943] The theory provides the basis for understanding the thermal-induced collapsing and swelling process of microgels. However, the Flory-Rehner theory fails to quantitatively describe the thermal microgel response, especially for low crosslinking degrees and low temperatures. [Lope2017] Most of the subsequently published theories describing the thermal response of microgels are based on the Flory-Rehner theory since it shows a good agreement between theory and experiment and is conceptually simple. [Ques2011; Lope2017]

Later, the swelling kinetics of spherical microgels is characterized by their relaxation time, stating that the swelling time is proportional to the square of the microgel's dimension and to its diffusion coefficient. [Tana1979] This relaxation time was extended to describe the swelling kinetics of anisometric microgels. For cylindrical and disc-shaped microgels, the relaxation is longer compared to spherical microgels, showing the impact of the microgel shape on the thermal response. [Li1990]

Some studies [Chen2006; Sun2008; Lu2010; Sier2014] measured the chain interactions and dynamics of thermo-responsive polymers during collapsing and swelling. These investigations help to explain the discontinuous VPT of microgels that differs in collapsing and swelling, resulting in a hysteresis. The hysteresis results from intersegmental hydrogen bond formation of the polymer chains. For the same temperatures, these polymer chain interactions differ in collapsing and swelling, as schematically illustrated in Figure 1.8. In the swollen state, the polymer chains are coiled, and hydrogen bonds almost exclusively occur between the carbonyl groups of PNIPAM and water. During heating, the hydrogen bonds of the polymer chains to water decrease, and an aggregate with a dense core but still a swollen shell forms. This dehydration becomes stronger above the polymer's LCST. Intrachain hydrogen bonds form and result in contraction, followed by interchain associations. As a result, the polymer chains collapse to a uniform aggregate. Subsequent cooling starts the swelling process with uneven swelling of the polymer chains, resulting in a swollen aggre-

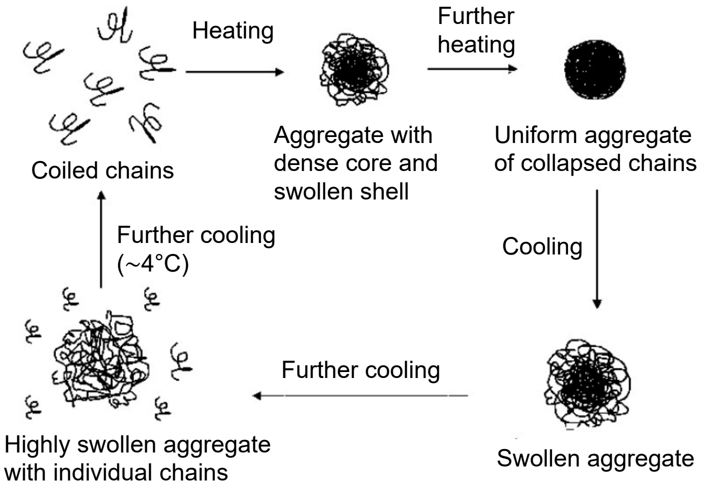

Figure 1.8: Thermal response of PNIPAM in water, displayed as schematic chain association and dissolution. Adapted from [Chen2006].

gate. Thereby, the shell swells more than the core. Some inter- and intrachain hydrogen bonds during swelling remain slightly below the LCST, where these bonds are not present during collapsing. This is stated as the reason for the hysteresis. The polymer chains only dissociate for temperatures significantly lower than the polymer's LCST, reversing the coiled chains. Before, the chain aggregate swells but does not dissociate, causing an intermediate, highly swollen aggregate with individual polymer chains. [Chen2006]

The thermoresponsive polymer PNIPAM not only collapses as a cause of a temperature change but also in a cononsolvent. A cononsolvent is a mixture of two good polymer solvents that become poor solvents when mixed, such as methanol and water for PNIPAM. At a molar fraction of methanol of 0.2, the polymer chains sharply collapse, transitioning from coil to globule state. At 0.4 molar methanol fraction, the chains swell again until full coil recovery at 0.6 methanol. Competing hydrogen bonding of the two solvents in the cononsolvent onto the polymer chain causes this so-called cononsolvency effect. [Tana2008]

1.3.3 Magnetically Induced Motion

Magnetically responsive microgels respond to a magnetic field and align along it, allowing for their precise motion control. To achieve microgels with a magnetic response, additives have to be incorporated into the polymeric network of the microgels since polymers used to fabricate microgels do not have magnetic properties. These additives are magnetic nanoparticles (NPs), typically iron oxides. [Hwan2008; Babu2022]

The incorporation of NPs in the microgels' polymer networks is realized in various ways in the literature. One approach obtains magnetically responsive microgels by entrapping magnetic NPs inside the porous structure of microgels. The preparation process is displayed in Figure 1.9. After fabrication by dispersion polymerization, the microgels were swollen in chloroform to enlarge their pores. The NPs entered into the polymeric microgel network through these pores and were trapped after microgel deswelling. [Yang2010]

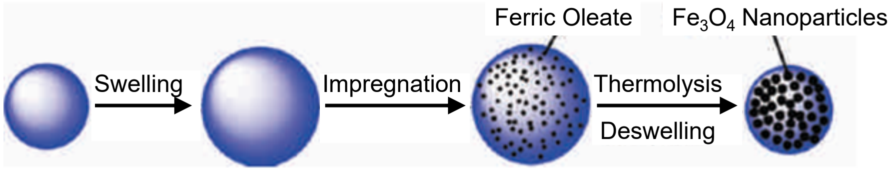

Figure 1.9: Evolution of magnetically responsive microgels by entrapping magnetic NPs in the microgel's polymeric network. Adapted from [Yang2010].

In a different approach, the magnetic NPs grew on carboxyl groups of the microgels' polymer networks. These groups were integrated during microgel fabrication by photo-induced copolymerization, which enabled the capture of ferric and ferrous ions. By subsequent coprecipitation, successive growth of magnetic NPs was achieved, resulting in microgels with high magnetic loading. The synthesis process of the magnetically responsive microgels is schematically shown in Figure 1.10. [Suh2012b] However, both approaches require a multi-step treatment of the microgels after fabrication to achieve their magnetic responsiveness.

A more direct approach with fewer fabrication steps presents the addition

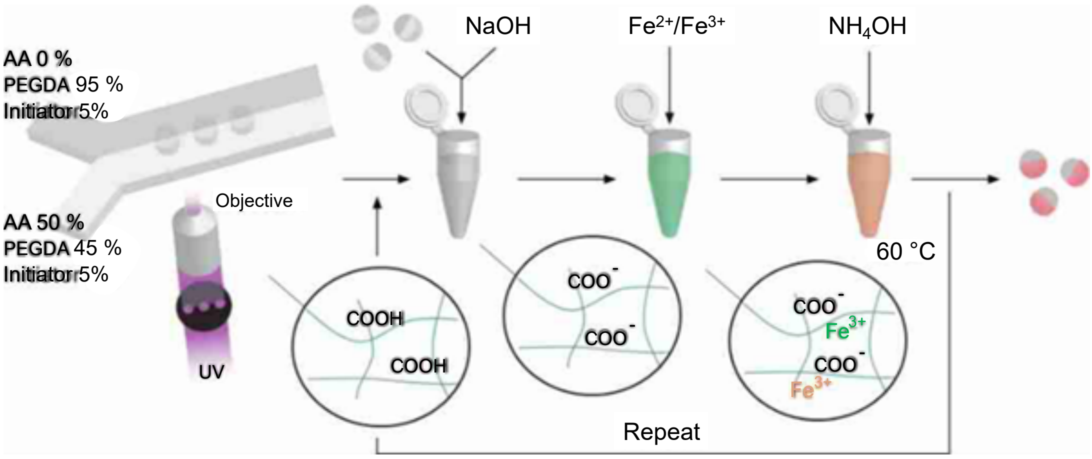

Figure 1.10: Schematic multi-step process to synthesize magnetically responsive microgels. Anisometric and/or Janus microgel fabrication using SFL, introducing carboxyl groups into the polymeric network, which capture ferric and ferrous ions with subsequent growth of magnetic NPs by coprecipitation. [Suh2012b]

of magnetic NPs to the reaction solution with subsequent photopolymerization. This was exemplarly described for fabricating anisometric microgels using particle replication in non-wetting templates (PRINT) [Nune2010] [Brau2022], microfluidics [Hwan2008], or SFL [Haki2014] (compare Figure 1.11). Even though the anisometry and the underlying reaction mechanism of the microgels are consistent for all examples, the methods significantly differ in the setup and the nanoparticles used to achieve the magnetic response of the microgels.

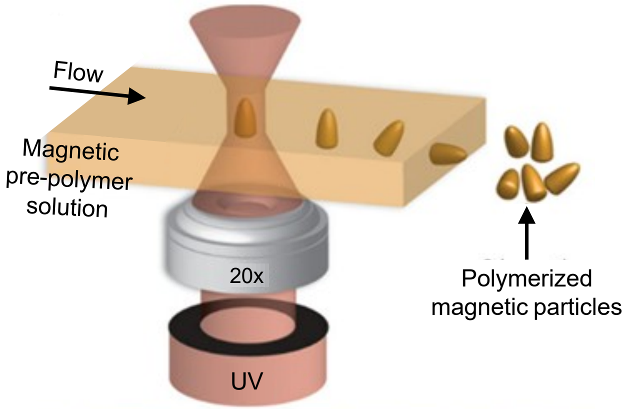

Figure 1.11: Fabrication of anisometric microgels with magnetic responsiveness using a magnetic pre-polymer solution during SFL. Adapted from [Haki2014].

In two of the mentioned approaches [Hwan2008; Haki2014], a commercial ferrofluid was used without applying a magnetic field during fabrication. This results in magnetic microgels, whose magnetic response is directly related to their anisometric shape, aligning along their largest dimension. [Hwan2008; Rose2020b] The reason for this alignment is oppositely positioned magnetic NPs within the anisometric microgels that have opposing forces. Thereby, the magnetic NPs at the microgel edges have a more pronounced effect on the magnetic torque of the microgel than the ones in the center, resulting in an increased magnetic driving force for microgel geometries with a greater aspect ratio. [Rose2020b]

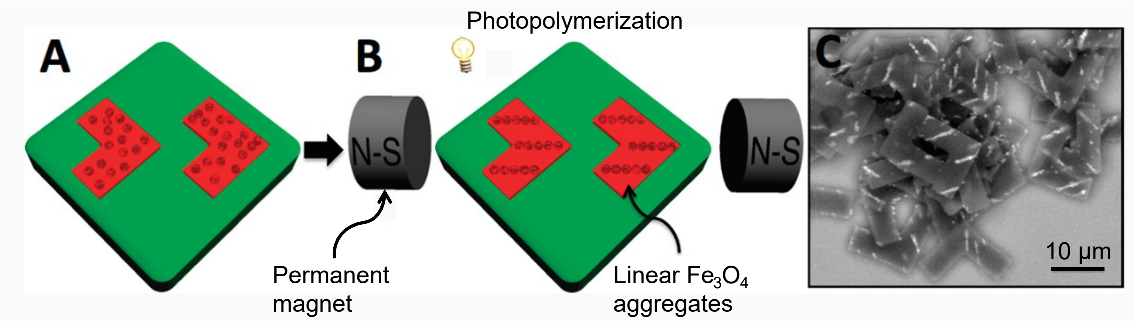

(a) Adapted from [Nune2010].

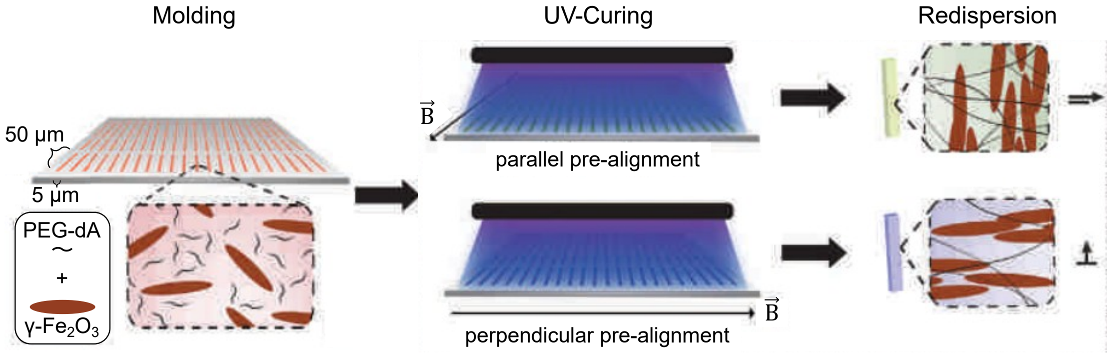

(b) Adapted from [Brau2022].

Figure 1.12: PRINT fabrication processes of anisometric microgels with a pre-programmed magnetic moment. [Nune2010; Brau2022]

Nunes et al. [Nune2010] and Braunmiller et al. [Brau2022] both applied an external magnetic field during fabrication to pre-align the magnetic NPs within the reaction solution prior to photopolymerization. The NPs formed linear aggregates along the magnetic field, which were fixated inside the forming microgels by polymerization. As a result, the aligned magnetic NPs within the anisometric microgels defined the direction of the microgels' magnetic moment independent of the microgel shape, as shown in Figure 1.12. This principle is equal for both works, but different magnetic nanoparticles were used. Nunes et al. [Nune2010] added spherical magnetite (Fe_3O_4) particles to the reaction solution, whereas Braunmiller et al. [Brau2022] applied ellipsoidal maghemite (γ-Fe_2O_3) particles. The chemical composition and shape of the particles differ, resulting in related but slightly different properties of NPs and microgels.

There are different kinds of magnetic NPs that are used to extend the microgels' characteristics and generate magnetically responsive microgels. The iron oxides magnetite (Fe_3O_4) and maghemite (γ-Fe_2O_3) are among the most commonly used. Maghemite is the oxidized form of magnetite. [Mahm2011] Below a material-specific temperature (Curie), these iron oxides are present in a magnetically ordered state and become ferrimagnetic. Ferrimagnetic materials like magnetite and maghemite are strongly attracted by a magnetic field. They have a net magnetic moment resulting from the spins of their unpaired electrons. The spins are aligned antiparallelly and have unequal moments, causing the materials' magnetic moment. [Corn2003] Depending on the size and anisotropy, they can even become superparamagnetic, common for NPs smaller than 10 nm at room temperature. [Corn2003] These particles are called superparamagnetic iron oxide nanoparticles (SPIONs). [Mahm2011]

In addition to the chemical composition, the shape of magnetic NPs influences their magnetic properties. [Itoh2003] Some studies show the synthesis of magnetic iron oxide NPs of non-spherical geometries like cubics or ellipsoids. [Ocañ1999; Itoh2003; Kim2009; Mali2017] In literature, most magnetic NPs integrated into microgels are spherical, commonly spherical SPIONs. These magnetize within a magnetic field and create a local field around themselves without having a predefined dipole moment determined by the NPs' shape. [Rose2020b] In contrast, ellipsoidal magnetic NPs show geometry-related self-assembly within an externally applied magnetic field, as shown in Figure 1.13. [Mali2017] The magnetic ellipsoids exhibit a fixed magnetic moment along their longitudinal axis and align with the magnetic

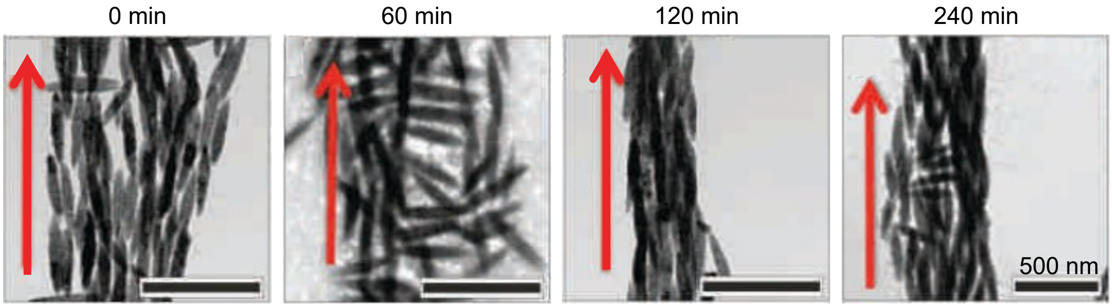

Figure 1.13: Self-assembly of ellipsoidal magnetic NPs (silica-coated hematite α-Fe_2O_3) within a magnetic field (red arrow indicates direction). Transmission electron microscopy (TEM) images after different alignment times (0 - 240 min) with scale bars all showing 500 nm. Adapted from [Mali2017].

field direction by rotation. Depending on time and field strength, multiple ellipsoids form oriented dipolar chains within a magnetic field. [Shin1987; Mali2017]

1.3.4 Shape and Architecture

An anisometric microgel shape provides several advantages over the classical spherical shape. The anisometry allows for targeted shape-related purposes, e.g., as micromachines, building blocks of microelectromechanical systems, encryption units, or biological carriers. Anisometric microgels comprise an increased surface-area-to-volume ratio, which is interesting for applications needing increased attachment areas or improved diffusion efficiency over their surface area. In addition, they show an anisotropic response to external stimuli, expanding the response characteristics for anisometric microgels. [Tian2020; Liu2024] Most of the application advantages reported in the literature contribute to biomedical applications like enhanced cellular interaction, accelerated drug delivery, or improved organ structure mimicking. This application field highly benefits from anisometric microgels, and many positive implications have been reported in the last few years. [Liu2024]

The advantages of anisometric over spherical microgels increased their interest and the associated invention of appropriate fabrication techniques. These methods are mainly based on microfluidic approaches as a result of the desired micrometer-sized resolution. [Liu2024] Plug-flow gelation and jet polymerization involve irradiating a flowing two-phase system within a microfluidic channel. The microgel shape of these two methods is, therefore, limited to spheres, rods, or fibers. [Krüg2019] PRINT enables high flexibility in microgel shapes using a non-wetting mold to form microgels. [Roll2005] However, the fabrication is time-consuming as the fabrication runs in batches and requires multiple fabrication steps, and the molding limits the possible microgel shapes. [Xu2013; Tian2020] Whereas direct laser writing methods provide true 3D shapes with high resolution [Lüke2022], these and related methods are time-consuming and require elaborate equipment. [Kim2011; Haki2014; Tian2020] Projection lithography methods enable the fabrication of microgels with complex shapes by shaping the light source that illuminates the reaction solution and accurately shapes the microgels. [Dend2006; Dend2007b] These methods show high resolution and high throughput with simultaneously low costs. [Tian2020] However, in microfluidic projection lithography, mask-based or maskless, the irradiation shape is elongated along the microfluidic channel height. As a result, the fabricated microgels have elongated 2D shapes but lack a true, defined 3D shape. [Haki2014]

Within the last few years, several methods have evolved to enable the fabrication of 3D shapes via projection lithography by altering the standard microfluidic process. [Tian2020; Liu2024] One possible alteration is applying pressure on the microfluidic reaction channel, thereby adapting its height.

Lock-release lithography utilizes this principle for the fabrication of 3D-shaped microgels, as shown in Figure 1.14a. Channel structures with protrusions towards the channels' insight prevent polymerizations at the protrusion locations during projection lithography. Cylindrical microgels fabricated at the protrusion locations form around them, resulting in cavities at these sides inside the cylinders. To flush the microgels out of the channel and overcome their trapping by the channels' protrusions, the channel is widened by applying pressure inside the channel. [Bong2009] This approach needs custom channel designs dependent on the desired shape and is still limited concerning the shape due to the limited shapes of the channel protrusion after molding.

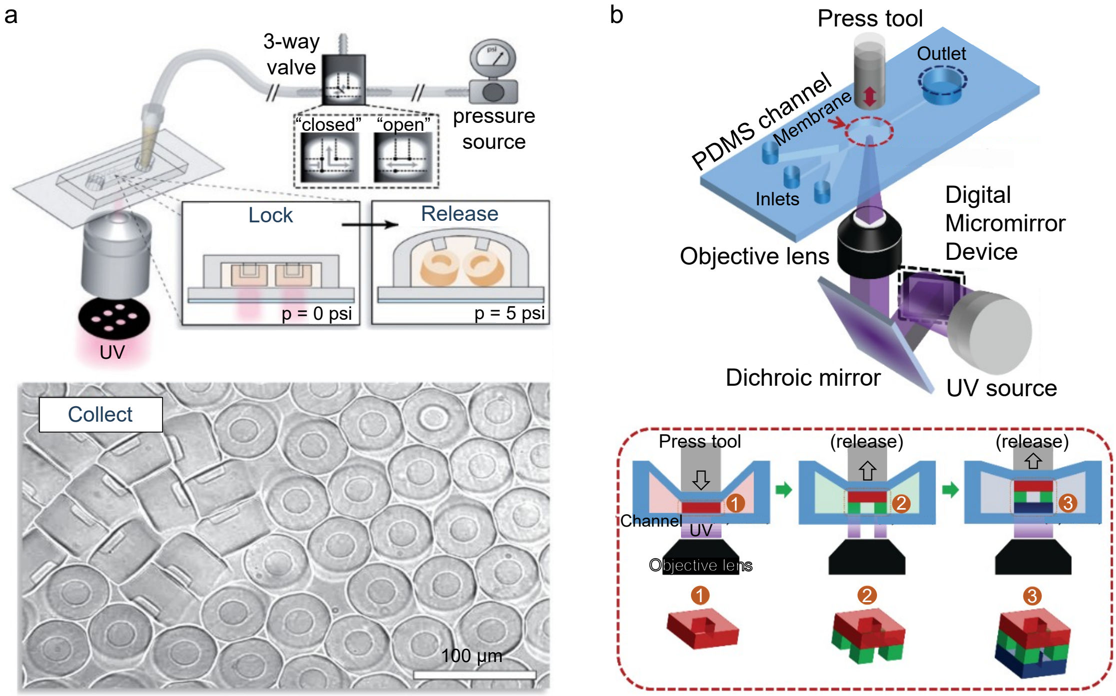

Figure 1.14: Three-dimensional microgels fabricated via pressure approaches changing the channel height during fabrication either (a) to flush trapped microgels out of the channel or (b) to enable multiple projections and thus microgel 3D slices at one position. Adapted from (a) [Bong2009] and (b) [Yoon2020].

A related approach is adapting the whole channel geometry from the common rectangle to, for example, an upside-down T-shape [Chun2008] or a triangle [Zhou2022]. Hence, the microgels' elongation height differs depending on the position within the channel, specifying the third dimension of the microgel shape. By additionally adapting the projection angle to the channel, the same channel geometry can lead to different 3D shapes. [Zhou2022]

Another pressure approach includes external pressure being applied to the channel to compress and precisely narrow its height, as displayed in Figure 1.14b. This is realized in various ways, e.g., by an external press tool [Yoon2020] or by having a two-layered microfluidic channel with a lower channel containing the reaction solution and an overlying pressure channel [Lee2009]. The 3D microgel shapes result from multiple projection steps at the same position but with subsequently released pressure to expand the reaction height between each projection. Each projection represents a slice of the 3D shape, which enables the fabrication of true 3D microgels via projection lithography. [Lee2009; Yoon2020] As a drawback of pressure approaches, the pressure steps increase complexity and are time-consuming, decreasing the microgel throughput.

In projection lithography, tuning the irradiation focus enables the fabrication of three-dimensional microgels. As discussed in Section 1.2.5, the irradiation path is not homogeneous, and this inhomogeneity can be further enhanced by adapting optical features. As a result, microgels with 3D shapes are fabricated in 2D microfluidic channels by polymerization between irradiation spots of the transparency mask pattern. Figure 1.15 displays exemplarily shapes resulting from this technique. The masks are shown in the top right of each microgel shape with the irradiated parts shown in white. The non-irradiated black parts are bridged during polymerization inside the microfluidic channel as a result of light diffraction and overlapping light paths. The height at which the paths overlap is controlled by adapting the focus plane. [Kim2011; Haki2014] As for the pressure approach, the shape configuration of the third dimension is still limited. However, the approach does not require any additional equipment nor reduces the microgel throughput.

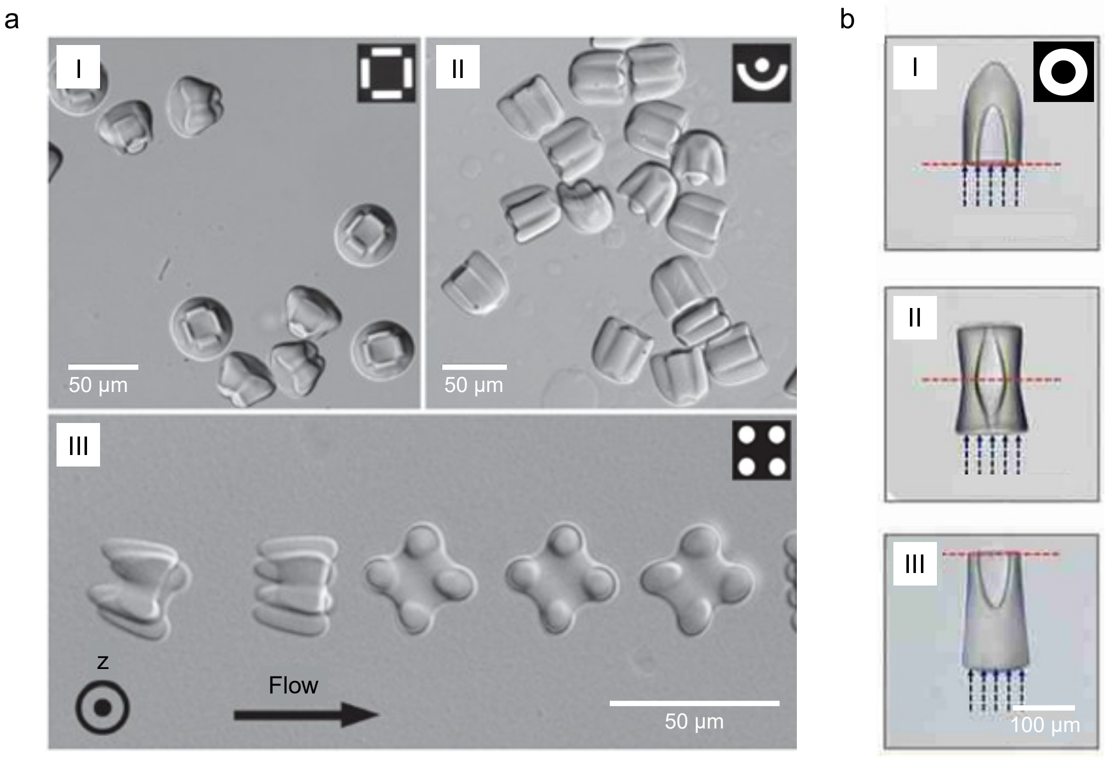

Figure 1.15: Three-dimensional microgels with interconnections between defined irradiation spots (top right) during projection lithography. (b) Scale bar (100 µm) and mask pattern apply to all micrographs. Adapted from (a) [Haki2014] and (b) [Kim2011].

By arranging individual microgels, enlarged complex structures arise even for spherical microgels as building blocks. A common and comprehensively studied approach is a microporous annealed particle (MAP) gel, where injectable microgels are linked, and the void spaces between the microgels function as a second level of porosity (compare Figure 1.16). [Grif2015; Gera2023] The approach was first described by Griffin et al. [Grif2015] for spherical PEG microgels and subsequently evolved toward improved scaffold properties, e.g., by varying the microgel interconnection, size, or shape. [Darl2020; Miks2022; Pfaf2024; Sutu2022]

By using anisometric instead of spherical microgels, the void spaces significantly change. The void geometries become more diverse, and the void interconnectivity is improved for anisometric building blocks. This effect evolves even for comparably simple rod shapes in a random alignment, as shown in Figure 1.17. [Romm2022; Qazi2022]

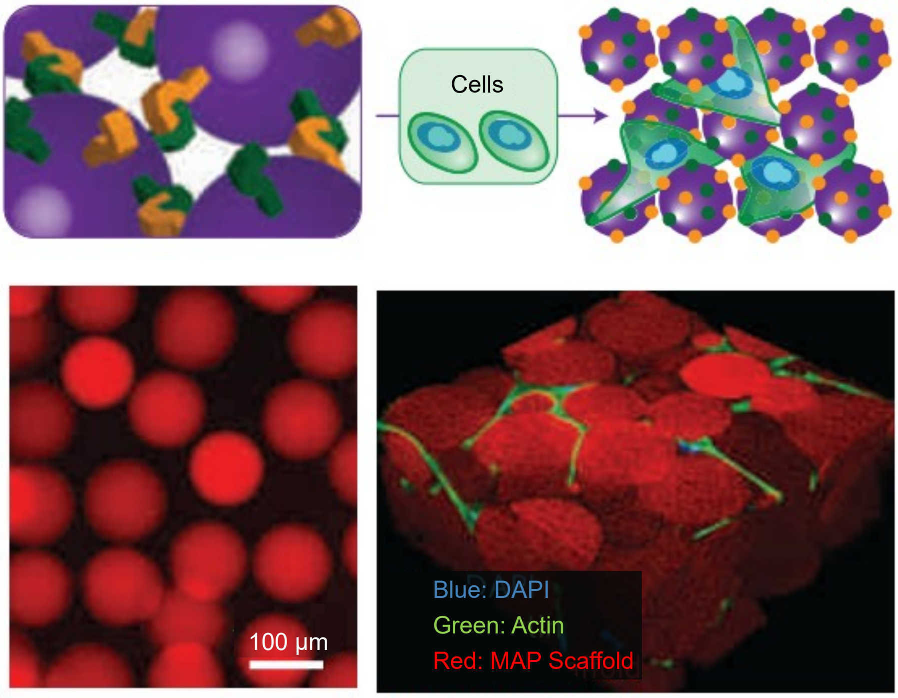

Figure 1.16: Microporous annealed particle (MAP) gel with linked spherical PEG microgels and cell growth in the void spaces. Adapted from [Grif2015].

Figure 1.17: Void visualization of randomly arranged microgel assemblies with varying individual microgel shapes. Scale bar (100 µm) applies to all upper and lower schemes, respectively. Adapted from [Qazi2022].

The mentioned assemblies have a random alignment of the individual microgels, implying limited control of the architecture of these assemblies. Literature reports different approaches and fabrication techniques to order individual microgels and achieve a micrometer-sized architectured 3D design. Microgels can, for example, be aspirated individually onto aspiration holes within a microfluidic channel. The arrangement of the holes determines where the microgels assemble. [Weig2023] Another assemble strategy connects individual microgels based on their shape with male and female anchor structures that interlock when two microgels come into contact. Their contact is guided within a railed microfluidic channel. [Chun2008] However, both approaches rely on modified microfluidic channels that enable the ordered arrangement of the microgels. Furthermore, the approaches only enable 2D assemblies and lack the transfer to self-supporting 3D architectures.

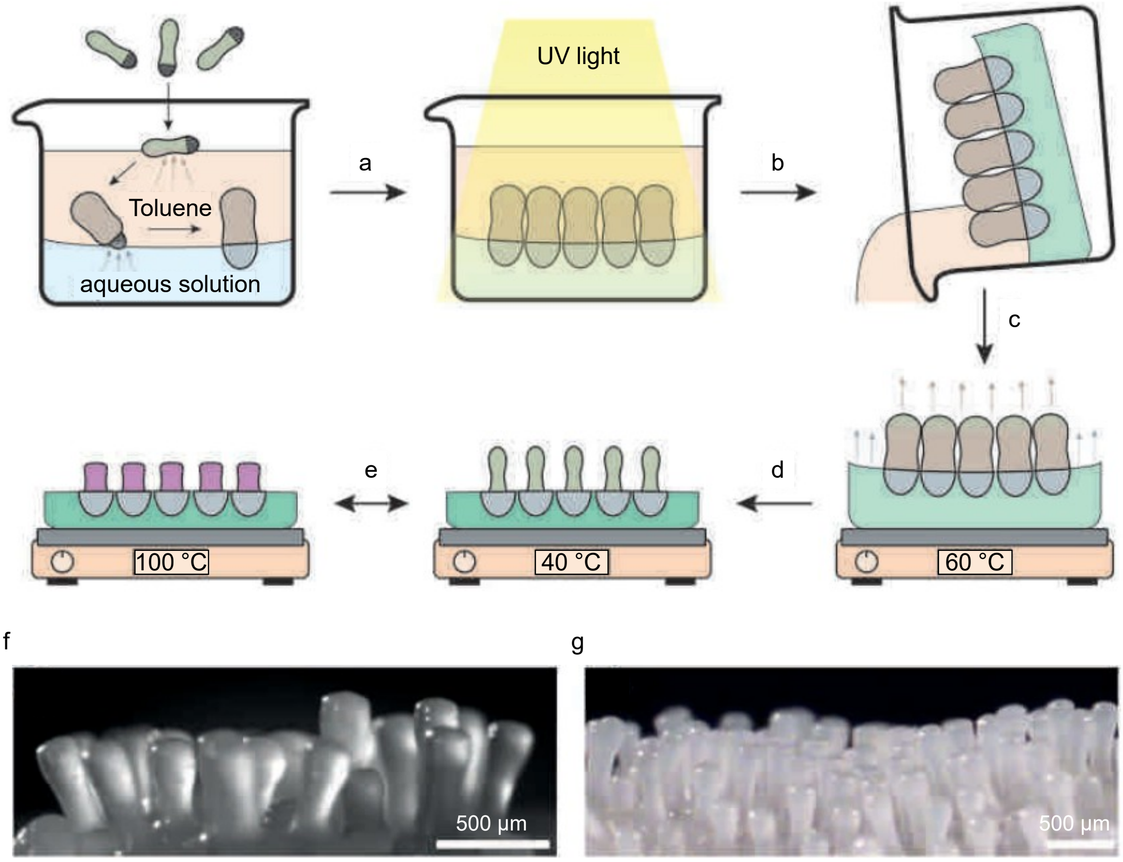

Figure 1.18: Self-assembled and linked Janus microgels. Adapted from [Hess2018].

An approach that arranges anisometric microgels outside of microfluidic channels uses rod-shaped Janus microgels. These provide a hydrophilic and a hydrophobic side, which allows them to be arranged at a phase boundary and subsequently linked. The synthesis process and resulting architecture are shown in Figure 1.18. [Hess2018] This architecture is limited in height but shows a three-dimensional structure. However, the achievement of structures different from the one presented is not straightforward via this method.

When arranging microgels via an induced magnetic response (compare Section 1.3.3), the structured assembly is unlike the other methods presented, not limited to the third dimension. However, this technique only enables the alignment but not the precise arrangement of the microgels to one another. [Rose2017; Babu2022] Furthermore, all approaches in which individual microgels are subsequently arranged in an assembly require multiple synthesis steps and either provide a random assembly, are time-consuming, or depend on a complex setup.

Three-dimensional architectures can also be fabricated directly instead of achieving them by arranging individual microgels. In theory, this saves synthesis steps and allows for a one-step fabrication, where no individual particles have to be fabricated first and subsequently arranged and linked. In practice, directly fabricating 3D microgel architectures is not straightforward under the conditions of a quick and effortless process and a precise and controllable micrometer-sized architecture. Often, molding is used to achieve millimeter-sized architectures with micrometer-sized resolution. [Pape2007; Unad2011; Gjor2022; Call2023] However, the molded geometrical patterns are limited in their 3D shape due to the molding process and lack an extension in the third dimension as well. Voxel-by-voxel and layer-by-layer printing approaches like two-photon-stereolithography or micro-stereolithography provide high resolution and true 3D shapes but are time-consuming and require complex equipment. [Kim2011; Tian2020] Maskless projection using a digital micromirror device enables fast fabrication of a complex-shaped microgel layer with micrometer-sized resolution. Figure 1.19a shows exemplarily millimeter-sized architectures with defined structures. In contrast to the ordered arrangement of individual microgels or molding, these architectures evolve in a fast one-step instead of a time-consuming multiple-step process. [Lu2006; Gauv2012] By micro-

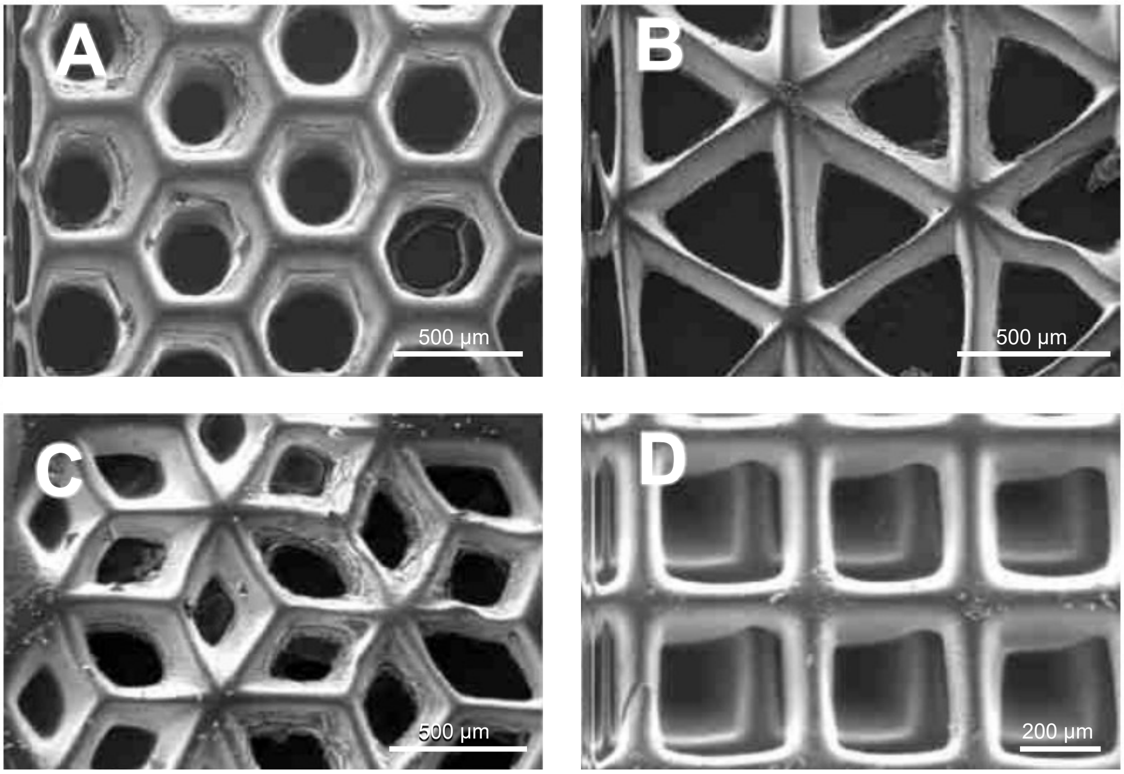

(a) Scanning electron micrographs of geometrically defined microgel (a-c) layers and (d) a two-layered architecture. Adapted from [Lu2006].

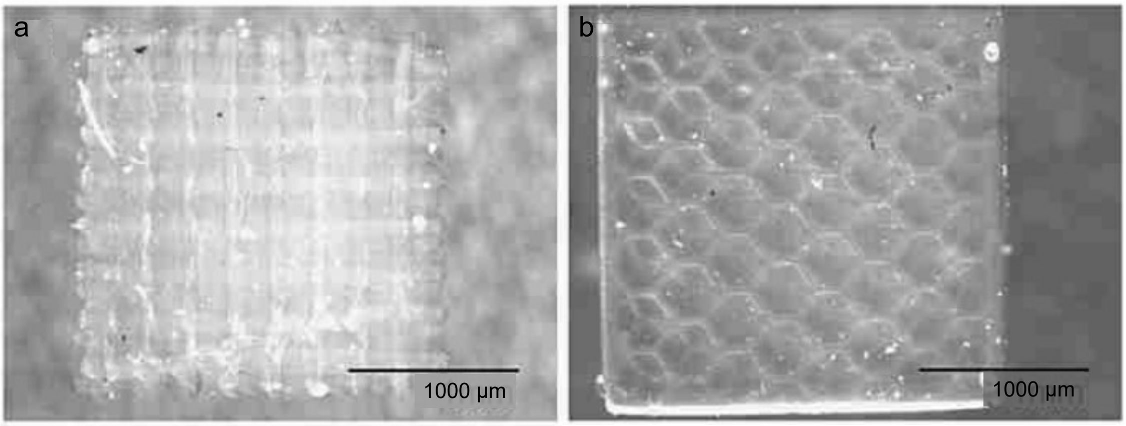

(b) Three dimensional (a) woodpile and (b) hexagonal architectures. Adapted from [Gauv2012].

Figure 1.19: Coherent microgel architectures fabricated using micro-stereolithography.

stereolithography, true 3D architectures with high resolution arise as illustrated in Figure 1.19b. [Gauv2012] However, the extension into 3D architectures requires a layer-by-layer projection, which is time-consuming and renders the setup more complex. [Kim2011; Tian2020]

1.4 Most Relevant Literature

The most relevant literature with regard to the scope of the thesis is listed and briefly summarized below. The publications represent breakthroughs or essential basis with regard to the focused microgel characteristics of this thesis: anisometric shape by fabrication, porous structure, thermal response, magnetic motion, and designed architecture. These characteristics categorize the listed publications, which are ordered chronologically.

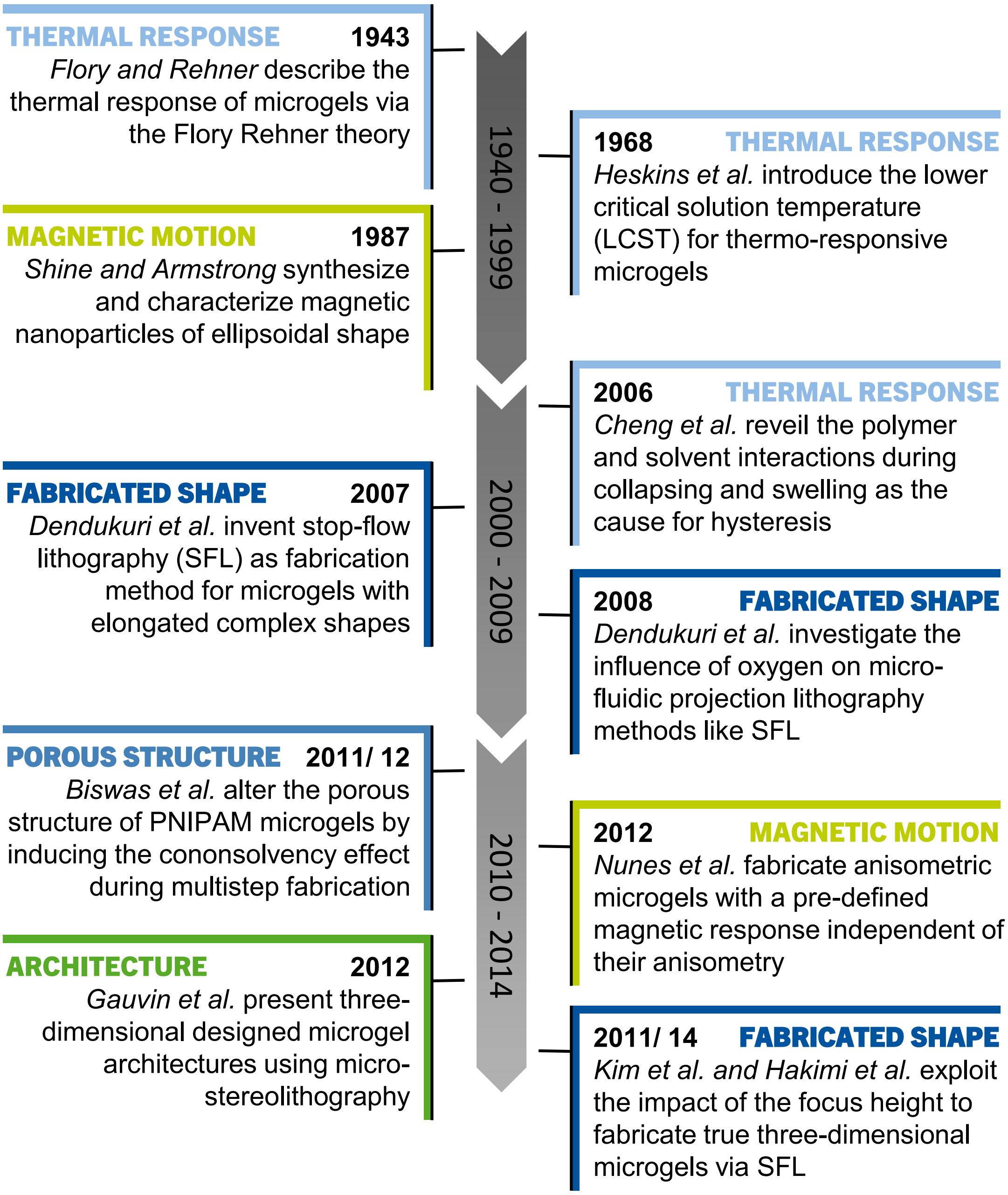

THERMAL RESPONSE **1943**
Flory and Rehner describe the thermal response of microgels via the Flory Rehner theory

1968 **THERMAL RESPONSE**
Heskins et al. introduce the lower critical solution temperature (LCST) for thermo-responsive microgels

MAGNETIC MOTION **1987**
Shine and Armstrong synthesize and characterize magnetic nanoparticles of ellipsoidal shape

2006 **THERMAL RESPONSE**
Cheng et al. reveil the polymer and solvent interactions during collapsing and swelling as the cause for hysteresis

FABRICATED SHAPE **2007**
Dendukuri et al. invent stop-flow lithography (SFL) as fabrication method for microgels with elongated complex shapes

2008 **FABRICATED SHAPE**
Dendukuri et al. investigate the influence of oxygen on microfluidic projection lithography methods like SFL

POROUS STRUCTURE **2011/ 12**
Biswas et al. alter the porous structure of PNIPAM microgels by inducing the cononsolvency effect during multistep fabrication

2012 **MAGNETIC MOTION**
Nunes et al. fabricate anisometric microgels with a pre-defined magnetic response independent of their anisometry

ARCHITECTURE **2012**
Gauvin et al. present three-dimensional designed microgel architectures using micro-stereolithography

2011/ 14 **FABRICATED SHAPE**
Kim et al. and Hakimi et al. exploit the impact of the focus height to fabricate true three-dimensional microgels via SFL

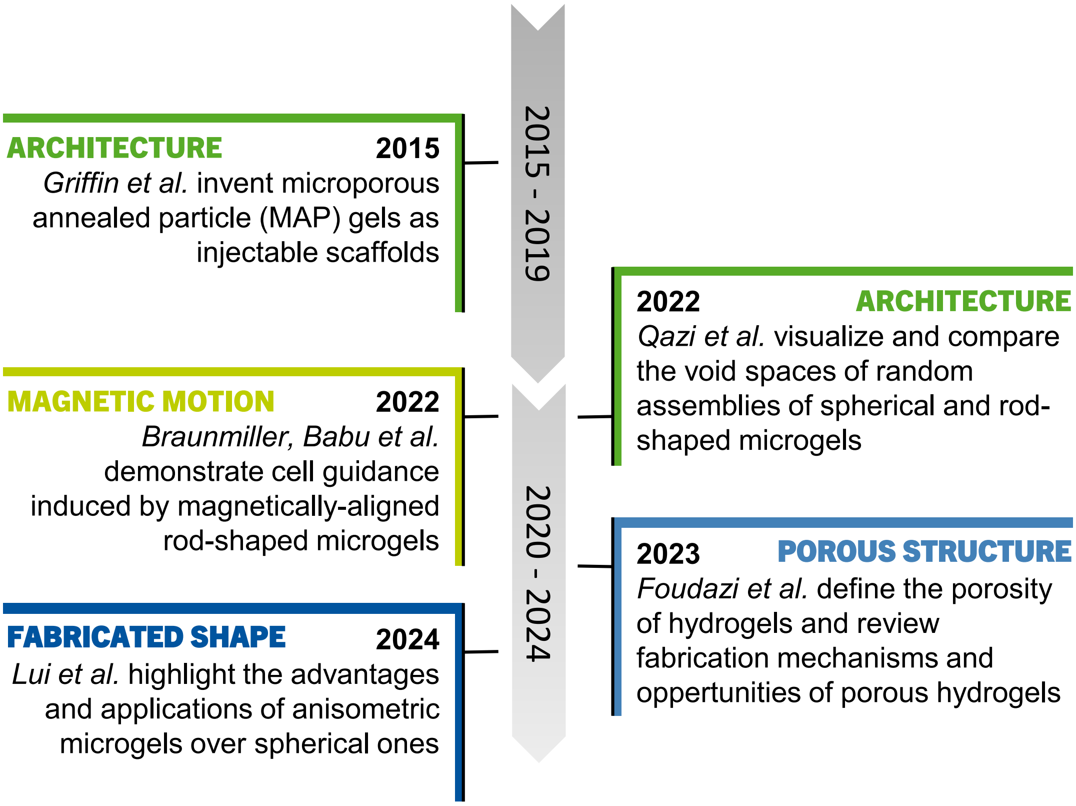

1.5 Scope of the Thesis

The present thesis considers the characteristics of complex-shaped micrometer-sized hydrogels and how to tailor them precisely. In particular, this involves the microgels' porous structure, thermo-responsiveness, magnetic motion, and architecture. An additional focus regarding all customized characteristics is the shape of the microgels. All investigated microgels are anisometric and exhibit complex shapes or even designed architectures. The microgels are fabricated via projection lithography in automated stop-flow mode, presenting a toolbox to design desired microgels with tailored and combinable characteristics. One possible motivation elaborated in the thesis is using these engineered microgels as customizable scaffolds for tissue engineering. Figure 1.20 illustrates the scope of the thesis, highlighting all aspects that are comprehensively addressed.

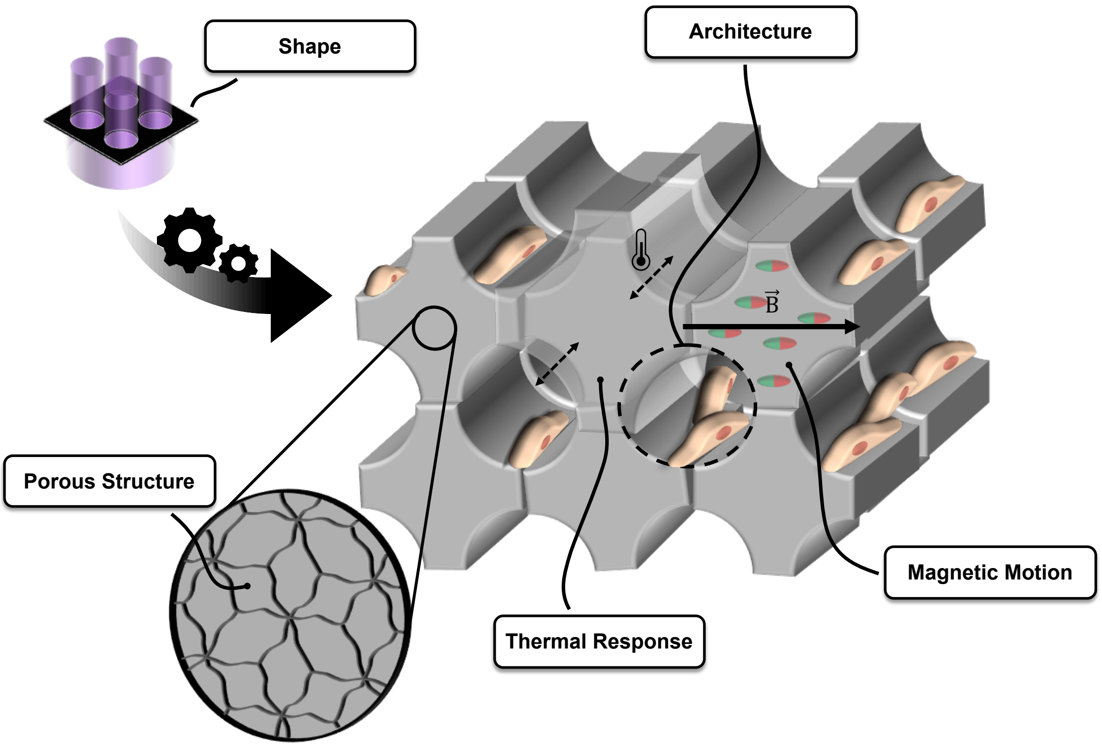

Figure 1.20: Scope of the thesis.

The chapters of this thesis address different research questions related to the focus of the thesis:

- Chapter 2: How can the porous structure and the thermal response of complex-shaped microgels be tailored?
- Chapter 3: Can complex-shaped microgels be precisely aligned or moved?
- Chapter 4: How can functional microgels be arranged in designed architecture?

Chapter 2 addresses the porous structure modification of rod-shaped PNIPAM microgels and the associated changes in their thermal response. The so-called cononsolvency effect during photopolymerization, in which water-methanol mixtures serve as reaction solution solvents, induces these characteristical modifications. This simple fabrication adaption alters the microgels' porous structure, aspect ratio, collapsing degree, collapsing and swelling velocities, and provides internal patterns during swelling.

Chapter 3 focuses on implementing a magnetic response in complex-shaped PEGDA microgels. Pre-aligned maghemite nanospindles during the fabrication step introduce a pre-programmed magnetic moment within the microgels independent of their shape. This feature allows the microgels to be aligned and rotated in an externally applied magnetic field, even incorporating them into microfluidic channels as controllable elements.

Chapter 4 presents hierarchically structured gel networks, so-called patches. The chapter provides a solution for the challenging task of arranging functional microgels in a structured way with at least two levels of porosity. Comprehensive analyses provide the basis for prospective reliable patch fabrication with desired architecture, porosity, mechanical properties, and more. A first cell study showcases the potential of the patches as versatile platform systems with great tunability for diverse applications.

Chapter 5 summarizes the results of this thesis and highlights the benefits of each tunable microgel characteristic. As an exemplarily perspective, the use of the microgels as tissue scaffolds is provided.

This thesis' content and results derive from research conducted under the affiliation and position of the author as a research fellow and PhD candidate at RWTH Aachen University. The position is associated with the Chair of Chemical Process Engineering. This work comprises data based on the following student theses written under the supervision of Lea Steinbeck:

- Maximilian Middeldorf, Bachelor's thesis, 05.2021, *Influence of Methanol on the Porosity and the Thermo-Responsive Behavior of Poly-(N-Isopropyl-Acrylamide) Microgels Fabricated via Stop-Flow Lithography*

- Vincent Hüttche, Bachelor's thesis, 05.2021, *Active Microfluidics with Rotating Microgels*

- Julia Litke, Master's thesis, 06.2023, *Hydrogel Patches as Cell Scaffolds - Synthesis and Characterization*

2 Porous Structure Modification for Tuned Thermal Behavior

Parts of this chapter have been published as:

Lea Steinbeck, Hanna J. M. Wolff, Maximilian Middeldorf, John Linkhorst, Matthias Wessling
Porous Anisometric PNIPAM microgels: Tailored Porous Structure and Thermal Response, Macromolecular Rapid Communications, 2024
DOI: 10.1002/marc.202300680

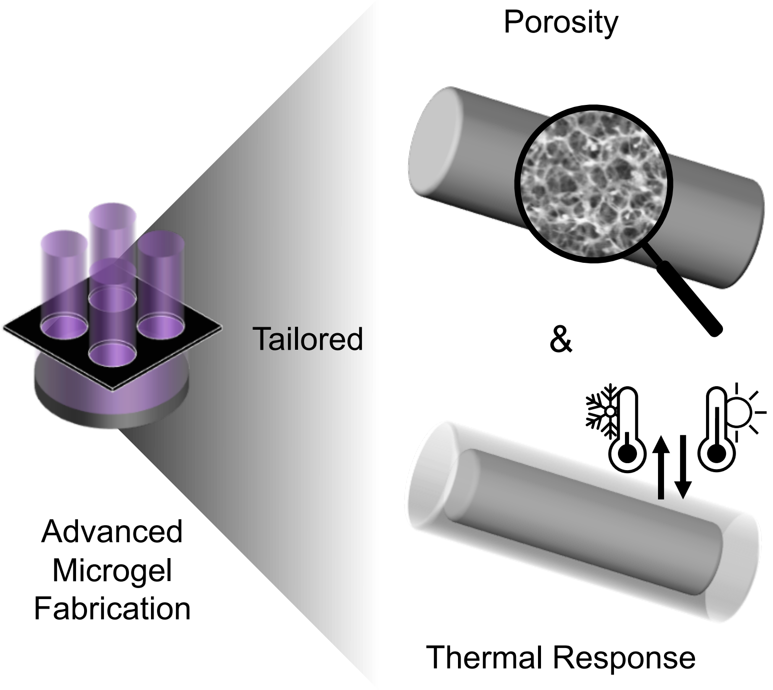

2.1 Introduction

Microgels have developed from model colloids to building blocks for new material systems with various applications. [Karg2019] They are highly swollen polymer networks and have an internal gel-like structure. Microgels provide several beneficial properties, such as being stimuli sensitive to temperature, pH, and ionic strength and even being biocompatible. [Garc2020; Schm2010; Wolf2020] Their softness and interfaces can be engineered [Scot2022] to tailor them, for instance, for cell seeding and cell proliferation. These properties enable the application of microgels as building blocks for minimally invasive scaffolds in tissue engineering. [Feng2016; Grif2015; Liu2017; News2019; Wang2010; Ried2016; Guer2019] Anisometric shapes of the microgels further enhance cell infiltration, migration, and proliferation within these scaffolds. [Babu2021; Grif2006; Hübs2015; Romm2022; Guer2019]

Internal pores in the nanometer scale inside the microgels significantly influence the microgels' functionality and application possibilities. [Mou2014; Bell2020; Wan2008; Dunc2012; Raue2022; Bisw2011; Bisw2012] These internal pores enable nutrient supply [Slau2009] or loading and protective surrounding of drugs. [Wen2019] These effects are not only caused by different ratios of void volume to total volume as per the classical definition of porosity. Besides this, characteristics such as the tortuosity, the sphericality or shape of the pores, the pore size distribution, the texture of the polymeric network, or its directionality must be considered when analyzing the porosity, or more accurately, the porous structure of microgels. [Foud2023]

This porous structure is directly related to the mechanical properties of the microgels as cell support, which has been investigated as one major influencing parameter on cell behavior, especially concerning growth, adhesion, and differentiation. [Janm2020; Raue2022; Pasz2005; Saxe2014] Hence, internal pores play a major role in the success of microgels as biomedical scaffolds.

In addition to the importance for cell cultivation, a high porosity results in a high surface area and, thus, a faster response to external stimuli. [Mou2014; Chu2007] Microgels respond to various stimuli such as pH, ionic strength, or in the case of poly(*N*-isopropyl acrylamide) (PNIPAM) temperature, changing their volume and shape and, in turn, their mechanical properties. [Plam2017; Wolf2020; Schm2010; Sui2011] These temperature-dependent changes of microgels enable further advantages such as controlled drug release [Garc2020; Wen2019], enhanced imitation of the active and dynamic cell environment [Hump2014], regulated cell training, or cell harvesting [Schm2010]. Besides biomedical science applications, hydrogels' porosity is important for various other applications and is of interest in many topics like agriculture, membrane separation processes, or catalysts. [Foud2023]

The thermal response of the microgels is reversible, but collapsing and swelling differ in the case of PNIPAM and related polymers, revealing a hysteresis. The individual polymer chain interactions are temperature-dependent and behave differently for the same temperature values during collapsing, in contrast to swelling. Slightly below the lower critical solution temperature (LCST), some inter- and intrachain hydrogen bonds remain during the swelling process which are not present during the collapsing at the same temperatures. Furthermore, the microgels' shells swell more than their cores during swelling. The resulting inhomogeneous swelling of microgels allows to further achieve areas of varying density and aggregation within one microgel during the microgel's thermal response. [Chen2006; Lu2010; Sun2008; Sier2014] Thus, pores within microgels are directly related to the functionality, mechanical properties, biocompatibility, and responsiveness of microgels. This provides a broad field of applications and a desired need to adapt these internal pores. However, a simple and efficient variation of the porosity within microgels remains challenging, especially with respect to anisometric microgels.

The porous structure and softness of microgels are generally adjusted by changing the amount of monomer or crosslinker as essential chemical components in the reaction solution. [Plam2017; Bach2015; Hwan2017; Chet2013] For UV-initiated radical polymerization, the variation of the exposure time and the radiant power is carried out for this purpose. [Krüg2019] However, these options allow limited flexibility only. Hence, methods to selectively introduce pores into microgels, change their pore shapes, or their polymeric structure without changing their chemical composition are of particular interest. [Foud2023]

One simple and often applied method is to use templates for the pores during the synthesis. [Mou2014; Wen2019; Wan2008; Dunc2012; Raue2022; Bell2020] In the case of PNIPAM microgels, oil droplets [Mou2014] and solid particles [Wen2019] are used as templates in the reaction solution for droplet polymerization. Also, gas bubbles [Wan2008] and porogens [Dunc2012; Raue2022; Bulu2023; Gan2023] are applied as templates in porous particle synthesis.

In addition to templates, in microgel synthesis, porosity can also be induced or adapted using the cononsolvency effect for bulk hydrogels [Bisw2011; Bisw2012], hybrid gels [Sulu2017], or microspheres [Bell2020]. The cononsolvency effect appears with PNIPAM polymers when dissolved in mixtures of two distinct good solvents, such as water and methanol. The polymer is swollen in each pure phase, water or alcohol, but collapses in mixtures of both. [Tana2008; Bhar2022; Sui2011; Sche2014] Competitive hydrogen bonding of water and methanol to the polymer chains of PNIPAM results in a conformation change of these chains and thus in the cononsolvency effect. [Tana2008; Dudo2015; Yong2022] The strongest collapse of spherical PNIPAM microgels is described for a methanol mole fraction of about 0.15 - 0.2. During this cononsolvency-induced collapse, methanol enriches inside the PNIPAM gels. [Noth2019; Sche2014; Bisw2012] Instead of only observing the cononsolvency effect on polymers after fabrication, the effect can be used directly during hydrogel synthesis. Thus, PNIPAM microgels with an altered porous structure are formed without the need for the dispersion of templates in the reaction solution or an additional step to dissolve the solid templates from the pores. [Bisw2011; Bisw2012; Sulu2017] This approach is reported for simple-shaped microgels fabricated via precipitation or emulsion polymerization but lacks a transfer to light-induced radical polymerization via projection lithography and anisometric complex-shaped microgels, which are among others favorable for cell culture scaffolds. [Babu2021; Grif2006; Hübs2015; Romm2022; Guer2019]

Using fabrication techniques like projection lithography, any desired elongated 2D shape of microgels is possible. This freedom in microgel shape enables benefits in various applications, like in the field of biomedical science, allowing the generation of injectable scaffolds for cell growth with tailored scaffold properties on various length scales. [Wolf2020; Dend2007a; Bong2014; Bong2009; Paul2015] Furthermore, light-induced polymerization enables a greater ability to tune the microgels due to the flexibility of the fabrication method.

In this work, the effect of methanol on the porous structure and the responsiveness of anisometric PNIPAM microgels is investigated using stop-flow lithography (SFL) as a fabrication technique. Specifically, rod-shaped microgels are investigated. However, the presented procedure can be used to fabricate any desired microgel shape in future works, revealing the possibility of variation of the fabricated microgels and their wide range of applications. The water content in the reaction solution for PNIPAM microgels is partly replaced with methanol to tailor the porous structure by controlling the cononsolvency effect. Microgels are fabricated with varying amounts of methanol between 0 and 50 wt%, and the respective fabrication parameters applied are investigated. The porosity and polymeric structure of the microgels are qualitatively and quantitatively determined by high-resolution electron microscopy with a subsequent software-based evaluation and by comparing the velocity of the thermal responsiveness of the microgels. Moreover, the outer appearance, the collapsed and swollen states, and the overall thermal behavior of the microgels are observed by light microscopy, allowing further analysis of swelling patterns as a function of the methanol content.

2.2 Experimentals

Reaction Solution Preparation Each reaction solution contained the monomer *N*-isopropyl acrylamide (NIPAM) (98 %, Acros Organics, recrystallized in hexane (99 %, VWR)), the crosslinker *N*, *N*'-methylene bisacrylamide (BIS) (99 %, Sigma-Aldrich), the initiator lithium phenyl-2,4,6-trimethyl-benzoyl phosphinate (LAP) ($\geq$ 95 %, Sigma-Aldrich), and a solvent solution. The solvent solutions contained the surfactant sodium dodecyl sulfate (SDS) (99 %, AppliChem), water (HiPerSolv CHROMANORM, VWR), and methanol ($\geq$ 99.5 %, Carl Roth).

For the preparation of the standard reaction solution without methanol, SDS (40 mmol L^{-1}) is dissolved in water as the solvent solution. The monomer (20 wt%), the crosslinker (2 wt%), and the initiator (1 wt%) were weight out into separate vials each. Afterward, the solvent solution (77 wt%) was added to the crosslinker and mixed thoroughly before being transferred to the vial with the monomer. After all components dissolved, this mixture was added to the initiator as the last component, mixed, and centrifuged to remove any air bubbles that appeared during solution preparation. For samples with methanol, the solvent solution was adapted but its volume was maintained to keep the ratio of monomer, crosslinker, and initiator in solution constant. Depending on the sample variant, the water content is partly replaced with methanol in the respective amount (0, 10, 20, 30, 40, or 50 wt% of the solvent solution) to induce the cononsolvency effect during microgel fabrication.

Microfluidic Chip Production The masters for microfluidic chips were produced using dip-in laser lithography with a two-photon lithography printer (Photonic Professional (GT) Printer, Nanoscribe GmbH, Eggenstein-Leopoldshafen, Germany). [Löls2018] The subsequent casting of the microfluidic chips from the masters was performed by soft lithography. [Kim2008; Xia1998] Poly(dimethylsiloxane) (PDMS) (Dow Corning, Sylgard 184 plus curing agent, 10:1 (w/w)) was used as chip material, being poured onto the master and cured (60 °C, overnight). After detaching, the cured PDMS form was perforated to achieve tubing holes, washed by sonication in isopropanol (5 min), and dried at atmospheric conditions (overnight). Afterward, the PDMS form was bonded on a PDMS-coated glass slide (VWR, 52 x 76 x 1 mm) by oxygen plasma activation (TePla 100 Plasma System, PVA), resulting in microfluidic channels (15 mm length, 900 µm width, 80 µm height) surrounded by PDMS.

Microgel Fabrication using SFL Stop-flow lithography (SFL) was used to fabricate the microgel variants. The basic principle of SFL is established in previous works [Dend2007b; Dend2008; Wolf2020] and visualized in Figure 2.1, whereas Wolff et al. [Wolf2020] lists the individual components of the self-constructed setup used in this work. A transparency mask with circular patterns (200 µm diameter, 400 µm distance to each other, squared arrangement) was used, leading to microgel rods (37 µm diameter, 80 µm length). To ensure an equivalent comparison between microgel variants with different methanol contents, every parameter influencing the fabrication except for the methanol content was held constant. All microgel variants were fabricated with the same radiant power (193 mW, 365 nm). However, as explained in Section 2.3.1, the 50 wt% methanol sample required a longer exposure time (425 ms) compared to all other samples (325 ms) to

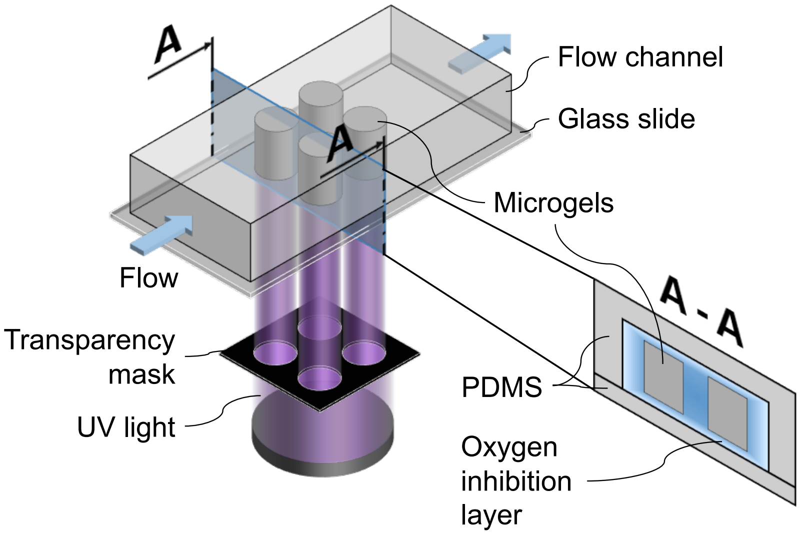

Figure 2.1: Scheme of the stop-flow lithography (SFL) setup to fabricate anisometric microgels.

achieve stable microgels.

All fabricated microgel samples were purified by using dialysis before subsequent investigations. Therefore, the sample was filled in a cellulose dialysis membrane tube (Zellutrans, MWCO: 12—14 kDa, 25 mm flat width, 20 µm wall thickness, Carl Roth GmbH) and inserted in deionized water (10 L, 2x 24 h) to exchange the reaction solution. Until analysis, the purified samples were stored at 4 °C to avoid arising biological impurities.

Temperature-Induced Collapsing and Swelling Experiments The thermal response of the microgels was investigated by heating them (from

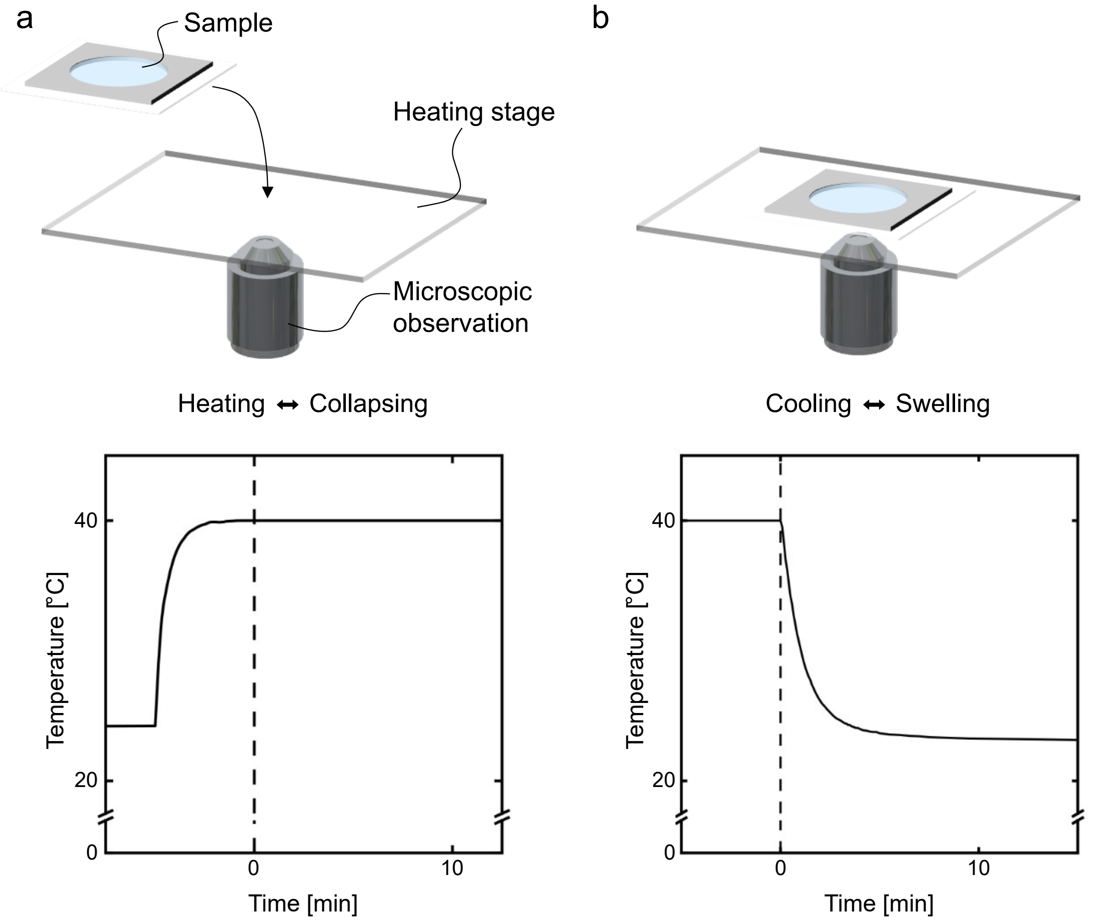

Figure 2.2: Sketch of the investigations of the temperature-induced (a) collapsing and (b) swelling of PNIPAM microgels. The curves show the temperature profile of the heating stage, and the dotted lines at 0 min indicate the time points when (a) the microgel sample is placed on the heating stage for collapsing or (b) the heating of the stage is turned off for swelling as beginnings of the investigations.

22 ℃ to 40 ℃) and then allowing them to cool again (to 22 ℃). During the analysis, the volume phase transition temperature (VPTT) of the PNIPAM microgels of 32 ℃ [Chet2013; Sche2014] was exceeded. Therefore, the microgel sample was warmed up (30 min) to room temperature (22 ℃) prior to the analysis. Afterward, the sample (20 µL) was inserted in a self-constructed PDMS chamber which was subsequently filled up with water (HiPerSolv CHROMANORM, VWR) (40 µL). The filled chamber was covered with a glass slide to prevent the solvent from evaporating. After sedimentation of the microgels (20 min), the sample was placed on a preheated (40 ℃) heating stage (H601-M-frame-glass, Okolab) which was attached to an inverse light microscope (DM IL LED, Leica). Immediately after the sample heating (40 ℃, 20 min), the sample was cooled down (22 ℃, 20 min) by lowering the temperature of the heating stage without active cooling. A sketch of the experimental procedure with schematic temperature profiles of the heating stage is shown in Figure 2.2.

The experiments were repeated for three sub-samples of every microgel variant with varying methanol content during fabrication. From each sub-sample, four randomly selected microgels were evaluated, resulting in a total analyzed amount of twelve microgels per methanol content. Microgel length and width were measured (ImageJ, Verison 1.53a) at defined time points (every 10 s within the first 2.5 min and after 3, 4, 5, 10, and 20 min) from micrographs taken periodically (1 fps) during heating and cooling.

Porous Structure Analysis For the investigation of the porous structure of the microgels, a water drop containing swollen microgels was frozen in liquid ethane (1 min) and stored until imaging in liquid nitrogen (cryo). Using a field emission scanning electron microscope (FESEM) (S4800, Hitachi), the frozen sample drop was cut to visualize the microgels' polymer structure and cross-sections and was sublimated (2x 20 min, -80 ℃) before being imaged (1-3 kV, 1 µA).

In addition to the qualitatively visual observation, the FESEM micrographs were evaluated to quantitatively determine the properties of the porous structure of the microgels. Therefore, a software-based evaluation of the micrographs was used to analyze the porous structures of the microgels as a common procedure for porosity analysis. [Kitt2023; Bisw2012; Patr2022; Sabh2016] The pore sizes, the porosity, and the directionality of representative 0 wt% and 40 wt% microgels were measured based on the microgels' surface structure (compare Figure 2.6 *surface*). The FESEM micrographs of the surface structure are processed according to Figure 2.3, increasing the contrast, blurring the images, binarizing them, and finally visualizing the pores by a sphere fitting algorithm. [Sabh2016] Each image processing step was needed for the accurate determination of the pore diameter distribution. However, the images from the intermediate steps were further used for other analyses. The original images were used for the visualization (compare Figure 2.6). The images with increased contrast were used to determine the directionality of the porous structures via a plugin (directionality analysis v2.3.0, method Fourier components) of the software Fiji (version 2.15.0) as a distribution of ImageJ (version 2). Based on the binarized images, the porosity of the microgels was calculated by counting the pixels representing the pores in relation to the total pixel count. The pore diameter distributions and mean diameters were determined by using a sphere fitting algorithm adopted from Sabharwal et al. [Sabh2016]. This algorithm assumes spherical pores and measures the diameters of

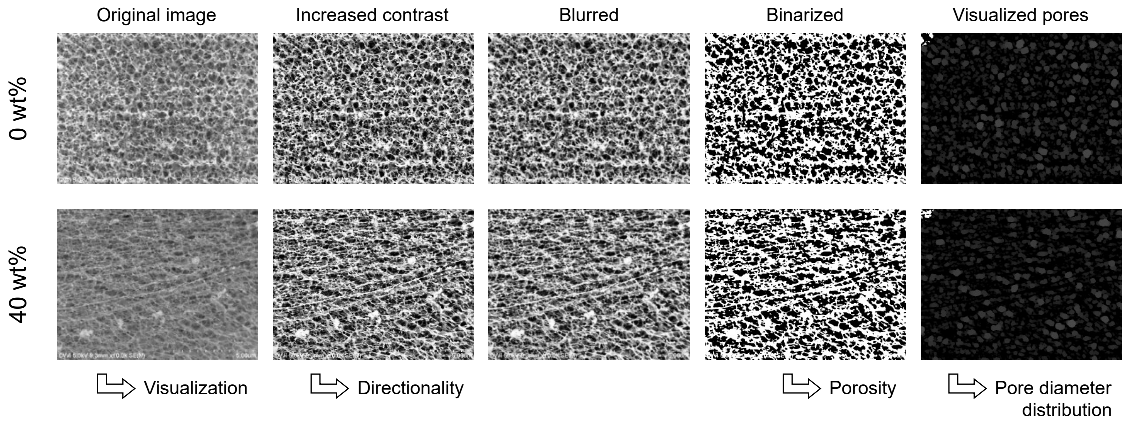

Figure 2.3: Image processing and porous structure analyses - Cryo FESEM micrographs of the surface structure of microgels fabricated with 0 wt% (top row) or 40 wt% (bottom row) methanol during fabrication. Image processing from left to right according to the Python script and indicated purposes of the respective images for the analysis of the porous structure of the microgels.

these pores as well as their relative amount (compare Figure 2.7). Subsequently, the used Python script further enables the visualization of these pores (compare Figure 2.3 right images).

2.3 Results and Discussion

2.3.1 Polymerization of Microgels in a Cononsolvency Environment

To adapt the porous structure and softness of anisometric microgels, the cononsolvency effect is used during microgel synthesis by stop-flow lithography (SFL). More radiant energy is needed in the presence of methanol to form stable microgels. This observation indicates that polymerization proceeds less efficiently in a water-methanol mixture. The polymerization induced in this work is based on two different effects: the light-induced radical polymerization via projection lithography and the polymerization in the presence of a cononsolvent.

Separately, both effects are described in the literature. Dendukuri et al. [Dend2008] model the light-induced free radical polymerization of microgels occurring inside microfluidic devices out of poly(dimethylsiloxane) (PDMS). Here, the four stages of radical polymerization are described, namely photolysis, chain initiation, chain propagation, and chain termination. The fifth possible reaction provides the inhibition of the polymer reaction via oxygen. This reaction mechanism can be directly transferred to the polymer reaction considered in this study.

However, if methanol is added to the reaction solution, the cononsolvency effect influences the polymer formation. This influence so far is only described for spherical microgels during precipitation polymerization. [Sulu2017; Bisw2011; Bisw2012] Here, the observed differences in the microgels are related to the collapse of the PNIPAM chain segments due to their decreased solubility during formation inside the alcohol-water mixture. However, the chemical composition of the microgels is not affected by the cononsolvency effect during fabrication and, thus, remains the same despite the methanol content in the reaction solution. [Bisw2012]

The polymer conversion in this work is determined by both described literature effects, light-induced radical polymerization and cononsolvency-induced phase separation, leading to more radiant energy being needed for microgel formation in a cononsolvent. Whereas the same polymerization conditions could be used for the fabrication of microgels with methanol contents of 0 - 40 wt%, no stable microgels could be fabricated in a reaction solution of 50 wt% methanol with these parameters. Consequently, the exposure time was increased to successfully form microgels in 50 wt% methanol, making them theoretically stiffer than the other microgel variants. On the contrary, the microgels get more deformable with increasing methanol content, as visually observed during the flow period of the SFL process. Furthermore, their post-swelling within the fabrication channel intensifies, exceeding the channel height. Thus, varying methanol contents in the reaction solution affect the properties of gels formed during the SFL process and will be analyzed in detail in the subsections below.

2.3.2 Methanol-Dependent Microgel Dimensions

The optical appearance of the microgels was investigated by brightfield micrographs shown in Figure 2.4a. These micrographs show the optical appearance and contour of the microgels in the swollen and collapsed state, respectively. The more collapsed a microgel is, the better its contours are visible since the refractive index increases. For an increasing methanol content, the microgel length increases in the swollen state and decreases in the collapsed state. Furthermore, especially the 40 wt% and 50 wt% microgels are more elongated than the variants fabricated with less methanol, showing the dependence of the aspect ratio on the methanol content in both states, swollen and collapsed.

To quantify the observed qualitative observation, the microgel lengths and widths were evaluated at low and high temperatures to compare the

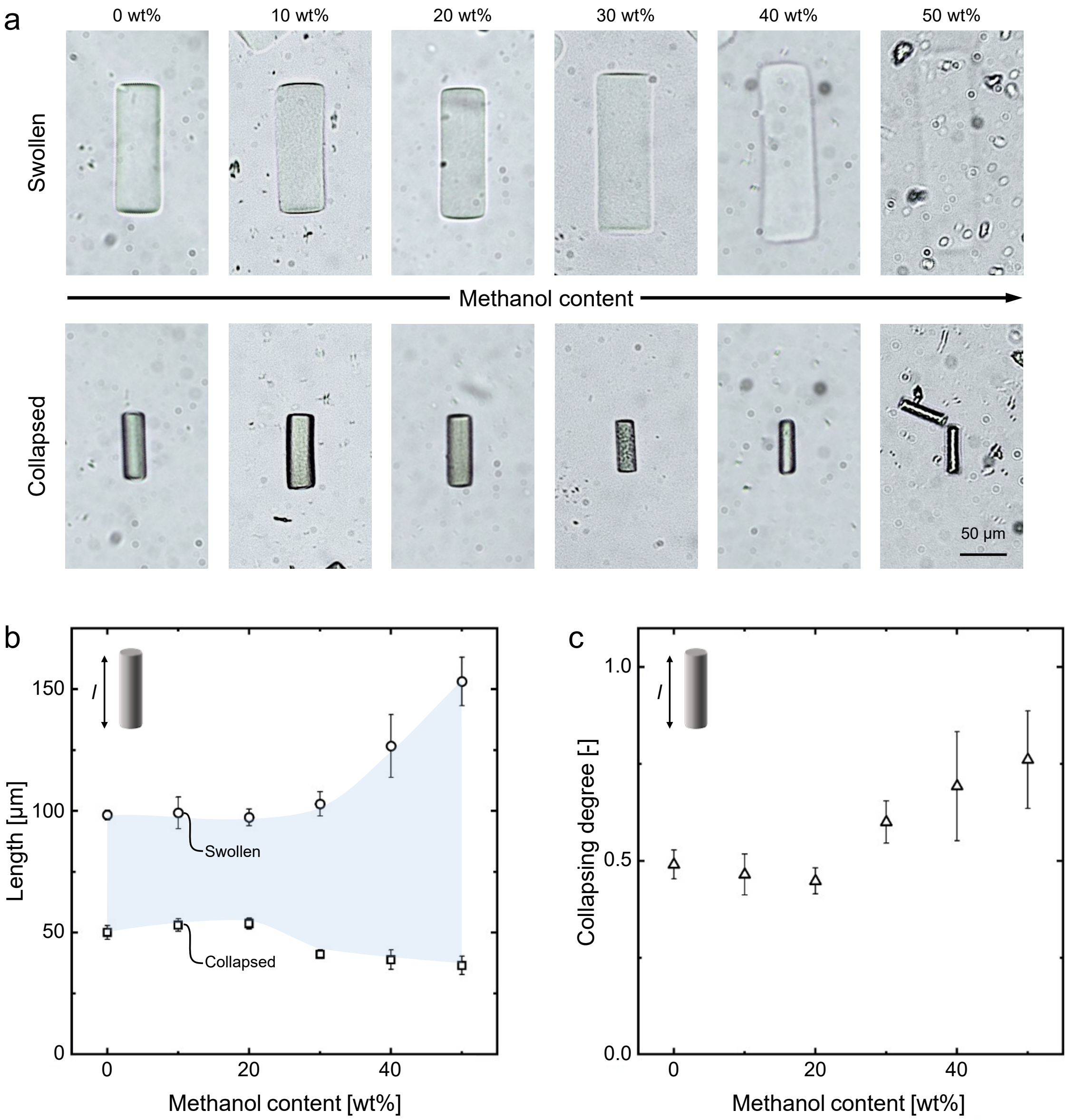

Figure 2.4: Microgel dimensions - (a) Brightfield micrographs of the swollen and collapsed states of exemplary microgels with 0, 10, 20, 30, 40, or 50 wt% methanol. (b-c) Length and collapsing degree comparison of microgels that contained different methanol contents in their reaction solutions during microgel fabrication using SFL. Plotted over the methanol content for samples with 0 to 50 wt% methanol in 10 wt% increments. (b) Microgel length *l* of the swollen (○) and collapsed (□) state each. The blue shaded area indicates the collapsing degree of the different microgel samples. (c) Collapsing degree - Length difference between the states (swollen length - collapsed length) divided by the length in the swollen state.

microgels in the swollen (22 °C) and collapsed (40 °C) state depending on their methanol content. Figure 2.4b shows the microgel length in the swollen respectively collapsed state as a function of the methanol content during fabrication. Both curves, swollen and collapsed, show a distinct trend with increasing methanol content. The curves start to significantly diverge at 20 wt% methanol. Above this methanol content, the size of the swollen microgels increases, whereas that of the collapsed microgels decreases. The swollen microgels fabricated in the presence of 50 wt% methanol are 56 ± 5% larger than microgels fabricated without methanol, whereas the same 50 wt% sample is 27 ± 4% smaller in the collapsed state.

The blue shaded area in Figure 2.4b demonstrates the increase in the length difference of both states for higher methanol content. Due to 50 wt% methanol, the collapsing degree increases to 76 ± 13% in comparison to 49 ± 4% for the methanol-free sample, as displayed in Figure 2.4c (compare Table 1 in the Appendix for all length and collapsing degree values). Thus, methanol has a significant influence on the collapsing degree of the thermo-responsive microgels.

Independent of the methanol content, all microgels in their swollen state exceed the channel height of 80 µm. Hence, the microgels swell after the SFL fabrication, resulting from the exchange of the reaction solution against water after fabrication. These microgel solvents differ in their osmotic contributions, causing a subsequent swelling of the microgels in water with a greater length of the microgels than the channel height during fabrication. With higher methanol contents, this difference between the osmotic conditions of the reaction solution composition and the experimental swelling/-collapse solution even increases. Thus, the post-swelling intensifies with an increase in the methanol content for two reasons: (a) the difference in the solutions and (b) the microgel properties themselves.

In addition to the lengths of the microgels, their widths during collapsing and swelling were investigated, displayed in Figure 2.5a. Dividing the length by the width of the microgel yields the aspect ratio, which illustrates the shape-related collapsing and swelling. Figure 2.5b shows the aspect ratio of the swollen and collapsed states as a function of the methanol content in the reaction solution during fabrication (compare Table 2 in the Appendix for all width and aspect ratio values).

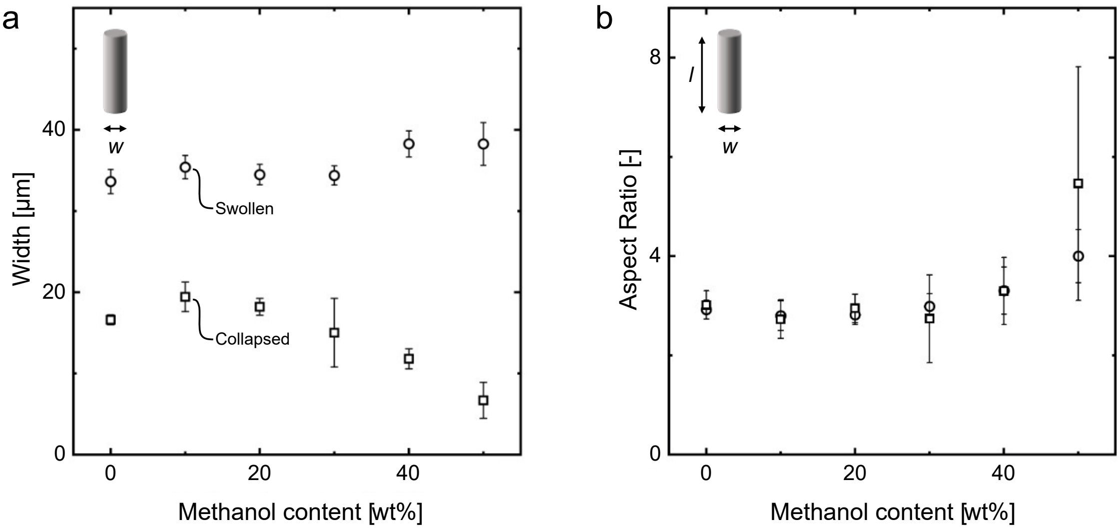

Figure 2.5: Microgel width and aspect ratio plotted over the methanol content for samples with 0 to 50 wt% methanol in 10 wt% increments, showing the swollen (○) and collapsed (□) state each. (a) Microgel width *w*. (b) Aspect ratio - Length *l* divided by width *w* of the respective microgels.

The aspect ratio of the rod-shaped microgels depends on the methanol content in both the swollen and the collapsed states. Up to 30 wt% methanol, the aspect ratios of all samples remain constant at 3. Subsequently, with increasing methanol content to 40 and 50 wt% methanol, the aspect ratio significantly increases, resulting in the lengths of the microgels being up to six times their widths. Thus, microgels are thinner and more elongated if a higher methanol content is present during fabrication. The aspect ratios are consistent between the swollen and the collapsed state of each microgel sample, except for the sample with 50 wt% methanol. However, this sample has comparatively large errors, with the difference between the swollen and collapsed state being within the error range.

The observed increased degree of collapsing with a higher methanol content enables a broadened collapsing window in the microgels' response to external stimuli. For future applications, this extended response may proof beneficial to provide a stimulus in cellular environments or through higher drug loading.

2.3.3 Visual Analysis of the Porous Structure

Microgel samples were sublimated (cryo) to remove solvent from the swollen microgel and to image the remaining polymer features using field emission scanning electron microscopy (FESEM). The micrographs in Figure 2.6 provide an indication of their porous structure. The 0 and 40 wt% variants are compared here, as they possess the most significant difference while being fabricated with the same polymerization parameters.

The first noticeable difference between the micrographs is their polymeric network. This difference applies to the longitudinal surface (compare Figure 2.6 *surface*) as well as the transversal cross-section (compare Figure 2.6 *cross-section* zoom-ins) of the microgels. For 40 wt%, this network is thinner than the one of 0 wt%, showing a distinctly finer structure.

In addition to the overall network, the polymer structure at the surface border of the microgels significantly differs (compare Figure 2.6 *surface border* zoom-ins). The 0 wt% microgels show a distinct and small area of a thinner polymer structure at the surface, whereas the 40 wt% microgels exhibit a noticeably wider area, which is more frayed at the border. This difference in the border of the microgels is further confirmed by the cross-section view of both microgel kinds in Figure 2.6 *cross-section* zoom-outs. Here, a significantly enlightened border surrounds the cutting edge of the cross-sections, indicating the equivalent thinner polymer structure observed in the *surface border* micrographs. This surrounding border is significantly thicker for the 40 wt% microgel compared to the 0 wt% one in the cross-section view, demonstrating another significant difference between the porous structures of microgels fabricated with and without an induced cononsolvency effect during their fabrication.

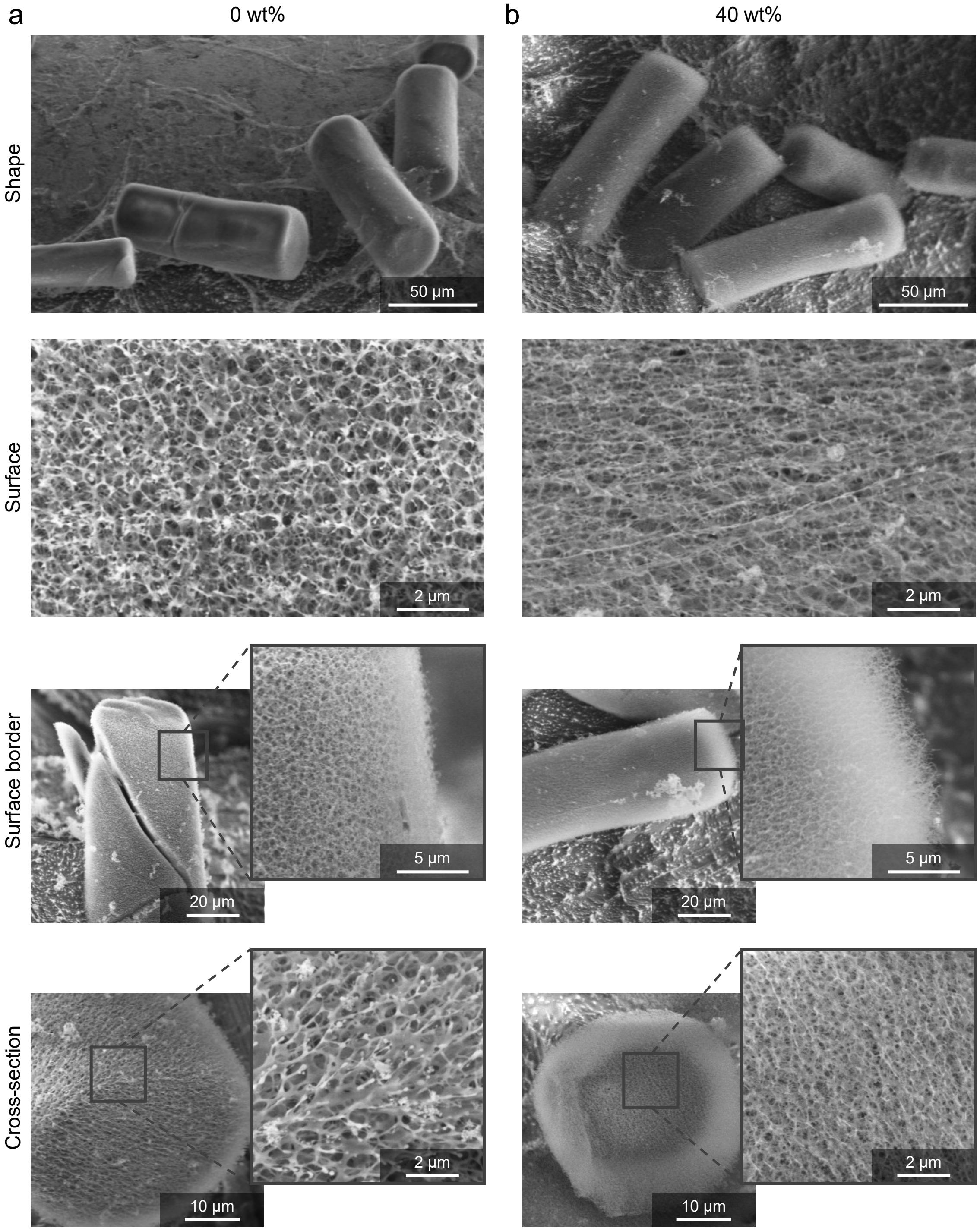

Figure 2.6: Porous structure - CryoFESEM micrographs of microgels in the swollen state fabricated with (a) 0 wt% or (b) 40 wt% methanol in the reaction solution, respectively. Both variants were fabricated with the same conditions despite the methanol content, showing the differences in their porous structure. For both microgel kinds, their shape, surface structure, surface border, and cross-section are depicted.

On the contrary to the observed differences, the porosity and the pore sizes of the bulk of both samples are nearly identical, with a porosity of 48.9 % and an average pore diameter of 214 ± 120 nm for the 0 wt% and 48.3 % and 202 ± 129 nm for the 40 wt% sample. Figure 2.7a shows the pore diameter distributions and the mean diameters of the microgels.

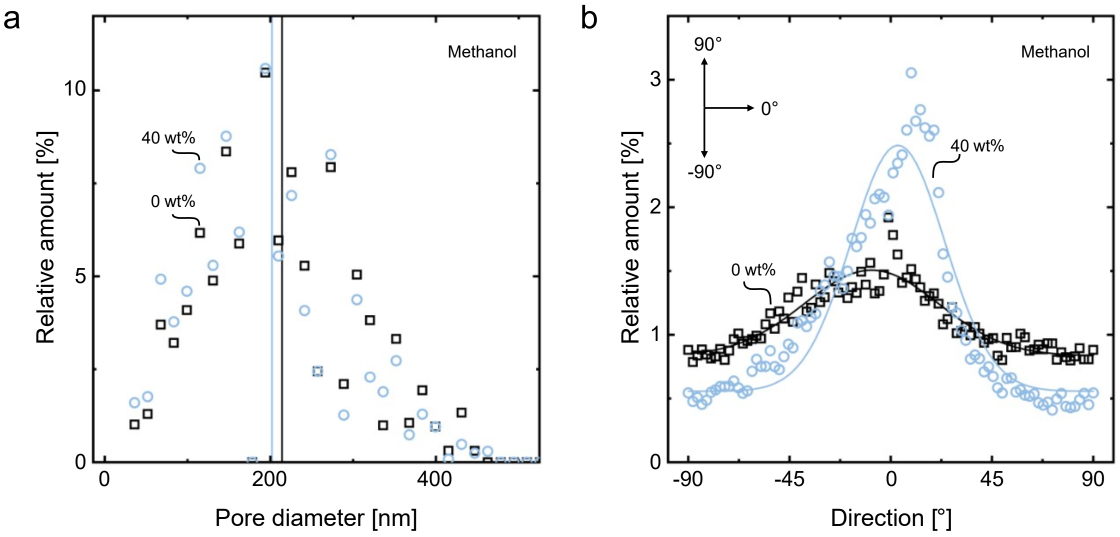

Figure 2.7: Porous structure analysis of microgels fabricated with 0 wt% (□, black) or 40 wt% (○, blue) methanol. (a) Pore diameter distribution with mean pore diameters displayed as vertical lines each. (b) Directionality of the porous structure with respective Gaussian fit.

Even though the pore size distributions are distinctively similar, the pores of the 0 wt% microgels are rounder and more evenly distributed, whereas the 40 wt% pores look elongated and stretched along the microgels' longitudinal axis (compare Figure 2.6 *surface*). Since the sphere fitting algorithm that was used to determine the pore diameters assumes spherical pores, the diameters of elliptical pores are given by their minor elliptical pore diameter. As a result, the major diameters of the elliptical pores, which are mainly present for the 40 wt% sample, are probably actually larger than the diameters of the spherical pores of the 0 wt% sample.

To alternatively measure the pore sizes of the microgels, small-angle X-ray scattering (SAXS) measurements were performed. However, these did not provide meaningful results due to an extremely low signal respectively contrast of the soft microgels, providing a known challenge in SAXS measurements on hydrogels. [Hild2022]

To confirm the presumable pore elongation of the 40 wt% microgels, the directionality of the porous structures of the microgels was measured based on their cryo FESEM micrographs shown in Figure 2.6 *surface*. Figure 2.7b shows the relative amount of structures oriented in a certain direction. The arrows (Figure 2.7b top left) relate the direction degrees of the graph to the directions within the micrographs. The most prominent direction within the porous structure of the 40 wt% sample is around 0 °, indicating an orientation of the porous structure along the longitudinal axis of the microgels. All other directions are significantly less prominent, confirming the elongation of the porous structure of the 40 wt% sample. The 0 wt% sample also shows a slightly increased amount of directed structures at around 0 ° toward the longitudinal microgel axis. However, the according peak in Figure 2.7b is comparably low, resulting in an almost flat curve and, thus, little directionality of the 0 wt% sample.

A possible explanation for these deviating appearances and the detected elongation of the 40 wt% sample is the differing microgel lengths despite the same fabrication conditions. Although both samples' lengths were limited by the 80 µm channel height during fabrication, the 40 wt% microgels are 127 ± 13 µm long compared to 98 ± 2 µm of the 0 wt% microgels. This increased microgel length leads to an increased aspect ratio of the 40 wt% microgels in the swollen state of 3.3 ± 0.5 compared to 2.9 ± 0.2 of the 0 wt% microgels. Consequently, the microgels elongated in varying degrees subsequent to the exposure-induced polymerization, resulting in the respective porous structures.

Since the microgel dimensions and their porous structure depend on the methanol content during fabrication, the presented procedure enables and simplifies the customization of microgel properties to requirements from applications. Therefore, the porous structure of the microgels was tailored without changing the chemical composition of the microgels. Hence, their porosity as the ratio of void volume to total volume remains the same, while their polymeric structure and its directionality and, as a consequence, their thermal response are significantly altered.

2.3.4 Time-Dependent Thermal Behavior

In addition to the final swollen and collapsed states as size limits of the microgels, their actual collapsing and swelling behavior is considered. The collapsing and swelling kinetics serve as indicators for the differences in the porous structures of the microgels. [Mou2014] In Figure 2.8a, the collapsing of these microgels is displayed by the relative microgel length as a function of the experimental time beginning at room temperature and heating up to 40 ℃.

Not only the extent but also the collapsing kinetics depend significantly on the methanol content during fabrication. For 10 wt% methanol, the velocity is the lowest with $0.22 \pm 0.03\,\mu\text{m}\,\text{s}^{-1}$ as maximum collapsing velocity of the sample, while 40 and 50 wt% collapse the fastest with $0.87 \pm 0.22\,\mu\text{m}\,\text{s}^{-1}$ and $0.96 \pm 0.28\,\mu\text{m}\,\text{s}^{-1}$, respectively. 0, 20, and 30 wt% show comparable, medium collapsing velocities of 0.41 to $0.61\,\mu\text{m}\,\text{s}^{-1}$ (compare Table 3 in the Appendix).

The velocities are related to the overall collapsing degree of the microgels. Thus, a stronger collapse is equivalent to faster-collapsing microgels. At first, all samples show similar collapsing kinetics, diverging after about 1 min except for 10 wt%, being directly slower. Within the first 2-3 min, the largest changes occur, performing only minor changes in size after this time period. The end states are reached after approximately 10 min, after which the relative microgel lengths show significant differences for different methanol contents as addressed and shown in the prior Section 2.3.2.

The reference with 0 wt% methanol collapses to 51 ± 4 % of its prior swollen length, whereas 10 and 20 wt% collapse less. This finding agrees with the observations of previous studies [Noth2019; Sche2014] about PNIPAM microgels showing their strongest collapse in a methanol-water mixture after fabrication at the same threshold region of 15-20 mol%, which corresponds to 24-31 wt% methanol in water. Above this methanol threshold, a stronger collapse is observed than that of the reference sample.

For microgels with a higher methanol content of 30 to 50 wt%, a correlation is detected between the amount of methanol in the reaction solution and the subsequent collapsing degree and kinetics of the microgels. The more methanol is present during fabrication, the stronger and faster the respective microgels collapse for a threshold above 20 wt% methanol.

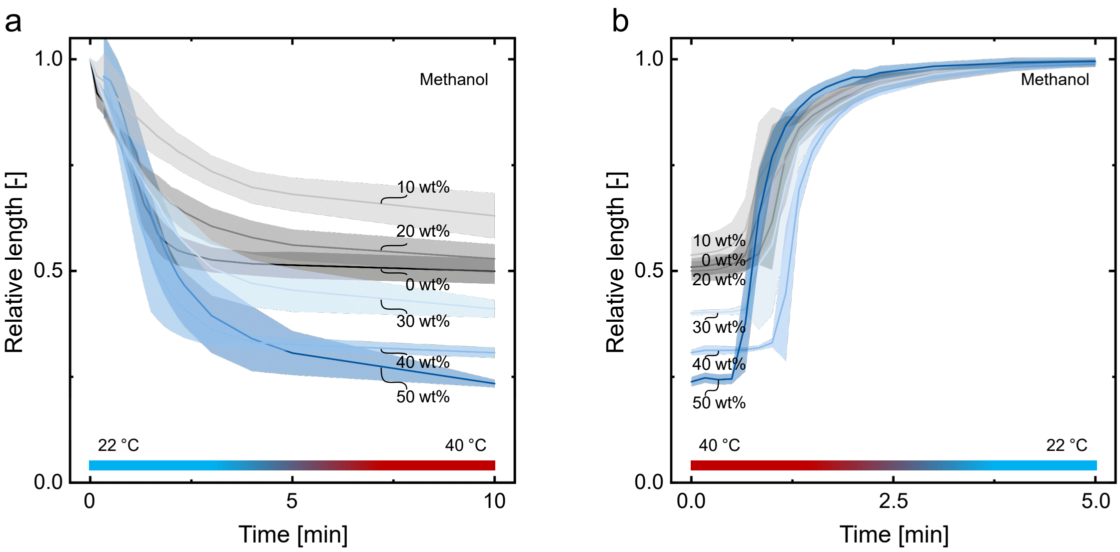

Figure 2.8: Thermal microgel response - (a) Collapsing and (b) swelling curves of rod-shaped PNIPAM microgels over time. Temperature-dependent relative lengths of microgels vary by their methanol content (0–50 wt%) during fabrication. Errors are presented as colored regions around the respective curves.

The swelling behavior of the microgel samples with varying methanol contents during fabrication was investigated by cooling them from 40 °C to 22 °C immediately after collapsing. This swelling is displayed in Figure 2.8b, considering the relative microgel length as a function of time. Since the actual temperature of the sample is unknown with the setup used, the initial points of the curves cannot be directly related to temperature values. Thus, the initial points could be influenced by the experimental procedure rather than being directly dependent on the temperature and should not be directly compared with each other. However, the relative time dependencies and, hence, the curve shapes are comparable.

The shape of all swelling curves is similar, showing an initial resting phase, a rapid swelling phase with comparable swelling velocities, and a constant end phase. Because of the fast swelling kinetics, significant differences in the slope of the swelling curves are difficult to detect. However, the maximum swelling velocities of the samples range from 0.97 ± 0.31 μm s^{-1} for 20 wt% to 3.90 ± 2.10 μm s^{-1} for 50 wt%, as shown in Figure 2.9b. In comparison, the maximum velocities measured during collapsing are significantly lower with 0.22 ± 0.03 μm s^{-1} for 10 wt% to 0.96 ± 0.28 μm s^{-1} for 50 wt%, as illustrated in Figure 2.9a (compare Table 3 in the Appendix for the exact values of the maximum velocities and the acceleration factors). Thus, the difference in kinetics during collapsing and swelling of each sample results in a hysteresis.

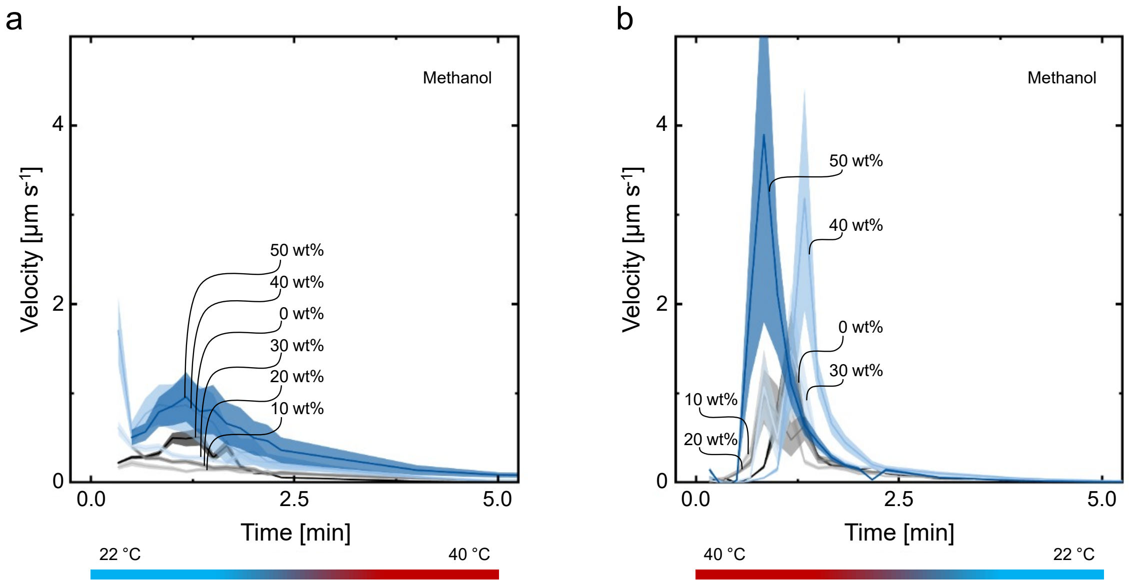

Figure 2.9: (a) Collapsing and (b) swelling velocities of rod-shaped PNIPAM microgels over time. Samples contained different methanol contents (0–50 wt%) in their reaction solutions during microgel fabrication using SFL. Errors are presented as colored regions around the respective curves.

As previously reported for PNIPAM, inter- and intra-chain hydrogen bonds may cause this hysteresis. These hydrogen bonds form above the lower critical solution temperature (LCST) during collapsing but dissociate only at temperatures much lower than the LCST during swelling, resulting in a difference of collapsing and swelling in the overall reversible process. [Chen2006; Lu2010; Sun2008] Due to their different porous structures induced by the cononsolvency effect during fabrication, the microgels' thermal responses differ. However, the swelling mechanism remains the same for all observed microgels.

2.3.5 Swelling Patterns

During the collapsing and swelling, not only the velocities but also the outer contour and shape of the microgels vary. Almost all microgels collapse evenly, retaining their shape over the whole process and displaying a uniform structure throughout the microgel. On the contrary, the swelling is irregular without a consistent shape but rather a temperature-dependent outer structure. Furthermore, distinct swollen and collapsed regions form within one microgel, resulting in an inner microgel structure. Different irregularities are observed and categorized in swelling patterns, shown in Figure 2.10. The observation of irregular swellings correlates with the swelling mechanism of spherical PNIPAM microgels reported by Cheng et al. [Chen2006] in which the microgel shell swells more than its core during the initial swelling phase.

Swelling is, on average, 3.5 ± 1.1 times faster than collapsing of the respective sample. During swelling, microgel samples with 0, 30, 40, and 50 wt% methanol during fabrication show an irregular swelling, whereas 10 and 20 wt% swell regularly with an even shape expansion in all directions, having regular inner and outer structures irrespective of temperature (Figure 2.10c). Thus, the swelling behavior is related to the methanol content during microgel fabrication. Moreover, these irregular swellings are related to an increased collapsing degree and higher collapsing and swelling velocities, as the same microgel variants show all these characteristics.

Depending on the methanol content, the swelling phenomena differ. For 40 and 50 wt% methanol, the so-called bone-like swelling is observed (Fig-

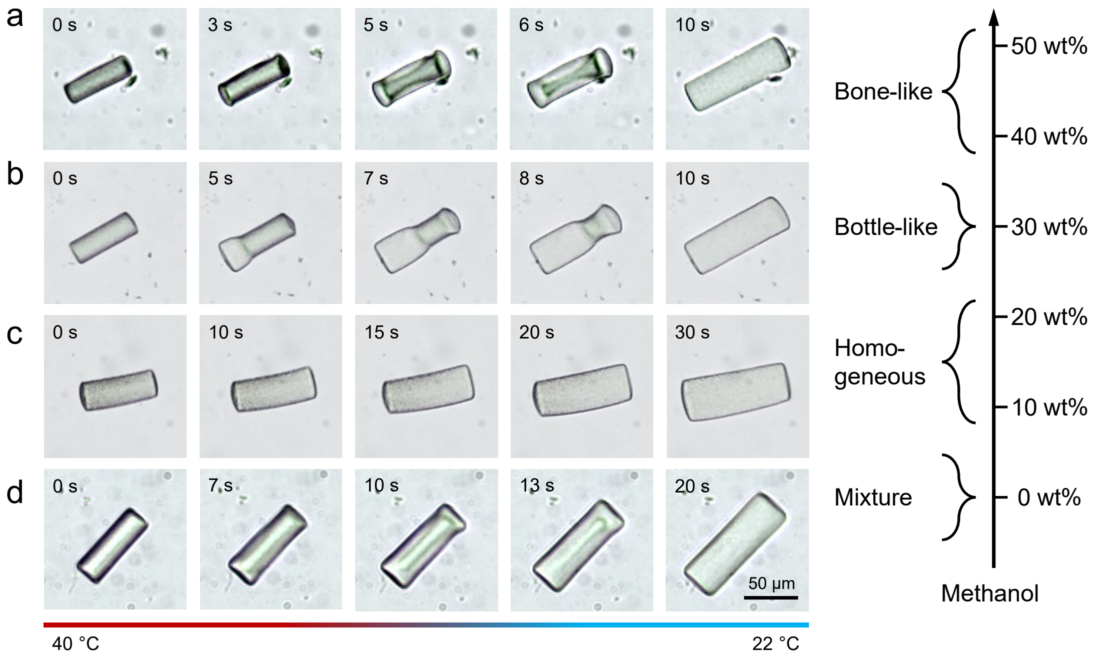

Figure 2.10: Swelling phenomena - Picture series of swelling processes of microgels fabricated with (a) 40 wt%, (b) 30 wt%, (c) 20 wt%, and (d) 0 wt% methanol in the reaction solution. Examples of irregular swelling patterns depend on the methanol content during fabrication.

ure 2.10a). Swelling starts at the thin sides of the gel and continues even stronger in the middle of the long sides, leading to a bone-like collapsed structure in the middle of the microgel, whereas the surrounding gel network is already swollen. This bone-like structure dissolves in the further swelling process, resulting in the homogeneous initial rod shape of the microgel. This swelling phenomenon can be reasoned by the water and, thus, heat diffusion limitation in the middle of the microgel during swelling, causing a time-delayed swelling in this region.

For the 50 wt% microgel sample, not only did the swelling reveal irregular microgel patterns, but during its collapse, the bone-like structure was also observed. These irregularities during collapsing might result from the comparatively high collapsing velocity of the 50 wt% microgels which lies in the order of the swelling velocity of the 20 wt% microgels (compare Table 3 in the Appendix).

Another observed swelling phenomenon is called bottle-like swelling and occurs for 30 wt% microgels, which is exemplarily shown in Figure 2.10b. Here, the thin microgel sides swell time-shifted instead of beginning simultaneously, whereas the swelling process does not proceed from the long sides of the gel. Hence, a bottle-like microgel structure arises with a thin collapsed area between the long sides of the microgel, while both areas related to the thin sides of the microgel are already swollen.

The positioning of this collapsed area is likely determined by the focus plane of the UV light during microgel fabrication via SFL. According to Dendukuri et al. [Dend2008], the homogeneity in microgel conversion during stop-flow lithography mainly depends on the molar extinction coefficient of the photoinitiator, its concentration, and the channel height due to the light's focus. By contrast, the reactivity difference between the crosslinker and the monomer is less relevant for light-induced polymerization compared to fabrication methods like precipitation polymerization. Thus, homogeneity distributions within microgels fabricated via SFL mainly depend on the focus applied during fabrication. [Haki2014; Kim2011]

In this work, the focus is set with respect to a homogeneous but highly focused light over the entire channel height, resulting in minor differences in the radiant power along the channel height and, thus, along the length of the microgels during fabrication. Hence, the occurrence and shift of the collapsed area arise from an increased power as a consequence of the focus and, thus, a denser crosslinking at this plane. Even if this effect induced by the SFL process becomes visible in combination with the cononsolvency effect, its influence remains the same for all samples, and thus, these can be compared with regard to the varied methanol content only.

The 0 wt% microgel sample without methanol in the SFL reaction solution shows a mixture of bone-like and bottle-like swelling phenomena (Figure 2.10d), beginning to swell on one thin microgel side, but results in a collapsed bone-like structure within the microgel.

The observed shape effects occur almost exclusively during swelling and are related to the methanol content of the microgel samples. These dependencies fit the previous observations regarding collapsing degree and collapsing and swelling kinetics.

The introduced cononsolvency-driven procedure allows the systematic fabrication of anisotropically swelling microgels with domains of varying density and aggregation. Such distinct domains within microgels are of special interest for a variety of applications, such as micrometer-scale targeted folding [Yin2022; Zhan2017], active swimmers [Mour2021; Wisc2020], and locally induced contractions for cell growth [Schm2010; Chan2019], among others [Zhan2018; Garc2020; Chen2021; Xue2017].

2.4 Conclusion and Outlook

In this work, a new fabrication procedure is established to tune the porous structure of thermally responsive rod-shaped PNIPAM microgels. The cononsolvency effect was used during microgel fabrication by replacing water as solvent in the reaction solution with a mixture of water and methanol with different contents of methanol from 0 to 50 wt%. Furthermore, stop-flow lithography as a fabrication method enables the realization of microgels of complex shapes in high throughput.

Depending on the methanol content, the microgel characteristics changed. Noticeably, during fabrication, the parameters needed for a successful polymerization and the qualitative stiffness of the microgels varied. Electron microscopy imaging showed deviating porous structures between microgels with and without methanol influence. Furthermore, the microgels' thermoresponsiveness was affected by the new fabrication procedure. The microgel length of the swollen state increased with increasing methanol content, whereas the length of the collapsed state decreased. This resulted in an enhanced degree of collapsing with an increase in the methanol content during fabrication. Thereby, the microgel length was more affected than the width, causing elongated microgels with higher aspect ratios, both in the swollen and collapsed states, as the methanol content increased.

The collapsing and swelling kinetics depended on the methanol content as well, whereas swelling shape patterns of the microgels occurred, which correlated with the methanol content in the reaction solution during fabrication. For high methanol contents of 40 or 50 wt%, bone-like swelling was observed. 30 wt% microgels showed bottle-like swelling, while samples with low methanol contents of 10 and 20 wt% swelled homogeneously without any pattern. Microgels fabricated without methanol exhibited a mixture of bone-like and bottle-like swelling, showing characteristics of both swelling patterns. These swelling patterns correlate with the swelling velocities observed for the respective samples since homogeneous swelling occurred for the slowest swelling microgels, whereas faster swelling microgels showed varying swelling patterns in correlation with their velocities.

Hence, the properties of anisometric PNIPAM microgels changed by the presence of varying methanol contents during fabrication via SFL. Their porous structure was modified, and consequently, their fabrication parameter, appearance, collapsing degree, and behavior during thermal response varied. This novel procedure enables the development of advanced microgels with tailored porous structure and increased and adjustable responsiveness for medical approaches and cell growth. Thus, injectable scaffolds can be generated with enhanced scaffold properties by applying the presented procedure. Due to the fabrication with SFL, implementing any other complex geometry is straightforward through the design of the mask geometry used in the SFL process. Hence, microgels of complex shape are feasible to further tailor the void spaces of these scaffolds in addition to the microgels' porous structure, achieving improved cell infiltration and proliferation.

3 Magnetic Actuation for Controlled Motion

Parts of this chapter have been published as:

Lea Steinbeck, Dominik L. Braunmiller, Hanna J. M. Wolff, Vincent Hüttche, Julia Wang, Matthias Wessling, Jérôme Crassous, John Linkhorst
Magnetically Actuable Complex-Shaped Microgels for Spatio-Temporal Flow Control, Advanced Materials Technologies, 2023
DOI: 10.1002/admt.202300044

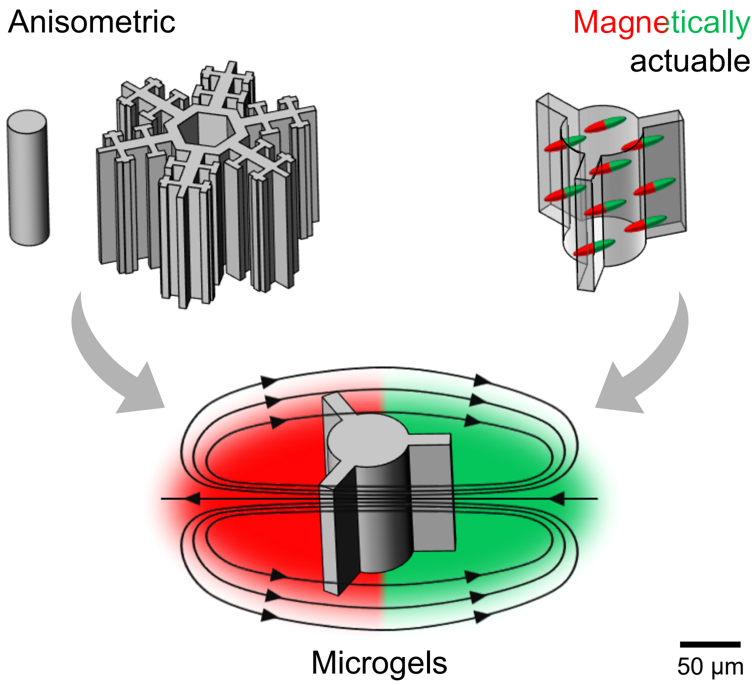

3.1 Introduction

Microgels that exhibit magnetic properties have drastically expanded the application fields of microgels. Magnetic microgels can be used for adsorption, as micromachines, for separation processes, or as microswimmers, among others. [Sanc2019; Alap2019; Sung2021; Mour2021] The magnetically-indued motion control of the microgels provides significant potential in architecting them in time and space.

Previous studies [Rose2017; Brau2022] show the alignment of magnetic microgels within the direction of a magnetic field to guide cell growth. These in vitro investigations have great potential to be translated into in vivo since a magnetic field has no adverse effects on tissues and penetrates them easily. [Babu2022] Besides a one-time alignment, magnetic microgels allow precise spatio-temporal motion control of the microgels. This characteristic can be exemplarily used to impact and regulate the microgels' environment and enable accurate flow control. Microfluidic flow control setups range from guidable colloids [Terr2002; Han2017] over pH-responsive valves [Beeb2000; Eddi2004] to pumping devices [Maru2006; Matt2006; Lei2007]. The initiative work in this field is the innovative microactuators presented by Beebe et al. [Beeb2000]. Magnetically-induced flow control is advantageous towards other triggers like pH, heat, electrics, optics, or mechanics since a magnetic actuation is less invasive. Hence, the magnetic response of microgels renders them ideal for diverse purposes like distinct flow control and structured cell scaffolds.

Magnetically responsive microgels are achieved by incorporating magnetic nanoparticles (NPs) inside the polymeric network of the microgels. These magnetic NPs often consist of iron oxide, such as hematite (α-Fe_2O_3), magnetite (Fe_3O_4), or maghemite (γ-Fe_2O_3). [Mahm2011] The magnetic properties of the NPs extend the properties of the microgels toward magnetic responsiveness due to the presence of the NPs within the microgels. [Hwan2008] The NP incorporation techniques differ in literature, ranging from a swelling entrapment [Yang2010] over a multi-step process with magnetic NP growth at functional sides [Suh2012b] to NP addition to the reaction solution [Hwan2008; Nune2010; Suh2012a; Haki2014; Rose2017; Babu2022].

Anisometric microgels with magnetic properties are advantageous compared to spherical microgels as they provide spatially directed influence on their environment. The fabrication methods of magnetic microgels with anisometric shape are comprehensive and comprise microfluidics [Hwan2008], particle replication in non-wetting template (PRINT) [Nune2010; Rose2017; Babu2022], maskless lithography [Lee2010], and stop-flow lithography (SFL) [Suh2012a; Suh2012b; Haki2014]. However, the magnetic moment of a microgel of an anisometric shape primarily follows the geometrically favorable axis of the microgel. [Rose2020a] Hence, the magnetic moment of anisometric microgels is predefined by their shape anisotropy. [Hwan2008; Rose2020b]

Only a few studies have overcome the limitation of the shape-defined magnetic moment orientation within anisometric microgels. [Nune2010; Brau2022; Saad2023] This is achieved by orienting the magnetic NPs and thereby defining the direction of the magnetic response of the NPs within the microgels. Therefore, a magnetic field is applied during the fabrication of the microgels to align the magnetic nanoparticles within the reaction solution prior to polymerization. Linear aggregates of the NPs form and are incorporated in the microgels by light-induced polymerization. This adaption enables anisometric microgels fabrication with predefined magnetic moments independent of the microgels' shape. The magnetic nanoparticles used are either spherical magnetite aggregates [Nune2010] or ellipsoidal maghemite nanoparticles [Brau2022; Saad2023]. The advantages of ellipsoidal NPs are their fixed magnetic moment along their longitudinal axis and their enhanced magnetic response. With increasing field strengths, ellipsoidal maghemite NPs align in dipolar chains with strong magnetic properties. [Mali2017; Itoh2003] The current studies show the introduction of a shape-independent magnetic moment within microgels fabricated via PRINT. [Nune2010; Brau2022; Saad2023] However, the magnetic microgels are coupled to the limitations of this method, like requiring several process steps and being limited in shape due to the mold design. [Liu2024; Haki2014]

This work expands the fabrication of anisometric microgels with predefined magnetic moments to SFL. This fabrication method allows the fabrication of magnetic microgels with high throughput and more complex shapes than previously published. Besides rod-shaped microgels, impeller- and snowflake-shaped microgels out of poly(ethylene glycol) diacrylate (PEG-DA) are realized. The direction of the magnetic moment within the microgels is predefined by adding ellipsoidal maghemite nanospindles to the reaction solution and applying a magnetic field during fabrication via SFL. In addition to the microgels' shape variation, their magnetic NP content and the polymerization parameters are altered. Depending on these differences, the magnetic response of the microgels is investigated by rotating them within an externally rotating magnetic field. The dependency of the microgel rotation rate is evaluated as a function of the rotation rate of the magnetic field for different microgel kinds and varying magnetic field strengths. Impeller-shaped microgels are additionally fixed inside a microfluidic device for their use as freely rotating actuators. Their induced flow control is evaluated using microparticle tracking velocimetry (µPTV).

3.2 Experimentals

Maghemite Nanospindle Synthesis Hematite nanospindles were synthesized with a defined size and aspect ratio and were subsequently reduced to magnetite and reoxidized to maghemite at high temperatures. The multi-step synthesis of the maghemite nanospindles ($60\,\mathrm{A\,m^2\,kg^{-1}}$ saturation magnetization [Mali2017]) was performed according to published protocols. [Ocañ1999; Brau2022] The nanoparticle size (260 ± 29.1 nm length, 51.2 ± 6.0 nm diameter) was confirmed using transmission electron microscopy (TEM) (Tecnai F20, FEI).

Microfluidic Chip Fabrication The microfluidic chips were fabricated by dip-in laser lithography for the master production and subsequent soft lithography (compare Section 2.2). All microfluidic channels, for fabrication, for in-chip rotation, and for in-chip pumping, are 15 mm long (x-direction) and 900 µm wide (y-direction). Figures 3.6a and 3.9a show scanning electron microscopy (SEM) (TM 3030 Plus, Hitachi) images of the channels for in-chip applications which have a height of 20 µm (z-direction) in contrast to the 80 µm high fabrication channel. The pillars (diameters of 15 µm) are spaced in a squared arrangement with regular distances to each other (209 µm in x- and 241 µm in y-direction). In the case of the pump housing chip, every second pillar is absent, and every second remaining pillar row is extended by a pump housing.

Reaction Solution Preparation The reaction solutions contained the pre-polymer poly(ethylene glycol) diacrylate (PEGDA) ($M_\text{n} = 575$ Da, with 400–600 ppm MEHQ as inhibitor, Sigma Aldrich), the initiator lithium phenyl-2,4,6-trimethylbenzoylphosphinate (LAP) (≥ 95 %, Sigma-Aldrich), maghemite nanospindles (2 g L^{-1}), and water (HiPerSolv CHROMANORM, VWR). The radical scavenger 4-methoxyphenole (MEHQ) (purum, ≥ 98 %, Sigma-Aldrich) was added to the reaction solution for the in-chip polymerization of microgels around pillars. The concentrated maghemite suspension was mixed with the respective water proportion and mixed in an ultrasonic bath (5 min). This water-maghemite solvent was added to the weighed pre-polymer and mixed before being added to the weighed initiator and mixed again. For in-chip polymerization, the radical scavenger was weighed out into a separate vial, and the pre-polymer solvent mixture was added to the radical scavenger prior to admitting the resulting mixture to the initiator.

Magnetic Microgel Fabrication using SFL Microgels were fabricated from reaction solutions containing PEGDA (20 wt%), LAP (0.5 wt%), maghemite ($\sim$0.08 wt%), and water in the presence of an externally applied magnetic field (13 mT). The maghemite content resulted from dissolving the concentrated maghemite solution in water (50:50 mixture). The stage setup shown in Figure 3.2a was used for the microgel fabrication using stop-flow lithography (SFL). [Wolf2020] Different transparency masks resulted in varying microgels shapes: circular rods (7 µm diameter), three-arm impellers (92 µm outer diameter), and snowflakes (100 µm outer diameter). Depending on the mask, the radiant power and exposure time during polymerization varied (rods: 1280 mW, 50 ms, impellers: 930 mW, 50 ms, snowflakes: 1280 mW, 60 ms). The snowflake-shaped microgels were additionally fabricated at high radiant power and short exposure time (1280 mW, 60 ms) and at low radiant power and long exposure time (130 mW, 500 ms). Further, rod-shaped microgels were fabricated with and without applied magnetic field, and impeller microgels were fabricated with varying maghemite contents (0.02 wt%, 0.04 wt%, and 0.16 wt% in addition to 0.08 wt%). After fabrication, the resulting microgel-containing solution was diluted with water (1:1). The microgels were sedimented (30 min), and then the supernatant was removed and replaced with water, repeated five times. Afterward, the microgels in water were stored at 4 ℃ until further use.

Visual Magnetic Microgel Analysis using FESEM The maghemite nanospindle integration was studied on dried microgels via field emission scanning electron microscopy (FESEM). Therefore, a silica wafer was sonicated in isopropanol (15 min) and then placed in an ozone oven (15 min). The microgels (20 µL) were dried on the wafer prior to being imaged using FESEM.

Free Rotation Analysis of Magnetic Microgels A microscope glass slide (22 x 22 mm, VWR) was sonicated in isopropanol (15 min) and then placed in an ozone oven (15 min). A well (0.24 mm height, 9 mm diameter) was created on the glass slide by two spacers (Secure-Seal™, Invitrogen). The glass slide with well was placed on a modified microscope (Axioscope, Carl Zeiss Microscopy Deutschland GmbH) and inside a magnetic field induced by a custom-made circular Halbach array (1 - 300 mT) with neodymium magnets. This Halbach array was mounted on a rotating stage (0.1 - 90 rpm) driven by a piezoelectric engine (PILine U651.03,

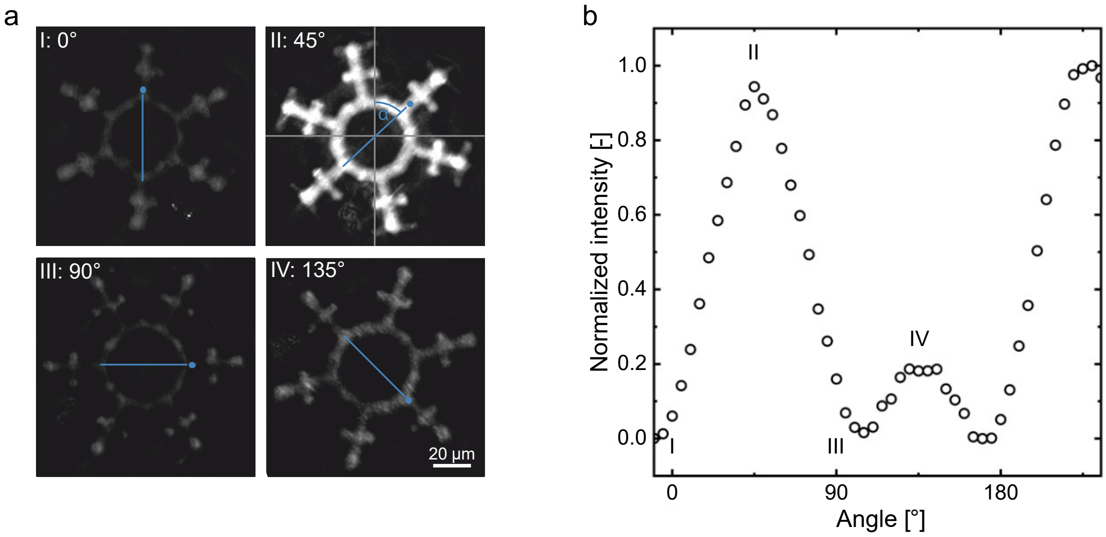

Figure 3.1: Analysis of the rotation rate of magnetic complex-shaped microgels using light polarization, exemplarily shown for a synchronously rotating snowflake-shaped microgel. (a) Micrographs of a snowflake-shaped microgel with different light polarizations depending on the rotation angle. The orientation of the polarizer is indicated by the gray lines, whereas the blue lines display the orientation of the maghemite nanospindles within the microgels, corresponding to the microgel rotation angle α. Scale bar (20 µm) applies to all micrographs. (b) Normalized light polarization intensity of the microgel applied over its rotation angle. Two large and two small peaks of 90° width each indicate a full rotation of a microgel, resulting in equal intensity values for angles with 180° difference.

Physik Instrumente). The microgels in water (9 µL) were inserted into the well, and their response to the applied rotating magnetic field was recorded (3600 frames, 100 fps). A linear polarizer was placed before the microgels, and an analyzer was positioned perpendicular to the polarizer after the microgels. Cross-polarization microscopy enabled the determination of the orientation of the light-polarizing dipolar maghemite chains within the microgels and, thus, the microgels' rotation rates. Therefore, the images were analyzed toward the intensity change of light polarization (ImageJ [Abra2003], custom-written Matlab routine), as shown in Figure 3.1. Around 20 microgels were investigated for each microgel kind.

In-Chip Immobilized Magnetic Microgel Fabrication Microgels around pillars were polymerized in a reaction solution containing PEGDA (20 wt%), LAP (1 wt%), maghemite (~0.08 wt%), MEHQ (0.5 wt%), and water. The three-arm impellers were fabricated using a magnetic field (13 mT) which was aligned to the microfluidic channel with the setup shown in Figure 3.2a. After fabrication, the reaction solution was exchanged against the flushing solution to avoid further polymerization inside the chip. The composition of the flushing solution was investigated to optimize the magnetic response capability of the microgels. The optimal flushing solution contains PEGDA (40 wt%), MEHQ (1 wt%), polyoxyethylene (20) sorbitan monolaurate (tween-20) (0.05 v%, Merck), and water.

In-Chip Flow Analysis For the in-chip rotation analysis, a custom-made setup with a motor-driven Halbach array (68 mT) was used. The influence of the magnetically induced in-chip rotation of the microgels on the surrounding fluid was investigated by microparticle tracking velocimetry (µPTV). This technique enables the quantification of fluid flows by tracking tracer particles. As tracers, fluorescent polystyrene microspheres (0.86 µm diameter, Rhodamine 6G dye, LaVision GmbH) were added to the flushing solution (0.07 v%). This seeded flushing solution was flushed into the microfluidic chip until it filled the whole channel. Afterward, the inlet pressure was increased to 1000 mbar, and the outlet pressure was raised until the fluid flow stopped. This procedure was visually observed through the stereomicroscope (SteREO Discovery.V20, Carl Zeiss Microscopy Deutschland GmbH) of the µPTV setup. After preparation, the rotation of the Halbach array was induced, and investigations started. During the measurement, a high-frequency Nd:YAG laser (532 nm, DM150, Photonics Industries International Inc.) induced the fluorescent response of the tracer particles, while two high-speed cameras (Phantom VEO 710L, Vision Research Inc.) recorded their movement. The setup is controlled by the software DaVis (version 10.0.5.47779, LaVision GmbH), which was also used for the image processing. With this software, particle tracks were processed to velocity fields, enabling the visualization of the fluid flow. A detailed description of the setup and the image post-processing is given in Stockmeier et al. [Stoc2022]

3.3 Results and Discussion

3.3.1 Magnetic Microgel Fabrication

To achieve anisometric, magnetically actuatable building blocks, maghemite nanospindles were integrated into complex-shaped PEGDA microgels using stop-flow lithography (SFL). The nanospindles added to the reaction solution were first aligned by the magnetic field of a Halbach array in a microfluidic channel as schematically illustrated in Figure 3.2a. The microfluidic chip was positioned in all three dimensions in the center of the Halbach array to ensure a homogeneous magnetic field in the polymerization area. In addition, the chip platform allows a controlled orientation of the surrounding Halbach array, enabling to set the maghemite orientation within the microfluidic channel. This way, complex-shaped microgels with a predefined magnetic moment were synthesized by SFL.

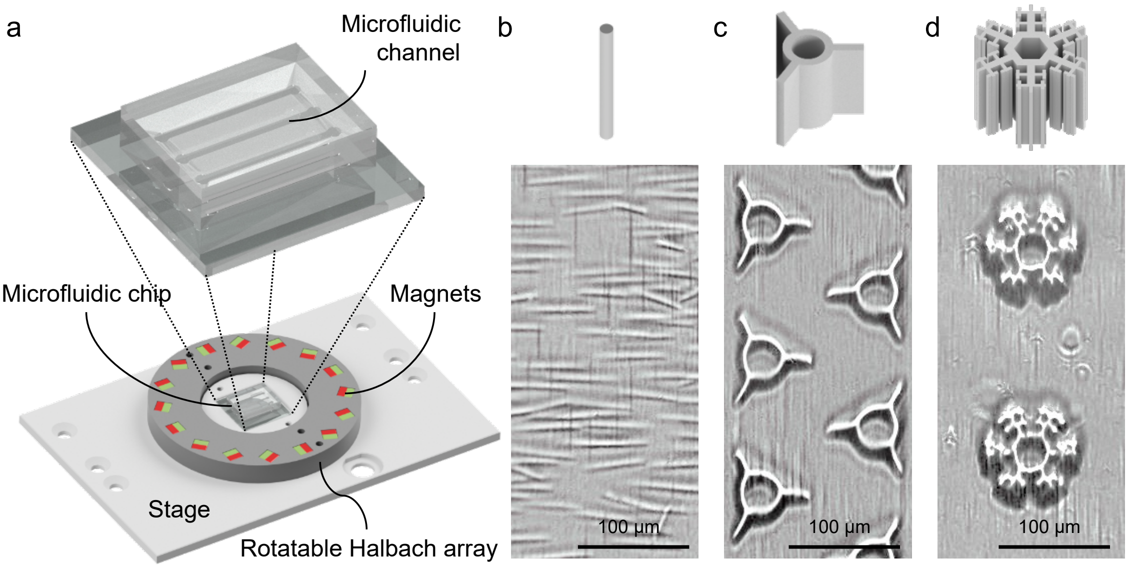

Figure 3.2: Fabrication of PEGDA microgels with integrated maghemite nanospindles. (a) Setup of the microgel fabrication (b-d) with the applied shapes and aligned maghemite nanospindles during microgel fabrication: (b) rod, (c) impeller, and (d) snowflake microgels. Scale bar (100 µm) applies to all micrographs.

To analyze the magnetic response, rod-, impeller-, and snowflake-shaped microgels were produced. In Figure 3.2b–d, the different microgels are displayed both as a schematic drawing and by a brightfield micrograph during fabrication (xy plane). In contrast to the images of the impellers and snowflakes, the rods were manually tilted to the side (from xz to xy plane) to visualize their rod shape in the micrograph. The applied magnetic field during fabrication causes an alignment of the maghemite spindles in the y-direction perpendicular to the microgels' longitudinal z-axis. Thus, when lying, the rods align perpendicular to the still-applied magnetic field due to their predefined magnetic moment (Figure 3.2b). This predefined magnetic moment is independent of the anisometry of the microgels but only depends on the maghemite nanospindle orientation within the microgels. The nanospindles have, in contrast to spherical nanoparticles, a direction-dependent magnetic response. Thus, by integrating maghemite nanospindles into the microgels, the direction of the magnetic moment of the microgels can be predefined by the applied magnetic field during fabrication.

The impellers were exemplarily characterized by scanning electron microscopy to evidence the presence of the aligned maghemite nanospindles. Figure 3.3 shows three magnifications of impeller-shaped microgels fabricated in the presence of maghemite nanospindles in the reaction solution. The highest magnification (compare Figure 3.3c) reveals the presence of maghemite nanospindles on the microgel surface. Individual nanospindles and dipolar chain formations are visible. These are aligned in the direction within the impeller-shaped microgels which is perpendicular to the microgels' height (z-axis). This alignment corresponds to the applied direction

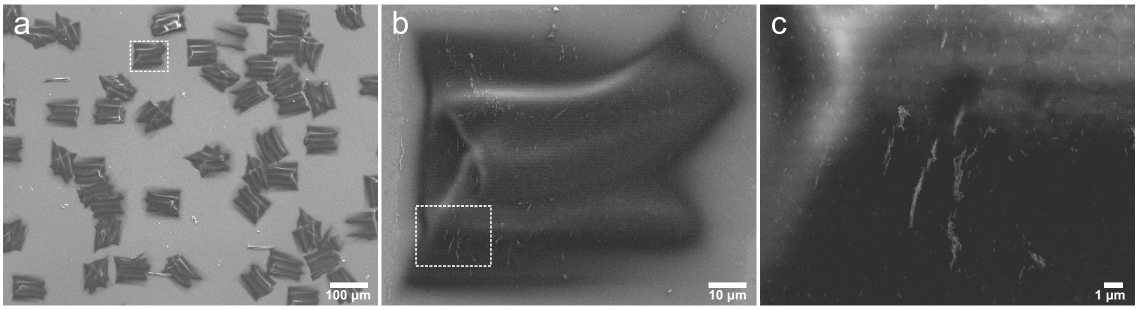

Figure 3.3: Electron microscopy images of impeller-shaped microgels with incorporated maghemite nanospindles (a-c) in three magnifications.

of the magnetic field during fabrication and demonstrates the successful aligned integration of the nanospindles inside or at least on the complex-shaped microgels.

Eleven microgel samples were fabricated, and their magnetic response was analyzed in terms of microgel shape, maghemite spindle alignment, polymerization parameters, maghemite content, and magnetic field strength. Whereas the influence of the microgel shape, the maghemite content, and the field strength are discussed in detail in the next section, the results for investigation of the maghemite alignment and polymerization parameter can be stated briefly:

The alignment of the maghemite spindles in the reaction solution showed to be crucial to enable a rotation of the microgels. Microgels that were fabricated without the alignment of maghemite spindles, meaning fabrication without a magnetic field, do not align uniformly with the magnetic field and show a weak magnetic response. In contrast, pre-aligning the nanospindles leads to a significant improvement in the magnetic response and enables the orientation of the microgels. Hence, the nanospindles need to be aligned during fabrication. Otherwise, no predefined magnetic moment will be created within the arising microgels.

Two polymerization parameter extremes were used during fabrication to test their influence on the magnetic response of the microgels. Long exposure time and low radiant power were applied for one sample, and for the other, short exposure time and high radiant power. The variation of the polymerization parameters does not influence the magnetic response of the fabricated microgels.

Regarding the two remaining fabrication factors, shape and maghemite content, the magnetic response was investigated in detail by determining the rotation rate of the different magnetic microgels as a function of the rotation rate of the magnetic field. The influence of the magnetic field strength was evaluated as an environmental parameter.

3.3.2 Magnetically Induced Rotation

The rotation of the magnetic complex-shaped microgels was realized by rotating an externally applied magnetic field around them. The microgels follow the magnetic field as the integrated maghemite spindles align along it. The microgels' rotation rate depends on the characteristics of the magnetic microgels, like their maghemite content and shape, and on the characteristics of the magnetic field, like its field strength and rotation rate.

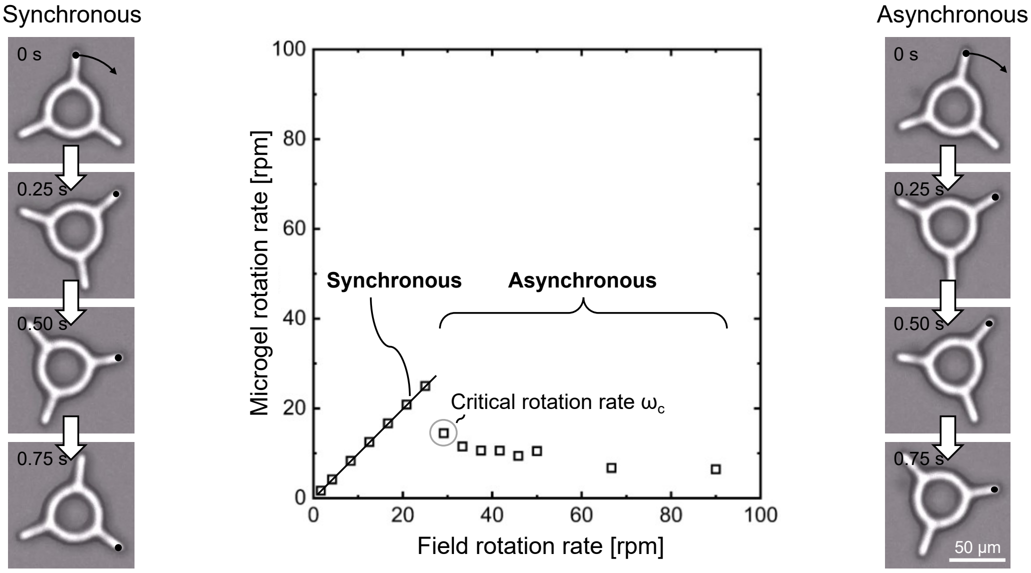

Figure 3.4: Rotation behavior of magnetically responsive complex-shaped microgels (impeller-shape, 0.08 wt% maghemite, 68 mT field strength). Synchronous and asynchronous rotation regimes are displayed as time-dependent image series and in the form of the microgel rotation rate. The transition between the regimes is indicated by the critical rotation rate ω_C. Scale bar (50 µm) applies to all micrographs.

For low rotation rates of the magnetic field, all microgels rotate synchronously, but above a critical rotation rate ω_C, the microgels show an asynchronous rotation. Figure 3.4 displays both rotation regimes as chronological micrographs and within a graph showing the microgel rotation rate over the field rotation rate for an impeller-shaped microgel with 0.08 wt% maghemite in a 68 mT strong magnetic field.

During synchronous rotation, the microgel rotation rate equals the field rotation rate in a linear correlation. Hence, the microgels can follow the rotating external magnetic field, and the integrated maghemite spindles are always aligned with the direction of the field. Asynchronous rotation is characterized by a lower microgel rotation rate than the field rotation rate. The magnetic moment induced by the orientated maghemite spindles within the microgel can not continuously follow the magnetic field. As a result, the microgel starts to rotate asynchronously. Within the asynchronous rotation regime, the microgel rotation is periodically reversed for a short time before the microgel rotates again with the rotation direction of the surrounding magnetic field as soon as this realigns with the microgels' magnetic moment by overtaking. Overall, the rotation proceeds with the rotation direction of the magnetic field but at a lower microgel rotation rate.

In the asynchronous regime, the angle between the magnetic moment of the microgels and the magnetic field is not constant, like in the synchronous regime, but it varies time-dependently. This is attributed to the frictional force and viscous torque that dominate the magnetic torque. The size of the contact area between the microgel and the underground surface mainly influences the frictional force between different microgels in this study, and a larger microgel volume increases the viscous torque. The magnetic field strength influences the emerging magnetic torque of the microgels. Furthermore, the magnetic torque is proportional to the amount of maghemite as the material that induces the magnetic response of the microgels. Consequently, the magnetic torque increases for microgels with a higher maghemite content in the reaction solution and for a larger microgel volume, both resulting in an increased maghemite amount per microgel. The characteristics of the magnetic microgels and the magnetic field influence the frictional force, the viscous torque, and the magnetic torque, determining the magnetically induced rotation behavior. The transition between these rotation regimes is marked by the critical rotation rate as the first value, where the rotation rates of microgel and magnetic field differ.

The rotation behavior of the magnetic microgels significantly distinguishes depending on the applied magnetic field strength, the maghemite nanospindle content within the microgels, and the microgels' shape. Figure 3.5 shows the influence of these varying parameters by displaying the microgel rotation rate as a function of the magnetic field rotation rate. Varying the parameters causes, among other differences, deviating critical rotation rates and, thus, shifted rotation regimes in relation to the field rotation rate. Table 4 in the Appendix lists all investigated samples' critical rotation rates.

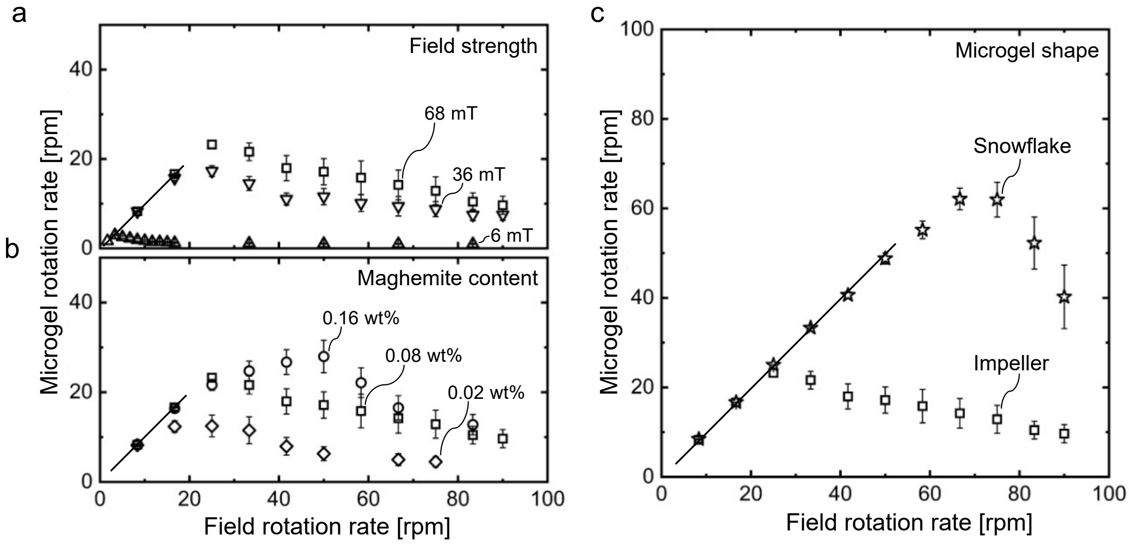

Figure 3.5: Magnetic response of complex-shaped microgels for varying (a) field strength, (b) maghemite content within the microgels, and (c) microgel shape. Unless otherwise specified, the microgels (n ≈ 20 each) are studied at a field strength of 68 mT, have a maghemite content of 0.08 wt%, and an impeller shape.

The magnetic field strength highly influences the rotation behavior of the magnetic microgels (compare Figure 3.5a). The higher the field strength, the higher the field rotation rates until which synchronous microgel rotation occurs. This effect is more pronounced between 6 mT and 36 mT than between 36 mT and 68 mT, and seems to be limited towards high field strengths.

An increased maghemite content also favors the occurrence of the synchronous regime (compare Figure 3.5b). However, the variation of the critical rotation rate between individual microgels within one sample also increases. This might be caused by a less defined structure of the dipolar maghemite chains when exceeding a certain content of magnetic nanospindles in the reaction solution, resulting in an inhomogeneous magnetic response. Hence, the effect of the maghemite content might be lower regarding the magnetic response.

Regarding the magnetic response of snowflake-shaped microgels compared to the impeller-shaped ones, their magnetic response is significantly stronger. The snowflake microgels show synchronous rotation at considerably higher rotation rates and by far exceed the magnetic response of all previous sample variations, as shown in Figure 3.5c. The snowflake-shaped microgels have an increased magnetic torque due to their larger volume, which results in an increased magnetic material within the microgels. However, the frictional force and the viscous torque are also increased, mainly depending on the larger surface contact area and the larger volume, and counteract the magnetic torque. As indicated by the rotation results, the contribution of the magnetic torque is stronger than the frictional force and viscous torque, leading to an enhanced rotation of the snowflake microgels. Since these relations are highly complex and hard to quantify, the shape influence can not be easily projected toward an ideal shape for magnetically induced rotation.

The findings on the rotation behavior enable the control and tune of the motion of magnetic microgels of complex shapes. Beyond that, this knowledge facilitates the microgels' transfer into microfluidic chips, using the magnetic microgels as static mixers.

3.3.3 In-Chip Integration of Actuatable Complex-Shaped Microgels

The fixed axis rotation of magnetic microgels was directly implemented by integrating them via SFL into a microfluidic chip with poly(dimethylsiloxane) (PDMS) pillars. Thus, the internal flow can be selectively influenced by the rotating microgels working as impellers. A microfluidic chip with pillars was fabricated to fixate the rotating impellers inside the channel. The pillars serve as fixation points for the impellers, allowing the microgels to rotate around a fixed axis. Figure 3.6a shows an SEM micrograph of the microfluidic channel made of PDMS in which the pillars are arranged in a square lattice.

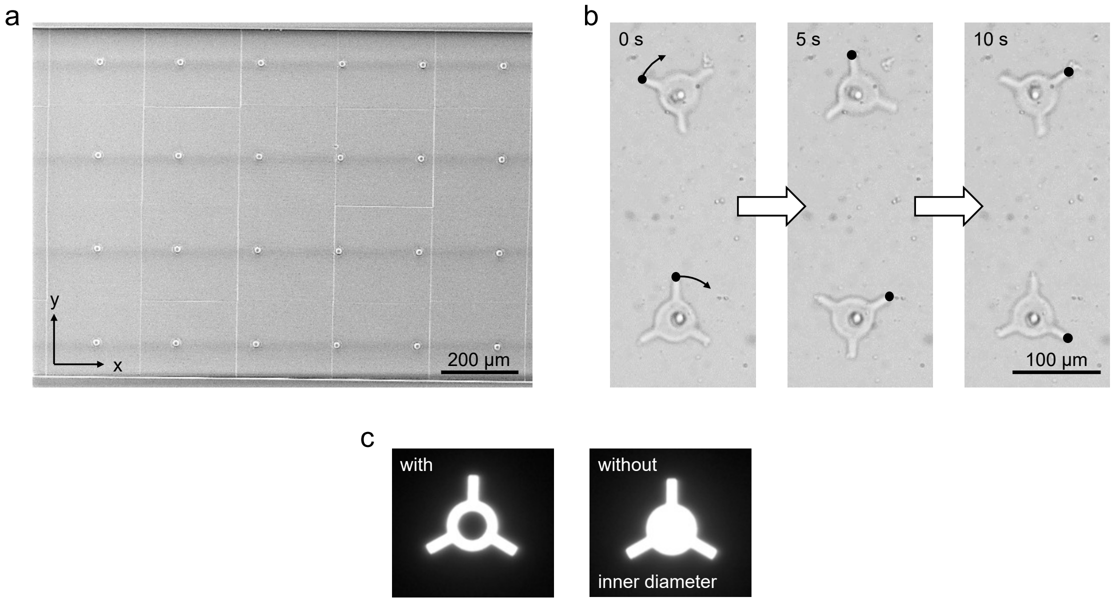

Figure 3.6: Integration and rotation of impeller-shaped magnetic microgels in-chip. (a) SEM micrograph of the microfluidic channel with PDMS pillars. (b) Time series of clockwise rotating impellers (without predefined inner diameter) around pillars in-chip. (c) Transparency mask shapes of impellers with and without inner diameter.

In order to find the right combination of diameters for the integrated pillars and surrounding impellers, two counteracting aspects have to be considered. On the one hand, the distance between the pillar and the surrounding microgel should be as small as possible to ensure a smooth and homogeneous rotation. On the other hand, the pillars and the microgel impellers must resist pressure during fluid flushing. As a result of the oxygen inhibition layer around the pillars during microgel polymerization, the pillar diameter has to be significantly smaller than the inner diameter of the impeller shape. Otherwise, oxygen inhibition reduces the impellers' wall thickness compared to the designated shape. Unfortunately, a larger inner diameter of the impellers allows tumbling and movement of the impellers around the pillars rather than homogeneous rotation.

To achieve a uniform short distance between pillar and microgel, microgel shapes without a predefined inner diameter are used for the fabrication around the pillars. Both impeller shapes, with and without inner diameter, are displayed in Figure 3.6c. Due to the oxygen inhibition layer surrounding the PDMS pillars, the microgels without inner diameter do not stick to the pillars. This results in the same microgel shape as microgels with a predefined inner diameter, but the distance to the pillars is reduced and even. Thus, the pillar diameter is kept small to ensure stable impeller walls, and the distance to the microgels is set by the oxygen inhibition layer. By using a microgel shape without inner diameter, the microgels are stable against fluid flushing and enable fixed rotation around the pillars.

For microgel fabrication, the channel is flushed with a reaction solution containing PEGDA, lithium phenyl-2,4,6-trimethylbenzoylphosphinate (LAP), maghemite nanospindles, 4-methoxyphenole (MEHQ), and water. Positioning the microgel polymerization areas in the exact spots of the pillars inside the channel is crucial to successfully fabricating homogeneous, intact, and rotatable microgels.

Two aspects were identified as obstacles to rotation: adhesion of the microgels to the channel and microgel swelling. Different flushing solutions were tested to address these challenges. To avoid further polymerization after fabrication, the reaction solution is exchanged with an aqueous solution containing 1 wt% MEHQ to hinder a potential ongoing polymerization by binding free radicals. Pure water as a flushing solution resulted in restricted or even no movement of the impellers and was, therefore, not used. To prevent adhesion, the surfactant tween-20 is widely used in microfluidics in droplet makers, but also reduces surface interaction in pipette tips. [Suh2012a] The addition of 0.05 v% tween-20 to the flushing solution was found to reduce sticking to the channel walls and allowed for better rotation stability. The osmotic pressure in the flushing solution was increased to avoid swelling and counteract an increase in the microgel size. Polymers or salts have previously been shown to reduce swelling effectively. [Bouh2018; Cava2017; Sade2012] In contrast to salts, using

PEGDA avoids introducing an additional component to the experimental system. Thus, PEGDA was added to the flushing solution with a concentration of 40 wt%, twice as high as in the reaction solution, allowing to keep the size of the impellers constant. However, the concentration of PEGDA cannot be increased too much, as the microgels would be constricted at the axis of rotation if they shrink further. The final flushing solution used in rotation experiments consists of tween-20, PEGDA (average molecular weight of 575 Da), MEHQ, and water, preventing further polymerization, swelling, and sticking of the microgels. Additionally, increased pressure during rotation experiments significantly increases the rotation ability, impacting sticking and swelling. The pressure widens the whole channel, resulting in more space for swollen microgels and possibly weakening the obstructive PDMS microgel connection.

The magnetic field must be aligned with the chip to induce a rotation of the fabricated microgel impellers. The strongest area of the Halbach array, which is in its center, needs to be at the same height as the microgels within the microfluidic channel, as discussed in Section 3.3.1. Ideally, the microgels are in the center of the Halbach array in terms of all three dimensions. This ensures that the magnetic field's strongest and most homogeneous part influences the maghemites within the impellers. This is realized by a setup designed for this purpose. Further, the Halbach array in this setup is motor-driven, allowing precise rotation rate adjustment clockwise and counterclockwise.

Figure 3.6b shows the time series of an in-chip clockwise rotation of the impeller-shaped microgels. For a rotation rate of the magnetic field of 2 rpm induced by the surrounding rotating Halbach array, the microgels rotated with 1.9 ± 0.1 rpm, corresponding to the applied magnetic field rotation. Due to the Halbach array, the magnetic field within the microfluidic channel is highly homogeneous, applying the same force on each impeller-shaped microgel independent of its location within the channel.

Impeller microgels were polymerized around a total amount of fifteen pillars within the displayed channel. Thereby, no impeller stuck to the channel walls. One impeller was hindered in its rotation by other unfixed microgels sticking to it, and another impeller did not follow the rotating magnetic field, although it was not sticking but was free around the pillar. The other thirteen impellers inside the presented channel rotated with the rotation rate of the applied magnetic field, which was set under the critical rotation rate of the microgels. A total of fifteen microfluidic channels were fabricated after improving the system and studied during the course of this work. Movable microgels could be observed in nine of these fifteen channels. In the other six channels, the microgels were mobile directly after fabrication but subsequently stuck to the PDMS. This might be caused by a decreased time interval between oxygen plasma bonding and microgel fabrication for these six PDMS channels. This decreased time interval influences the formation of an oxygen inhibition layer during fabrication and results in the sticking of the microgels. The adapted fabrication procedure, the post-treatment, and the rotation conditions reliably enable a homogeneous and even microgel rotation.

In addition to observations of the rotation of the magnetic microgels, microparticle tracking velocimetry (µPTV) analysis was performed, investigating the fluid movement induced by the rotating impellers. In Figure 3.7a, single fluorescent particles in the fluid and their velocities are shown. The microgel impellers and pillars are schematically illustrated. Near the microgel impellers, rotating movements of the measured particles are observed in circular flow patterns. Figure 3.7a and b show different analyses of the same rotation experiment, velocities of individual particles, and a velocity field, respectively. The rotation rate of the magnetic field was set to 15 rpm, and a pressure of about 1 bar was applied on both sides of the microfluidic channel.

Figure 3.7b demonstrates that the magnetically induced microgel rotation impacts the surrounding fluid inside the microfluidic chip. A field with

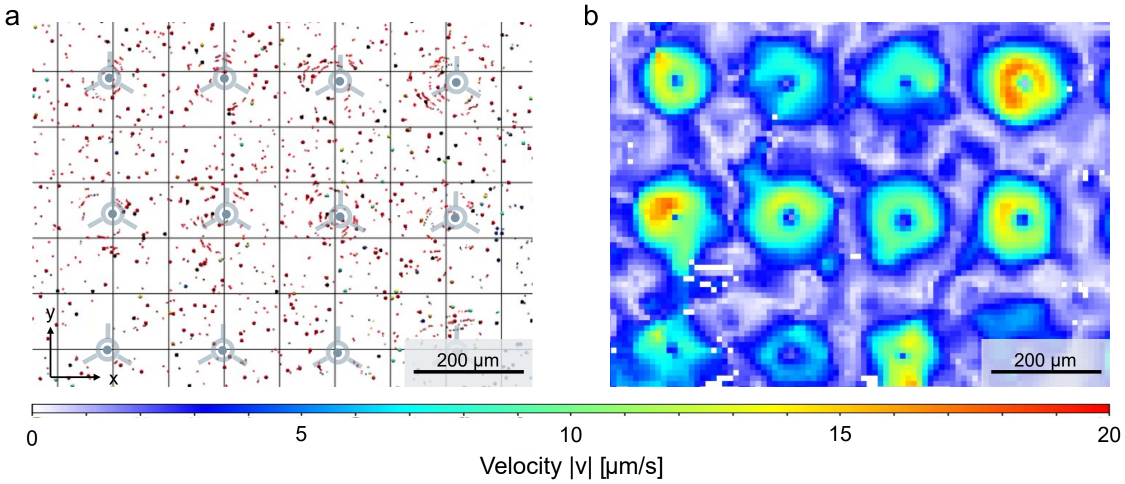

Figure 3.7: Magnetically induced rotation of impeller-shaped microgels causes fluid movement in-chip. (a) Microparticle tracking velocimetry (µPTV) flow analytics showing particle transport induced by rotating impellers, which are schematically illustrated. (b) µPTV image with analyzed flow velocities.

twelve rotating microgels is displayed, showing the same section as in Figure 3.7a. In the center of each microgel, at the position of the fixed PDMS pillars, no particle movement is detected. Around the pillars, particle velocities up to 20 µm s^{-1} were detected, indicating mixing of the fluid in the region of the microgel impellers and even slightly beyond. An average diameter of about 160 µm around the pillars is affected by the rotating impellers, which is 60 % larger than the outer diameter of an impeller. The highest velocities are detected at the impeller body in their arm regions. The tracer particle movement decreases with increasing distance from the microgel. Between the rotating impeller-shaped microgels, nearly no fluid movement is present, demonstrating the effect of the flow being induced by the magnetically actuated rotation.

In the future, the field of mixing can be further increased by adapting the pillar arrangement by varying the pillars' distance or their pattern. Therefore, the microfluidic master design can be easily changed. Like this, a locally distributed and potentially more extensive mixing can be achieved in future investigations. Moreover, the microgel shape can easily be varied by changing the transparency mask in the SFL setup. Hence, the fluid displacement can be increased by optimizing the impeller shape of the microgels. Exemplary improved shapes are shown in Figure 3.8. Such im-

Figure 3.8: Possible impeller shapes without inner diameter, which can be exemplarily used for in-chip mixing. The (I) original impeller design is modified by increasing (II) the blade length, (III) the number of blades, and (IV, V) changing the shape of the blades from straight to shovel-like.

provements might comprise an increased blade length (II) to enlarge the radius of mixed fluid around each impeller. An other possiblity to increase the impact of each impeller on the fluid motion is to fabricate impellers with more blades (III). Furthermore, the shape of each blade might significantly influence the microgels' impact on the surrounding fluid. Shovel-like blades (IV, V) potentially improve the fluid displacement and additionally stabilize the impeller due to thicker blade regions near the center of the impellers.

The developed magnetically actuatable microfluidic system might have the potential for additional applications besides the presented mixing, such as microfluidic pumping. A proof-of-concept of particle pumping is performed including a novel microfluidic chip design and first rotation experiments, shown in Figure 3.9. In comparison, the pumping chip has half of the pillars of the mixing chip since every second row is absent. Instead, pump housings are incorporated at every second row of the remaining pillars. Thus, alternating areas of pumping and mixing originate. The respective channel design is shown in Figure 3.9a.

Figure 3.9b shows the successful integration of magnetic impeller-shaped microgels in the microfluidic pump housings. Due to the high amount of PDMS at the pumping areas, higher shear rates appear during the exchange of the reaction against the flushing solution. This results in microgel deformations within the pump housings. Nevertheless, the impellers suc-

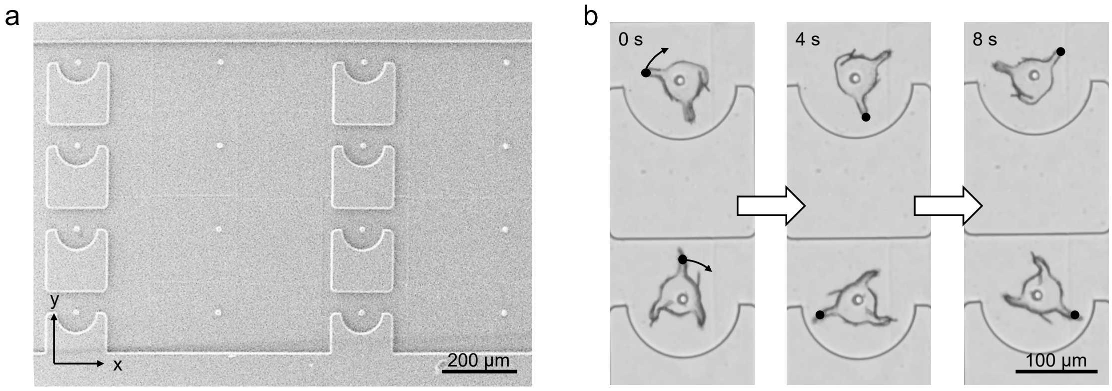

Figure 3.9: Active microfluidics and induced pumping and mixing by rotating impellers. (a) SEM micrograph of the microfluidic pump housing. (b) Incorporated impellers in housing showing a time series of clockwise in-chip rotation.

cessfully rotate, displayed by a time series of their rotation with a rotation rate of 10 rpm, which corresponds to the rotation rate of the applied magnetic fields.

The achieved rotation rates of the impellers in-chip for both application kinds are considerably lower than the critical rotation rate of the same microgel kind investigated in free rotation (compare Section 3.3.2). This discrepancy is most likely mainly caused by significantly increased frictional forces within microfluidic chips resulting from their narrowed height. The pumping design demonstrates that the novel active microfluidic system is easily adaptable for further in-chip applications. This is achieved by only changing the microfluidic master design without other adaptions of the fabrication process. Hence, the channel design and the microgel shape are replaceable, resulting in various new application possibilities without additional effort regarding the fabrication process.

In conclusion, a stable and reproducible actuatable microfluidic system was developed for spatio-temporal flow control. Polymerization around fixed pillars produced magnetic microgels in a microfluidic device at precise positions. This novel system is generated in one single step by polymerizing the microgels directly at their final position without further synthesis steps. The rotation of these magnetic impeller-shaped microgels is induced by the rotation of a Halbach array's external magnetic field, causing the surrounding fluid's actuation. While there are some limitations remaining in the system, it demonstrates the potential of precisely integrating magnetic actuators with a strong magnetic moment as actuatable microfluidic elements.

3.4 Conclusion and Outlook

This work presents a detailed study of complex-shaped microgels with introduced magnetic responsiveness with a predefined magnetic moment. The magnetic response of the microgels was achieved by integrating maghemite nanospindles in the reaction solution during the fabrication process via SFL. By aligning the ellipsoidal nanospindles within a magnetic field prior to polymerization, the magnetic moment within the microgels is predefined instead of being determined by the microgels' anisometric shape. A contactless actuation of the fabricated microgels is enabled by using an external magnetic field, precisely controlling the motion of the complex-shaped microgels.

The magnetic responsiveness of these microgels was investigated under a rotating magnetic field. The magnetic microgels synchronously rotate with the rotation rate of the externally applied magnetic field up to a critical rotation rate, which depends on their magnetic response. The influences of maghemite alignment, polymerization parameters, microgel shape, maghemite content, and magnetic field strength on the microgel actuation were studied. The alignment of the maghemite nanospindles during fabrication is crucial to achieving a spatially directed response of the magnetic microgels, whereas the polymerization parameters have no influence on the microgels' magnetic response. An increased maghemite content within the microgels and an increased magnetic field strength both result in an enhanced magnetic response of the microgels. The microgel shape considerably influences their rotation ability, with snowflake-shaped microgels showing significantly higher rotation rates than impellers.

In addition to analyzing freely rotating magnetic microgels, these were integrated into a microfluidic chip, creating an actuatable microfluidic system. This system was developed in a one-step process where the microgels are directly fabricated in a microfluidic chip containing PDMS pillars serving as fixed rotation axes. In the case of a transparency mask with impeller shapes without an inner diameter, the hydrophilic microgels are tightly located around hydrophobic PDMS pillars. The gap between the static pillars and the rotating microgels results from the oxygen inhibition layer surrounding the PDMS pillars, ensuring stable microgel rotations around the axes. These integrated magnetic impeller-shaped microgels actively mixed their surrounding fluid inside a microfluidic channel, thus enabling spatiotemporal flow control remotely actuated by a rotating magnetic field.

The strategy to precisely position the axis of rotation of microgels in a microfluidic chip offers the possibility of creating more advanced microfluidic designs with movable and actuatable elements that could be adapted for various applications, from microfluidic valves and pumps to particle sorting. Magnetically actuatable microgels in solution provide promising building blocks for scaffolds in the field of tissue engineering, as shown in recent publications. In the literature, cell growth guidance was demonstrated for aligned rod-shaped microgels. The complexity of the microgels' shape provided by the method presented in this work enables the tailoring of the void spaces in such aligned scaffolds and, thus, possibly further enhances this specified application.

4 Patterned Crosslinking for Designed Architecture

Parts of this chapter have been published as:

Lea Steinbeck, Richard Paul, Julia Litke, Isabel Karkoszka, G. Philip Wiese, John Linkhorst, Laura De Laporte, Matthias Wessling
Hierarchically Structured and Tunable Hydrogel Patches: Design, Characterization, and Application, SMALL, 2024
DOI: 10.1002/smll.202407311

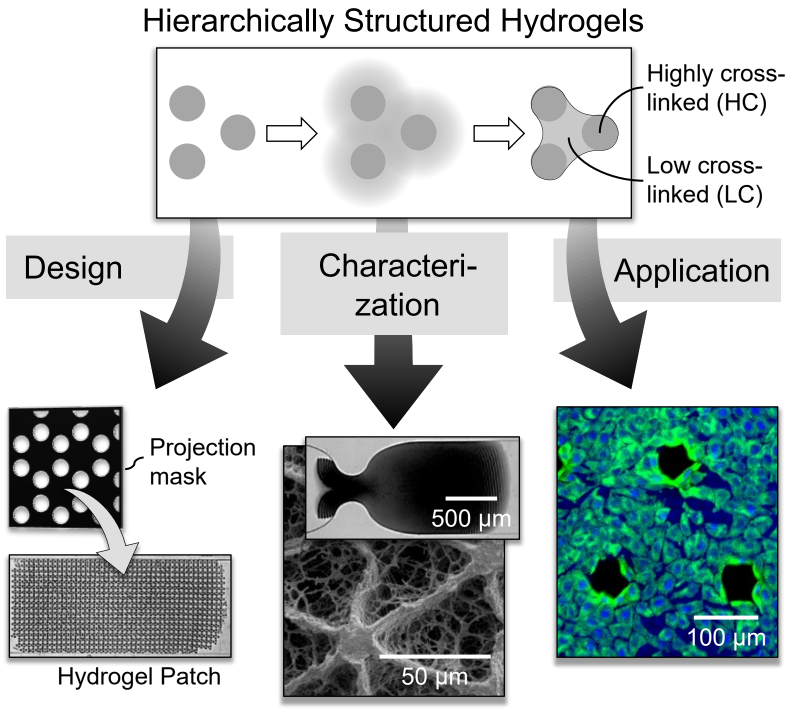

4.1 Introduction

Hydrogels are a group of functional materials that consist of crosslinked polymer networks and that drastically swell in water or other solvents. With their beneficial attributes such as their tunable size, porous network, responsiveness to external stimuli, and biocompatibility, they show great potential to meet challenges in optics, separation and transport processes, and tissue engineering, among others. [Agra2018; Aize2020; Choi2011; Gera2023; Liu2024; Xion2022; Yazd2020] To provide a high level of complexity within these functional materials, not only the material itself but also the structure of the hydrogels is essential. [Aize2020; Gera2023] Recent studies show the benefits of an anisometric geometry of hydrogels, like an improved diffusion efficiency or an increased attachment area due to the increased surface-area-to-volume ratio of anisometric hydrogels. [Tian2020; Liu2024] When the hydrogel geometry is designed, structure-dependent applications such as encryption units, micromotors, or cell guidance become possible. Complex hydrogel structures further enable a more suitable adaption of the hydrogels to their desired purposes and, thus, more successful applications in general. [Qazi2022; Liu2024; Gjor2022; Tian2020]

Especially for biomedical applications, highly structured hydrogels are of great relevance, as they can, for example, significantly influence cell interactions, migration, tissue shape, and drug delivery. [Liu2024; Gjor2022; Bril2023; Solb2023] The hydrogels then establish the microenvironment for cells during these applications. In turn, the cell behavior directly relates to the mechanical and topographical characteristics of the surrounding microenvironment. It is desirable to engineer the characteristics of the hydrogels to the natural niche of the cell type of interest. [Bril2023; Babu2021; Kitt2023]

Mechanical characteristics comprise, for example, the stiffness of the hydrogel scaffolds, which can change the cells' morphology, mobility, proliferation, or gene expression, altering cell differentiation. [Janm2020] The stiffness of a hydrogel polymer network is related to its crosslinking degree and its pore characteristics, i.e. pore size, degree of porosity, heterogeneity, and 2D and 3D topology. A versatile process to control such features all at the same time is also desirable to meet the needs of biomedical applications. Pore size and degree of porosity additionally influence the diffusion of nutrients and other essential supplies to cells and the removal of metabolic products, ensuring the sustained maintenance of the cells. [Raj 2023; Babu2021]

In addition to the stiffness, adherent cells require a substrate of suitable surface topography and macroporosity, which enables cell adhesion and in-growth similar to the natural extracellular matrix. Therefore, void spaces between hydrogel structures in the size of the cells and larger are essential for cell infiltration. The shape and size of these void spaces significantly influence the cells' behavior. [Gera2023; Romm2022; Qazi2022] Beyond that, the topography can stimulate the cells and instruct cellular reactions and cell fate. [Unad2011] In larger architectures, the topography helps to recreate the physiological complexity of the microenvironment of the cells and to mimic natural structures such as organs. [Ouya2020; Yavi2022] Hence, for all hydrogel applications, particularly in biomedicine, it is essential to precisely define the crosslinking degree on the molecular level as well as the architecture of individual hydrogels or their assemblies in the micrometer range.

In recent years, various methods have been developed and established to meet these structural challenges. The probably most widely used approach to achieve structured hydrogels is the microporous annealed particle (MAP) assembly. [Grif2015; Miks2022; Sutu2022; Pfaf2024] Thereby, building blocks are crosslinked, which are often randomly arranged spherical microgels. [Gera2023] However, systems exist where the arrangement is not random but, for example, controlled via aspiration of single spherical building blocks, resulting in highly structured layers. [Weig2023] Although the packing of MAP scaffolds built from spherical microgels can be adjusted to a certain degree by adapting the microgels' arrangement or diameter, the respective assemblies are still limited in pore shape.[Gera2023; Bulu2023]

A variation in pore shape and interconnectivity is achieved by using non-spherical building blocks. [Qazi2022; Romm2022] Compared to ordinary spherical microgels, these anisometric building blocks offer several advantages, namely higher surface area, higher diffusion efficiency, and increasing porosity within assemblies. [Liu2024; Gera2023; Babu2021] Anisometric building blocks with additional features like being magnetically responsive [Rose2017; Brau2022], biphasic [Dend2007a], or amphiphilic [Hess2018] can be arranged in a partially controlled manner, resulting in an induced directionality, more homogeneous pore spaces, or more defined arrangements. Furthermore, a controlled stacking of single anisometric, complex-shaped building blocks can result in a structurally ordered assembly. [Cui2018]

Other approaches to achieving structured hydrogels are not based on assemblies of building blocks but rather on the patterning of larger hydrogel sheets by molding to achieve pockets [Gjor2022], geometrical patterns [Unad2011], curvatures [Call2023], or grooves [Pape2007]. Approaches with probably the most control and shape variety of hydrogels on a micron scale are based on lithography, enabling the creation of complex, coherent structures. [Lu2006; Gauv2012] These structures often display cellular structural elements as one of eight bioinspired structural design elements defined in literature. [Nale2015] However, these structures comprise only one degree of crosslinking within the polymer network separated by void spaces and lack gradients in the polymer.

Combining cellular and gradient structural elements by providing structured networks with defined regions of deviating crosslinking degrees would result in an even increased number of applications or an enhanced realization of existing applications like tissue engineering. Controlled topography and locally resolved porosity due to such 3D structures with various degrees of crosslinking might be used for cell guidance and induced cell behavior by local differences within the scaffold.

This work presents the fabrication and characterization of hierarchically structured hydrogel patches by stop-flow lithography (SFL), comprising cellular and gradient structural design elements. A transparency mask shapes UV light that initiates localized photopolymerization within a prepolymer-containing microfluidic channel. The features of the sheetlike hydrogels form by locally exceeding a particular input energy, resulting in at least two regions with variable crosslinking degrees. The internal structure and the crosslinking degrees of the patches can be adjusted. Hence, the presented fabrication method enables the fabrication of precisely structured hydrogels across many length scales. The patch formation is investigated for varied exposure parameters for two material systems based on poly(ethylene glycol) diacrylate (PEGDA) and *N*-isopropyl acrylamide (NIPAM). Additionally, the impact of mask parameters, such as spot diameter and distance, are studied for the NIPAM-based material system to determine reliable patch formation parameters. The porous structures of poly NIPAM (PNIPAM) patches with varying crosslinking patterns and degrees are visualized by field emission scanning electron microscopy (FESEM) after freeze-drying. Microfluidic compression and squeezing experiments are performed to characterize the impact of the patch patterns on their mechanical properties. Finally, since tissue engineering is a promising application for hydrogel patches, their usage as cell scaffolds is showcased for cultivating L929 mouse fibroblast cells in microtiter plate experiments.

4.2 Experimentals

Microfluidic Chip Fabrication The microfluidic chips for the patch fabrication, the compression experiments, and the squeezing experiments were all produced via the same method. Therefore, masters for microfluidic chips were CAD designed (Inventor Professional 2023, Autodesk) and produced with a two-photon lithography printer (Photonic Professional (GT) Printer, Nanoscribe GmbH) via dip-in laser lithography. The remaining resin (IP-S, Nanoscribe) was removed via two washing baths of 1-methoxy-2-propyl acetate (10 min, $\geq$ 99.5 %, Sigma Aldrich) and isopropanol (3 min, $\geq$ 99.9 %, Sigma Aldrich), respectively. To harden the printed structure, the masters were cured under UV light (365 nm, 6 h). The microfluidic chips arise from subsequently casting the masters with poly(dimethylsiloxane) (PDMS) (Dow Corning, Sylgard 184 plus curing agent, 10:1 (w/w)). After curing (60 ℃, overnight), the PDMS was detached and punctured at in- and outlet to achieve tubing holes. The PDMS was washed by sonication in isopropanol (5 min) and dried (RT, overnight). For the patch fabrication chips, a glass slide (52 x 76 x 1 mm, VWR) was coated with PDMS (200 µm thick layer) via a casting knife and cured (60 ℃, overnight). Then, the PDMS form was bonded on the coated glass slide via oxygen plasma activation (TePla 100 Plasma System, PVA). An uncoated glass slide was used for the fabrication of the compression and squeezing chips.

Reaction Solution Preparation Two material systems were used to fabricate hydrogel patches. The first one is based on the pre-polymer poly(ethylene glycol) diacrylate (PEGDA) ($M_n = 575$ Da, with 400–600 ppm MEHQ as inhibitor, Sigma Aldrich). The other one contains the monomer *N*-isopropyl acrylamide (NIPAM) (98 %, Acros Organics, recrystallized in hexane (99 %, VWR)) and the crosslinker *N*, *N*'-methylene bisacrylamide (BIS) (99 %, Sigma-Aldrich). Both material systems were initiated via UV-light (365 nm) irradiation of the photo-initiator lithium phenyl-2,4,6-trimethylbenzoyl phosphinate (LAP) ($\geq$ 95 %, Sigma-Aldrich). Water (HiPerSolv CHROMANORM, VWR) was used as a solvent solution. PEGDA patches that were used for cell cultivation were fabricated with the addition of the comonomer glycidyl methacrylate (GMA) ($\geq$ 97 %, Sigma Aldrich), hereafter referred to as PEGDA-GMA patches.

For the preparation of the reaction solutions, depending on the material system, the monomer NIPAM or the pre-polymer PEGDA (20 wt% each) were weighed in a vial (1.5 mL, Eppendorf) and water (77 wt% for PNIPAM, 79 wt% for PEGDA, or 78.8 wt% for PEGDA-GMA, respectively) was added. The initiator LAP (1 wt%) was weighed in a separate light-protected brown vial (1.5 mL, Eppendorf). In the case of the NIPAM material system, the crosslinker BIS (2 wt%) was weighed as well and added to the initiator vial. For the PEGDA-GMA patches, the comonomer GMA (0.2 wt%) was treated equivalently. Afterward, the dissolved monomer or pre-polymer solution was added to the initiator-crosslinker, initiator, or initiator-comonomer vial, respectively. This mixture was homogenized using a vortex mixer (Vortex Genie 2 Digital, Scientific Industries) (3000 rpm, 20 s). Subsequently, the vial was centrifuged (mini star silverline, VWR) (6000 rpm, 3 min) as the last preparation step of the reaction solution before hydrogel fabrication.

Patch Fabrication The hydrogel patches were fabricated via projection lithography inside microfluidic channels in a stop-flow mode, known as stop-flow lithography (SFL). A sketch of the setup is shown in Figure 4.2. A transparency mask below the microfluidic channel shapes the UV light (365 nm, LZ1-00UV00, LED Engin), which irradiates the reaction solution within the microfluidic channel (y: 900 µm wide, z: 80 µm high, x: 15 mm long). Thus, a photo-induced radical polymerization starts, which results in the formation of hydrogels. All PNIPAM patches were fabricated with identical exposure parameters (200 mW, 750 ms, equals 38 mJ mm^{-2}), except for the hydrogel formation study where the parameters were varied (compare Section 4.3.1). The PEGDA-GMA patches for cell cultivation needed higher radiant exposure due to the comonomer addition (900 mW, 800 ms, equals 181 mJ mm^{-2}). A continuous fabrication was achieved by applying an automated stop-flow mode. [Dend2007b; Wolf2020] Thereby, the resting fluid was exposed to fabricate hydrogels. Afterward, a pressure difference (OB1, Elveflow) across the channel enabled the flow of the hydrogels out of the window of exposure by opening a solenoid valve (Type 6724, Bürkert). Next, the valve is closed again to stop the fluid, and the cycle is repeated.

After fabrication, the reaction solution surrounding the hydrogels was exchanged against deionized water (10 L, 2x 24 h) via dialysis (Zellutrans, MWCO: 12–14 kDa, 25 mm flat width, 20 µm wall thickness, Carl Roth GmbH). The purification of the patches used for cell cultivation was performed by sedimentation. Therefore, the fabricated patches within the unpolymerized reaction solution were light-protectively sedimented (5 min). Then, the supernatant reaction solution was discarded, and the sedimented patches were washed with fresh water. This sedimentation and washing procedure was repeated two times for a total of three cycles. Until analysis, all purified samples were stored at 4 ℃.

Porous Structure Analysis To investigate the porous structure of the patches, the patches in water were transferred into a vial (DNA LoBind, 1.5 mL, Eppendorf), and excess water was carefully removed after sedimentation of the patches by using a pipette. The vial was sealed with sealing tape (parafilm, Heathrow Scientific) and perforated with a needle. The patches were frozen in liquid nitrogen by placing the vial into a filter cap bottle (150 mL, Christ) and attaching it to a freeze-dryer (alpha 1-4 LO plus, Christ) (2 h). The dried patches were imaged using a Schottky field emission electron microscope (FESEM) (SU5000, Hitachi).

Compression and Squeezing Experiments To investigate the mechanical characteristics of the patches, compression and squeezing experiments were performed for eight patch types (compare Figure 4.7). Therefore, each patch in water was compressed against a filter structure or squeezed through a constriction inside microfluidic channels. First, each patch was flushed into the respective channel. Therefore, the inside of a tubing (FEP, 0.79 mm ID, 1.59 mm OD, Darwin) was wetted with an aqueous polyoxyethylene (20) sorbitan monolaurate (tween-20) (Merck) solution (0.05 v%) to prevent the sticking of the patch. Via a connected syringe, the patch was aspirated into the tubing, and subsequently, the tubing was connected to the microfluidic chip and an inlet vial. The chip outlet was connected to an outlet vial. At the inlet as well as the outlet vial, pressure was applied via a pressure controller (OB1, Elveflow) to ensure a definite pressure difference across the microfluidic channel. Via minor pressure, the patch was flushed into the channel using the same aqueous tween-20 solution (0.05 v%), and the orientation of the patch was checked to exclude previous compression or squeezing. Figure 4.1a shows the experimental setup. Then, for both experimental kinds, a linear pressure ramp was applied on the patch (60 s), starting the compression or squeezing experiment. The pressure difference within the channel was set higher for

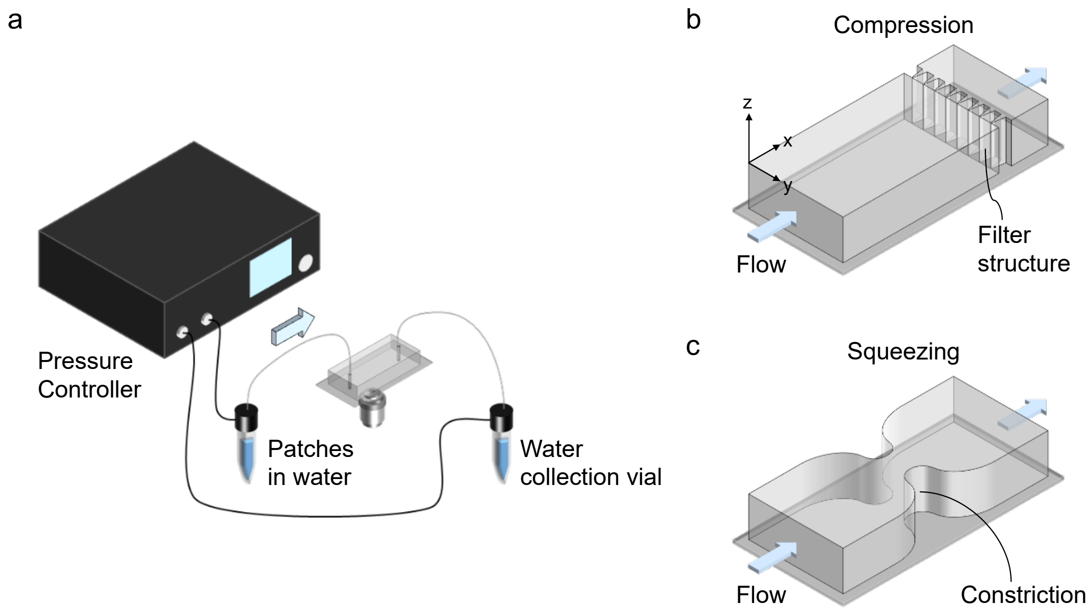

Figure 4.1: Schematic (a) setup to study the mechanical characteristics of patches via (b) compression against a filter structure or (c) squeezing through a constriction within the microfluidic channel.

the *structure* and the *directionality* patch types (0 - 1720 mbar) than for the *porosity* types (0 - 40 mbar).

Both channels (y: 900 µm wide, z: 80 µm high, x: 8 mm long) had the height and width dimensions of the patches. The schematic structures of the microfluidic channels are depicted in Figure 4.1b and c. The filter structure at the end of the compression channel had 5 µm wide pores (100 µm distance to the next pore, equals 8 pores), which covered the whole channel height (z: 80 µm). These pores restrained the patch and let fluid stream through, allowing pressure to build up on the patch and compressing it against the filter wall. The constriction within the squeezing channel had a width of 225 µm (y-direction), corresponding to a quarter of the channel and patch width. The compression or squeezing was investigated via an inverse light microscope (DM IL LED, Leica). During each experiment, a video and the matching pressure values were recorded. Subsequently, a micrograph was extracted (every 1 s) and binarized. The surface area of the patch within each micrograph was determined by an algorithm (Python) that counts every pixel displaying the patch in the binarized image.

Protein Functionalization of Hydrogel Patches Hydrogel patches were transferred into 12 well cell culture slides (81201, Ibidi) and washed three times with sterile phosphate-buffered saline (PBS) (1X, 200 µL, J62036.K3, Thermofisher) with resting times (5 min) between each washing step. For the functionalization of the PNIPAM patches, the PBS was aspirated and replaced by sulfosuccinimidyl 6-(4'-azido-2'-nitrophenylamino) hexanoate (sulfo-SANPAH) (803332-50MG, Sigma Aldrich) dissolved in dimethyl sulfoxide (DMSO) (A3672,0100 , ITW Reagents) (0.1 mol L^{-1}, 200 µL). The PNIPAM patches were exposed to UV light (365 nm, 5.2 mW cm^{-2}, 14 min, Analytik Jena) before being washed three times with sterile PBS (1X, 200 µL) with resting times (5 min) between each washing step. For both patch kinds, PNIPAM and PEGDA-GMA, the PBS was aspirated and replaced by a fibronectin solution (30 µg mL^{-1}, 200 µL, 10838039001, Sigma Aldrich) before incubating the patches (37 °C, 24 h). After the incubation and before cells were seeded, gels were washed three times with sterile PBS (1X, 200 µL).

Cell Cultivation L929 mouse fibroblasts (85011425, Sigma Aldrich) were cultivated in Gibco^{TM} high glucose Dulbecco's modified eagle medium (DMEM) (11965092, Thermo Fisher) supplemented with fetal bovine serum (FBS) (10 v%, 10-FBS-12F, Capricorn Scientific) and penicillin/streptomycin/amphotericin B (ABM) (1 v%, 15240062, Thermo Fisher). Cells were cultivated at 37 °C, 5 % CO_2, and 70 % humidity, subcultured at 80 % confluence, and the passage number was restricted to 25 subcultures. For a subculture, spent culture medium was aspirated, and cells were covered with trypsin-like protease (TrypLE^{TM} express enzyme, 12604013, Thermo Fisher) and incubated (37 °C, 5 min). Afterward, fresh culture medium (5-10 mL) was added, and cells were resuspended. The cell suspension was centrifuged (400 rcf^{-1}, 5 min), and the supernatant was aspirated carefully after centrifugation. Cells were resuspended in fresh culture medium and counted in a cell counting chamber with an automated cell counter (EVE^{TM}, NanoEntek) in a mixture (50 v%) with the dye trypan blue (0.4 %, NanoEntek). For experiments, a cell stock suspension (25000 viable cells/ mL) was prepared, which was added (200 µL) to each sample.

Immunofluorescence Imaging After two days of cultivation, immunofluorescent staining was performed to subsequently determine the cell area of individual cells. For cell fixation, spent culture media were aspirated, and each well was washed once with PBS (1X, 200 µL). The PBS was aspirated, and paraformaldehyde (PFA) (4 %, 200 µL, A3813,1000, ITW Reagents) was added and incubated (37 ℃, 20 min). Each well was washed once with PBS (1X, 200 µL) before 4-(1,1,3,3-tetramethylbutyl)-phenyl-polyethylene glycol (Triton^{TM} X-100) (0.1 v%, 150 µL, 15 min, Sigma Aldrich) was added to permeabilize the cell membranes. The wells were washed two times with PBS (1X, 200 µL) before a bovine serum albumin (BSA) blocking solution (1 v% in PBS, 150 µL, 126593-100GM, Sigma Aldrich) was added (RT, 30 min). The blocking solution was removed, and wells were washed two times with PBS (1X, 200 µL). Actin filaments were stained (60 min) with phalloidin-iFluor 488 reagent (0.1 v%, 150 µL, ab176753, Abcam). Afterward, wells were washed with PBS (1X, 150 µL), before staining (5 min) the cells' nuclei with 4',6-diamidino-2-phenylindole (DAPI) (0.4 v%, 150 µL, ab228549, Abcam). Wells were washed two times with PBS (1X, 200 µL) and stored at 4 ℃ under the exclusion of light until imaging. Imaging of the stained cell conditions was performed with confocal laser scanning microscopy (SP8 X, Leica) (excitation wavelength: 405 nm for DAPI, 488 nm for phalloidin).

Cell Area Calculation The cell area was determined with image processing software (1.54j, ImageJ). The scale bar in the exported microscopy images was used for software calibration. Images were transformed into 8-bit versions, and one color threshold was applied for all images. The wand tracing tool was used to outline individual cells and measure them subsequently. 70 ± 28 cells of each condition were considered for the cell area mean values of each condition with a minimum of 27 cells per condition.

Nanoindentation Mechanical properties of hydrogels were determined using a nanoindenter (Pavone, Optics11Life). A cantilever probe with a spherical tip (49.5 µm radius, 0.45 N m^{-1} stiffness) was installed. Hydrogels were functionalized with fibronectin (30 µg mL^{-1}) like for cell cultivation and submerged in fresh culture media (1 v% ABM, 10 v% FBS in DMEM, 24 h). The nanoindenter probe was calibrated in culture medium, and all indentations were performed at the same conditions (RT, 1 µm s^{-1} speed, 7 µm indentation depth). Each hydrogel condition was measured at least three times, always at different locations. The effective Young's modulus E_{eff} was derived from the recorded indentation curves using the Hertzian contact model via the device-associated data viewer software (V2.5, Optics11Life).

4.3 Results and Discussion

4.3.1 Hydrogel Patch Formation

Hydrogel patches are hierarchically structured hydrogel networks consisting of highly crosslinked (HC) and low crosslinked (LC) regions. The locations of the HC regions of the patches are defined by the transparency mask in the projection lithography fabrication process, inducing a localized polymerization within the reaction solution. The LC regions within the patches arise from light scattering and radical diffusion that is achieved by irradiating in a specific parameter range, depending on the transparency mask pattern. Within this range, the polymerization is not limited to the defined irradiation spots but additionally occurs to a lesser extent in the intermediate surroundings, where the reduced local energy leads to decreased crosslinking and the formation of the corresponding LC regions. Thus, a so-called hydrogel patch arises, consisting of an HC pattern defined by the transparency mask and connected by an LC polymer network.

The patches investigated in this work are about 2.25 mm long, 0.9 mm wide, and 80 µm high, which is defined by the dimensions of the microfluidic channel used for fabrication and the irradiation area of the projection lithography setup. By adapting these dimensions, the overall patch size can be varied. Using the stop-flow mode of the projection lithography setup provides a high-throughput fabrication ($>$ 50 patches/ min) of the patches. Figure 4.2 shows a visualization of the top and side view of a patch inside a microfluidic channel. The HC regions defined by the mask are visualized in dark gray, whereas the LC regions are light gray.

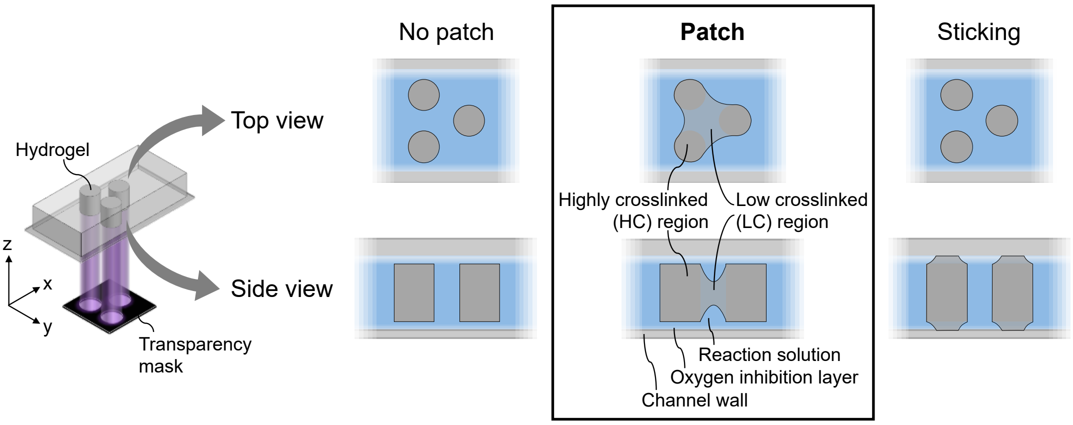

Figure 4.2: Hydrogel formation using mask projection lithography. Schematics of the hydrogel formation events, *no patch*, *patch*, and *sticking*, in the side and top view for a hexagonal spot arrangement, showing the network connections.

Besides *patch* formation, other formation events can occur, namely, *no patch* or *sticking*. *No patch* means the formation of hydrogels with only one degree of crosslinking or no hydrogel network at all. These hydrogels, which are simply referred to as uniformly crosslinked, correspond to the given pattern of the mask and are separated from each other without having an LC interconnection and thus without forming a patch. Even though the *no patch* hydrogels are called uniformly crosslinked, there might be minor variations within the hydrogels due to the fabrication method, for example, because of providing the associated irradiation from one channel side and setting the present light focus in the middle of the channel height. These minor deviations, however, are considerably marginal compared to the induced levels of crosslinking of the patches by the mask pattern.

During *sticking*, the arising hydrogel network sticks to the channel bottom, top, or both. Hence, the hydrogel cannot be flushed out of the microfluidic channel and collected. Instead, the hydrogel blocks the channel.

The *sticking* can occur with uniformly crosslinked hydrogels or with patches and leads in both scenarios to the interruption of the continuous fabrication process. However, in applications of microfluidic chromatography, this may actually be desirable to fabricate a precisely tuned stationary phase of the chromatography bed. For both formation events, *no patch* and *sticking*, no patches can be collected for subsequent use. Hence, the first objective of the study was to identify at which conditions patches form.

Which formation event occurs depends on several influencing parameters. The hydrogel formation via free-radical photopolymerization is mainly determined by irradiation, polymerization system, mass transport by diffusion, light scattering, and oxygen diffusion. [Wolf2021] The irradiation parameters determine the initiation of the polymerization, whereas the molecular composition of the polymerization system determines the reactivity of the reaction solution. Monomer diffusion and light scattering cause the diffusion of the local reactivity resulting in less sharp polymerization domains. This apparent disadvantage was utilized to generate hydrogel patches.

Oxygen prevents radical photopolymerization, and oxygen needs to be depleted before crosslinking reactions can occur. At the channel walls of the microfluidic flow channel, a so-called oxygen inhibition layer (OIL) is present since atmospheric oxygen diffuses through the porous channel material poly(dimethylsiloxane) (PDMS). Thus, the polymerization at the channel walls is prevented to a certain extent, and the thickness of the OIL influences the height and the sticking of the hydrogels. [Dend2008; Wolf2021]

Radiant power directly correlates with the number of radicals forming [Haki2014], and the exposure time highly impacts the diffusion since this is time-dependent. As a result, hydrogels are shorter (z-axis) and thicker (xy-plane) when fabricated with decreased radiant power and increased exposure time for constant energy input. This hydrogel shape varies from the straight elongated hydrogel shape normally desired during SFL. [Wolf2021] However, to achieve three-dimensional patches, these shape variations towards shortened and thickened hydrogels are favorable since they prevent sticking by an increased distance to the channel walls and broaden the hydrogel network, particularly in its height center. Hence, a parameter combination with low radiant power and high exposure time is preferred for successful patch formation at a constant energy input.

Generally speaking, a decreased radiant energy input results in *no patch* formation, whereas an increased energy input favors *sticking*. Furthermore, for successful patch formation, precursor monomer diffusion and light scattering need to be enhanced compared to *no patch* formation, whereas the oxygen inhibition at the channel walls needs to be retained. Thus, the LC hydrogel network can form beyond the irradiated areas and connect individual HC regions without *sticking* to the channel wall. To achieve mechanically stable and removable patches, the parameters of the fabrication process need to be controlled and set within a certain interval.

Polymer Material and Irradiation Influence

The most prominent process parameters for controlling formation events are the material system, the exposure parameters, and the mask dimension. These parameters were tuned within this study to form hydrogel patches successfully and reliably. Figure 4.3 displays the formation events for two different material systems and varying exposure parameters. The first material system is based on poly(ethylene glycol) diacrylate (PEGDA), whereas the other material system contains *N*-isopropyl acrylamide (NIPAM) and *N*, *N*'-methylene bisacrylamide (BIS). A transparency mask was used that has circle-shaped spots of 40 µm diameter, which are arranged in a hexagonal arrangement with 100 µm edge-to-edge distances to all six neighboring circle shapes on the mask. The exposure time t and the radiant power P of the UV-LED directly correlate with the energy input on the irradiation area A according to

$$H = \frac{P \cdot t}{A}. \tag{4.1}$$

Three different values of this energy input per area, called radiant exposure *H*, were studied: 38, 50, and 63 mJ mm^{-2}. For each radiant exposure, the exposure time and the radiant power were varied, investigating four parameter combinations per radiant exposure, resulting in a total of 12 investigation points. The formation events, *patch*, *no patch*, or *sticking*, were recorded for both material systems.

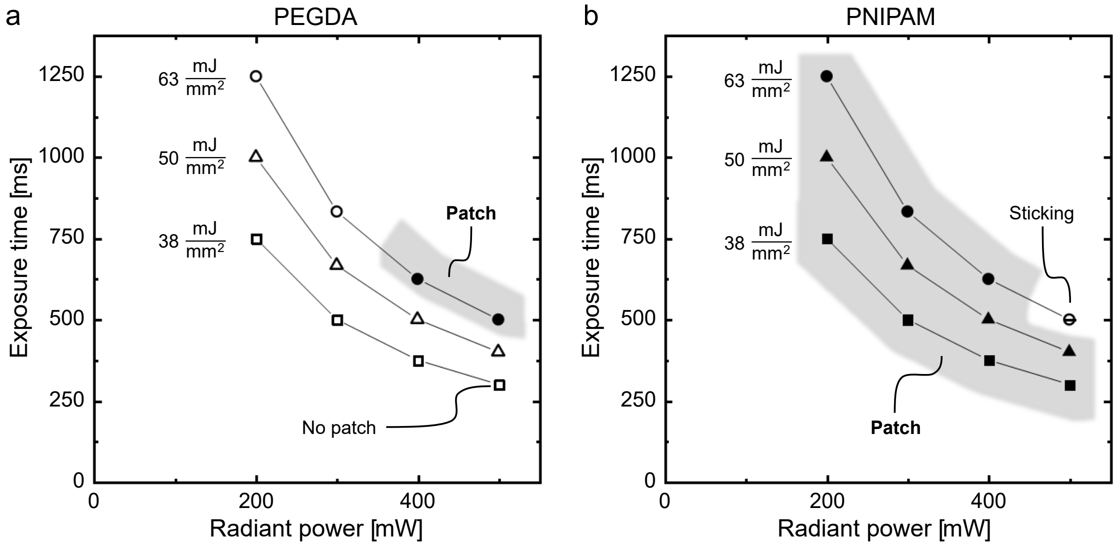

Figure 4.3: Occurrence of the formation events depending on the applied exposure parameters during fabrication, displayed for three radiant exposures with four exposure pairs each: 38 mJ mm^{-2} (square), 50 mJ mm^{-2} (triangle), and 63 mJ mm^{-2} (circle). Formation events plotted for a (a) PEGDA-based material system and (b) PNIPAM hydrogels: *no patch* (unfilled symbols), *patch* formation (filled symbols and a gray area), and *sticking* (strikethrough symbols). A transparency mask with circle-shaped spots of 40 µm diameter was used with the circles having an edge-to-edge distance of 100 µm to all six neighboring circle shapes on the mask (hexagonal arrangement).

Figure 4.3a shows the formation events occurring for the PEGDA material system, displaying exposure time over radiant power while grouping the parameter combinations displaying the same radiant exposure. *Patch* formation occurred at the highest radiant exposure of 63 mJ mm^{-2} applied for the two parameter combinations with the highest radiant powers but lowest exposure times (500 mW for 500 ms, 400 mW for 625 ms). For all other parameter combinations, *no patches* were fabricated, either forming hydrogels without LC interconnection or showing no hydrogel network at all. Hence, the HC regions could not be connected for radiant exposures below 63 mJ mm^{-2} for the PEGDA material system. Patches forming only at high radiant power and low exposure times for a constant radiant exposure firstly is counter-intuitive. For high radiant powers and low exposure times, the HC regions at the irradiation spots are theoretically thinner (xy-plane) and longer (z-axis). However, the other two combinations of parameters of the same radiant exposure with thicker (xy-plane) and shorter (z-axis) HC regions did not result in *patch* formation. Thus, the hydrogel network between the HC regions seemed not to be sufficient for a stable polymer network. A possible explanation could be the height confinement (z-axis) of this network in the center for low radiant powers and high exposure time, possibly being too thin to withstand mechanical stress.

For the NIPAM-based material system, a wider formation window was observed for the same exposure parameters, as shown in Figure 4.3b. At the highest radiant exposure of 63 mJ mm^{-2}, the parameter combination with the highest radiant power (500 mW, 500 ms) resulted in *sticking* of the resulting hydrogel network. For this parameter combination, *sticking* is comparably favored due to a higher (z-axis) hydrogel network for high radiant powers. Except for this single parameter combination, *patch* formation was achieved for all applied parameters.

The results show a significant influence of the material system on the formation of hydrogel patches. For the same weight proportion of PEGDA and NIPAM, *patch* formation is significantly more favored for the NIPAM-based material system. In this context, the total number of reactive double bonds in the reaction solution is decisive for the hydrogel and thus the *patch* formation. [Kitt2023] To calculate this number, the number of reactive groups per molecule, as well as the molecule's mass, are relevant since the reaction solutions were composed via weight proportions. Furthermore, the NIPAM-based material system not only consists of NIPAM as the monomer but also includes the crosslinker BIS, whose reactive groups must also be considered. The NIPAM-based material system, therefore, has almost three times as many reactive groups as the PEGDA-based material system. Moreover, there are further influencing factors regarding the hydrogel formation that differ between both material systems, such as rheological properties, molecular diffusion, or accessibility of reactive groups. The molecular diffusion is directly affected by the coil volume of the molecules. [Kitt2023] Since the polymer-forming molecules of the NIPAM-based material system are both significantly smaller than the PEGDA molecules, their molecular diffusion is faster. Hence, the favored patch formation of the NIPAM-based material system is reasonable due to the increased reactive groups and the faster molecular diffusion of the NIPAM-based material system. Due to the favored *patch* formation of the NIPAM-based material system for the same weight proportion of the precursor and the thermoresponsive properties of PNIPAM with arising application possibilities, the following patch characterizations are conducted with PNIPAM patches.

Mask Dimension Influence

Besides the material system and the exposure parameters, the features of the transparency mask, i.e. the geometrical details and their dimensions, highly influence whether patches are formed and further define the geometry of the patches. The geometrical features of the mask comprise the shape of the individual irradiation spots, their diameter, their distance from each other, and their lateral arrangement on the mask. Figure 4.4 shows the formation events for varying the spots' (a) distances and (b) diameters. During the variation of one of these mask parameters, the other parameter was held constant at 40 µm diameter or 100 µm distance, respectively. All masks have circle-shaped irradiation spots in a hexagonal arrangement, which is exemplified in Figure 4.2 (and Figure 4.5a). Each spot has six directly neighboring spots, separated by the same distance. During fabrication, the mask pattern is projected into the microfluidic channel, reducing its dimensions by a constant factor of 5.46 as a result of the projection lithography setup. [Wolf2020] Therefore, the resulting patches fabricated with a mask with a spot diameter of 40 µm exhibit HC regions with diameters of around 7 µm. To investigate the influence of the mask on the patch formation, the formation events for varying mask dimensions were investigated for PNIPAM hydrogels at constant radiant exposure (38 mJ mm^{-2}) and changing radiant power and corresponding exposure time, equal to the parameter combinations investigated before (compare Figure 4.3).

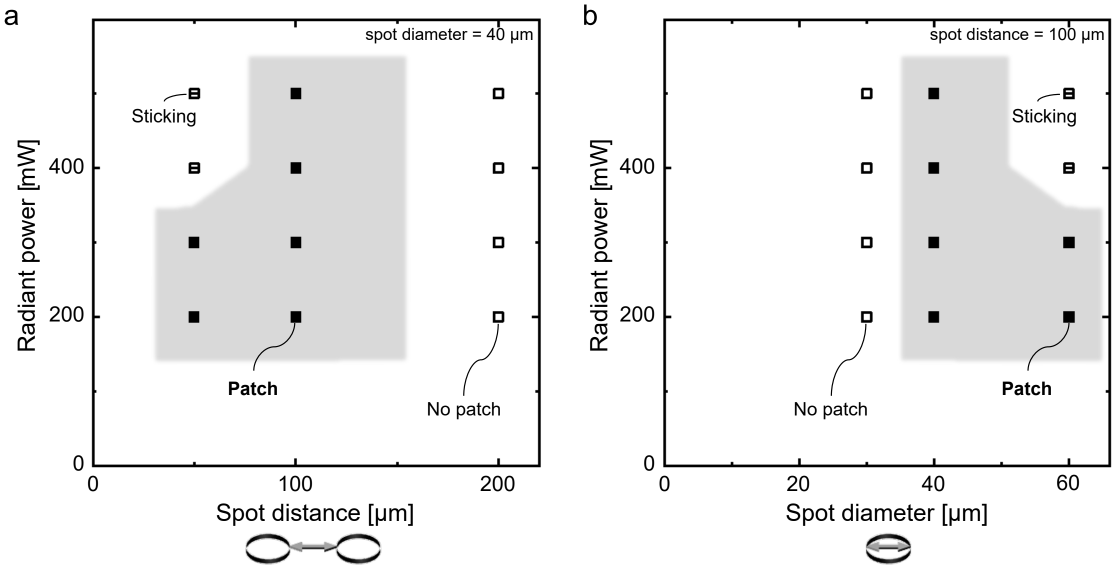

Figure 4.4: Influence of the dimensions of a transparency mask with a hexagonal arrangement of circle-shaped spots on the hydrogel formation events: *no patch* (unfilled symbols), *patch* formation (filled symbols and a gray area), and *sticking* (strikethrough symbols). PNIPAM hydrogels fabricated at a constant radiant exposure (38 mJ mm^{-2}), investigated for (a) a varying spot distance at a constant spot diameter of 40 µm and (b) a varying spot diameter at a constant spot distance of 100 µm for four exposure combinations each.

If the diameter of the irradiation spots on the transparency mask was held constant to 40 µm, an ideal spot distance of 100 µm was observed (compare Figure 4.4a). For this spot distance, each applied parameter combination results in *patch* formation. For a halved spot distance of 50 µm, in only two of the four irradiation cases, patches were formed. A decreased spot distance enhances *sticking* of the hydrogels due to the mask pattern-dependent increased local energy input and the decreased diffusion and scattering distances, resulting in lower oxygen inhibition. Furthermore, high radiant power at constant radiant exposure favors *sticking* as a result of increased oxygen depletion at the channel walls. The local energy input can be described by the proportion of the actual irradiated area, relative to the possible overall irradiation area. This value equals the proportion of HC regions in relation to the patch area. The mask with a decreased edge-to-edge spot distance of 50 µm leads to a proportion of 18 % of the actual irradiated area. In comparison, the reference mask with 100 µm spot distance and the same spot diameter has an actual irradiation contribution of 7 % (compare Table 5 in the Appendix). For a doubled spot distance of 200 µm, *no patch* formation occurs for all parameter combinations. Here, the same effects cause this formation event, which work as the opposite by decreasing the local energy input (3 % actual irradiated area) and increasing the diffusion and scattering distances with increasing spot distance.

Not only does a decreasing spot distance increase the local energy input per area, but an increasing spot diameter for a constant spot distance has the same effect. Figure 4.4b shows the formation events for a varying spot diameter and the four defined parameter combinations at 38 mJ mm^{-2} radiant exposure each. If the spot diameter is increased only by 50 % to 60 µm, *sticking* occurs for the two parameter combinations with the highest radiant powers (400 mW, 500 mW). Here, the actual irradiated area accounts for 13 % of the possible overall irradiation area compared to 7 % of the reference mask with 40 µm diameter (compare Table 5 in the Appendix). However, in contrast to the varying spot distances, the diffusion and scattering distances between the irradiation spots stay the same for varying spot diameters due to a constant edge-to-edge distance. Hence, the differences in formation events are only caused by the deviating local energy inputs due to adapted actual irradiation areas. In contrast, *no patch* appears for a spot diameter of 30 µm for all combinations of exposure parameters tested. For this mask, a decreased actual area of 5 % is irradiated, resulting in an insufficient local energy input for *patch* formation.

Investigating the influence of the dimensions of the transparency mask enables reliable hydrogel patch fabrication. As a reference point, the spot diameter-to-distance ratio should be about 0.4 to definitely achieve *patches* during fabrication. A lower ratio results in *no patch* formation and a significantly higher ratio in *sticking*. Based on this ratio, the geometry of the mask can be varied, revealing straightforward patch formation, as discussed in the following section. Even when there is an optimal ratio of mask dimensions to form patches, these dimensions can be adjusted to a certain extent. This flexibility can be further enhanced by additionally adapting the fabrication parameters. Thus, the extent of the LC network and the ratio between the LC and HC networks are tunable. This, in fact, allows the design of the patch dimensions to be on purpose and tailored to applications, such as a cell-specific space for growing. To allow comparability between the patches characterized in this work, all the following PNIPAM patches were fabricated at the same exposure parameter settings (38 mJ mm^{-2}, 200 mW, 750 ms).

4.3.2 Geometry Variation

With the spot diameter-to-distance ratio of about 0.4, it is straightforward to design new patch geometries. On the one hand, the HC spots can be significantly enlarged, as exemplarily shown in Figure 4.5a for a patch with enlarged circles. This patch compromises 52 µm large circles in contrast to the diameter of the circles of the previously investigated patches of 7 µm. The enlargement was directly realized by increasing the diameter and distance of the spots while retaining the approximate diameter-to-distance ratio. On the other hand, the shape of the irradiated spots and, thus, the shape of the HC regions can be tailored as well. Figure 4.5a shows four different masks and their resulting patches with adapted spot shapes. For all masks, the spots' surface area, their distance from center to center, and their hexagonal arrangement are identical.

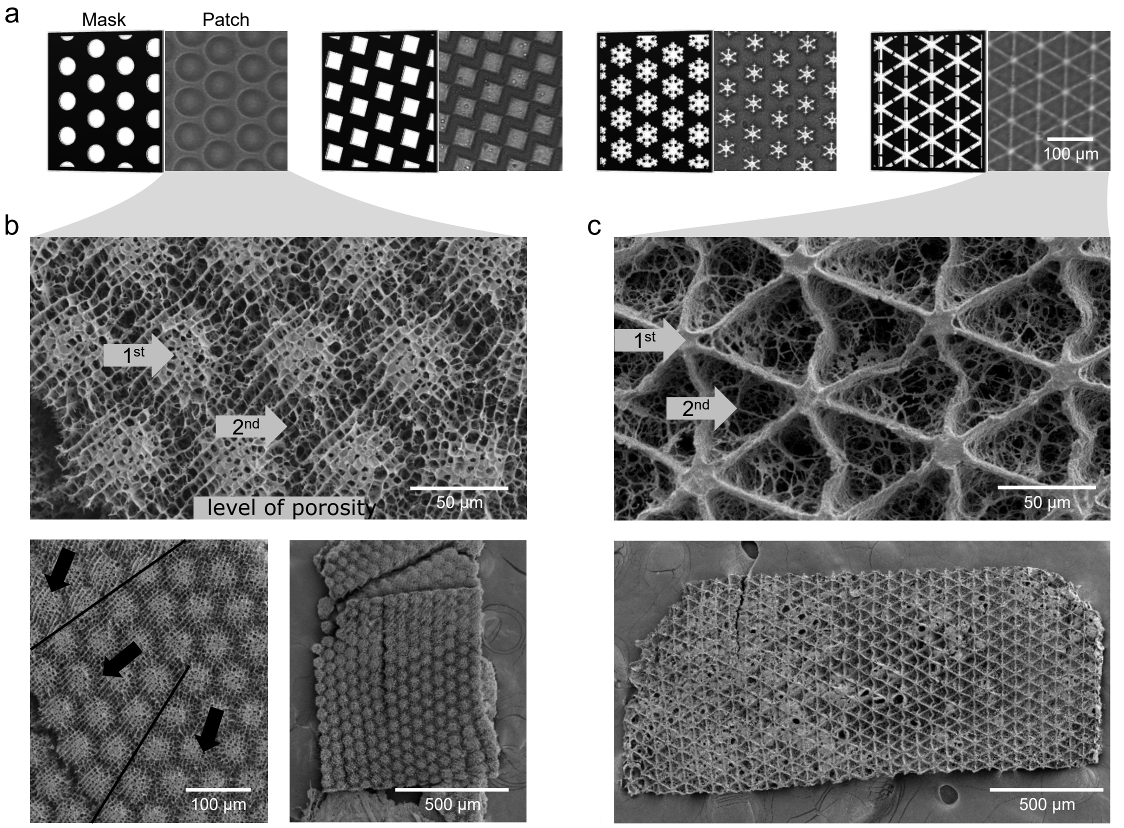

Figure 4.5: Varying patch geometries by different spot shapes. (a) Mask schemes and corresponding brightfield images of patches with different shapes of the HC regions induced by the irradiated mask spots. From left: circle-shaped, square-shaped, snowflake-shaped, star-shaped. All other mask parameters are held constant for all patch types: irradiation spot area, center-to-center spot distance, and hexagonal spot arrangement. Scale bar (100 µm) applies to all micrographs. (b-c) FESEM images of patches with (b) circle-shaped or (c) star-shaped irradiation spots. (b) Black lines and arrows indicate regions with different directionalities within the porous structure of the patch, most likely resulting from freeze-drying.

Optical analysis via FESEM revealed the porous structure of the different hydrogel patches. Figure 4.5b and c show the porous structures of patches with a circle-shaped and a star-shaped geometry, respectively. Less and more porous regions are present within the patches, corresponding to the patch-specific HC and LC regions observed before. The HC regions induced by the spots of the mask are comparatively denser than the interconnecting LC regions. Thus, the irradiation spot location is confirmed to be directly related to a higher degree of crosslinking, as stated before, expressed by a lower porosity in electron microscope images. These two regions within the patches represent two levels of porosity that can be intentionally designed with the fabrication method presented here. The first level refers to the spot-induced HC regions, while the second level of porosity evolves from the bridging of the polymer network between these spots.

The apparent directionality within the porous structure of the circle-shaped patch (compare Figure 4.5b) is most likely related to the preparation method of the patch sample and, therefore, not to the structural features of the patch itself. The chosen drying method during sample preparation highly affects the appearance of hydrogel structures in FESEM investigations. [Lin1999] Freeze-drying used here applies a force on the samples and is known to introduce pores within soft porous structures, and the direction of ice crystal growth during freeze-drying mostly likely induced the directionality within the patch. [Lin1999; Foud2023] A cause related to the fabrication is unlikely since a possible flow- or light-induced cause would result in a unidirectional impact on the patch structure, whereas the apparent directionality changes within the patch, indicated by the black lines and arrows in the middle magnification of Figure 4.5b.

The height (z-axis) of the hydrogel differs between regions with low and high crosslinking or porosity. This height difference is particularly visible for the FESEM image of the star-shaped patch (compare Figure 4.5c). The HC regions appear particularly dense and possess the approximate height of the channel in which the patches were fabricated. In contrast, the LC regions between exhibit µm-sized pores after freeze-drying and seem like triangle-shaped cavities due to their comparatively low height compared to the HC regions. This height difference between the regions is caused by the LC regions receiving less energy during formation.

In the photo-induced radical polymerization of the patches using projection lithography, the highest energy is concentrated at the focal plane of the light in the center (x-axis) of the microfluidic channel. At this level, the radiant exposure is maximized due to the light focus, and the oxygen inhibition is minimized due to the greatest distance from the channel walls. [Dend2008] Consequently, the formation of LC regions between the irradiation spots starts at the z-axis centered height of the channel surrounding the irradiation spots (in the xy-plane). As the distance to the channel walls decreases, oxygen inhibition increases, necessitating high local energy at the top and bottom of the channel for polymerization, which the LC regions lack. Thus, both crosslinked regions, HC and LC, develop in the central height of the formed patches, though only the HC regions span the full channel height, extending in both directions along the z-axis.

4.3.3 Porosity Variation

In addition to the two induced and always occurring degrees of crosslinking of the patches, further degrees can be induced, being equivalent to levels of porosity. Figure 4.6 shows two exemplarily patches with three engineered levels of porosity (*44 µm pore* and *95 µm pore*), based on mask designs having larger domains without light transmission. This third level of porosity is introduced by varying the distance between some irradiation spots within the patch while maintaining the hexagonal spot arrangement with optimal diameter-to-distance ratio at other regions within the mask. Thus, the formation of coherent patches is ensured by retaining the basic framework of spots that was designed for reliable patch formation in Section 4.3.1.

The three exemplary patch structures in Figure 4.6 have the same first two degrees of crosslinking with HC and LC regions, resulting in two porosity levels. All three patches have circle-shaped HC regions with 7 µm diameter and 18 µm edge-to-edge distance to each other as the first level of porosity. In between, LC regions are present, possessing the second level of porosity. By omitting single irradiation spots within the mask, the second patch has regions with an even lower crosslinked network and, thus, a third level of porosity, which is highlighted in the FESEM images in Figure 4.6b *44 µm pore*. These regions cover a diameter of 44 µm and consist of a polymeric network, which is visible during brightfield imaging but cannot be

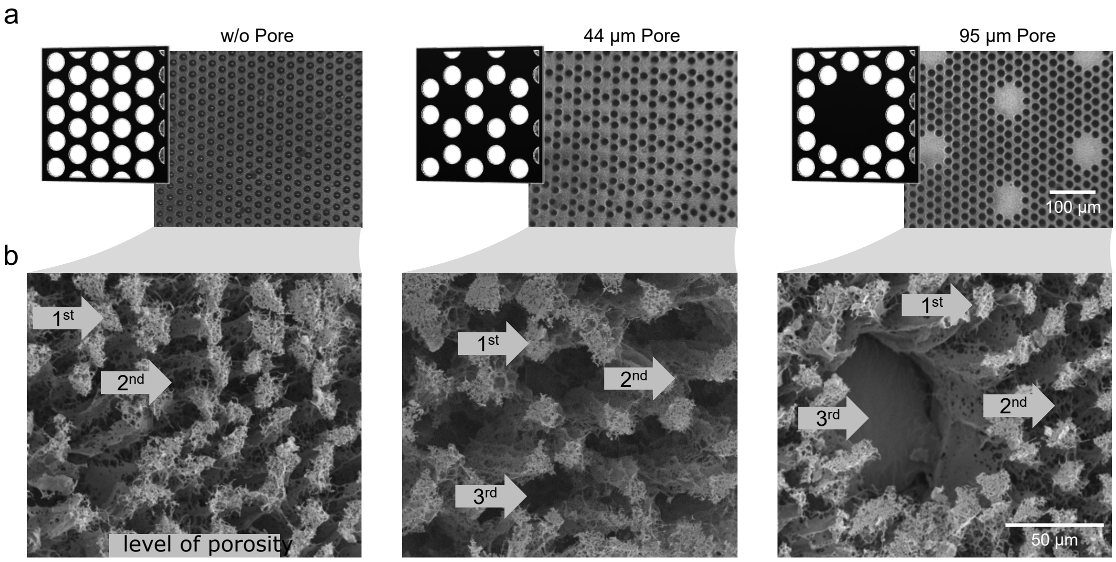

Figure 4.6: Patches series with induced third level of porosity by missing out irradiation spots within a regular hexagonal spot arrangement of circle-shaped spots with 7 µm diameter on the patches. From left to right: without additional induced porosity (*w/o pore)*, induced 44 µm porous regions by single missing irradiation spots (*44 µm pore*), induced 95 µm pores by missing an arrangement of seven spots (*95 µm pore*). Visualization of the patches by (a) mask schemes and corresponding brightfield images of the patches and (b) FESEM images with levels of porosity being indicated. Scale bars (a: 100 µm, b: 50 µm) apply to all micrographs each.

reliably detected in the FESEM images, which is most probably attributable to the preparation method for FESEM via freeze-drying. Within the mask used to fabricate the third patch (Figure 4.6 *95 µm pore*), not only single spots but entire spot arrangements of seven spots are omitted. Hence, porous regions with a diameter of 95 µm emerge within the resulting patch. Since this distance between the irradiation spots is too large to be bridged by the forming polymer network during the fabrication, these porous regions actually are single pores, respectively, through-pores within this patch type. By omitting different irradiation spots within the mask pattern, a customizable third-level porosity is induced into the patch pattern.

The presented patch examples demonstrate the design freedom allowing to potentially adjust the patch properties beyond the previously described combinations of HC and LC regions. Consequently, other regions within the patch pattern can be adapted, enabling a high degree of freedom and multiple levels of porosity even beyond the three shown. The variable spot shape and the intended dark spots of the irradiation pattern of the transparency mask increase the complexity of the geometry and also allow the design of laterally inhomogeneous porosity patterns. Such designed patch patterns may, for instance, provide tissue scaffold structures, which enable a directionality and cell growth guidance structure, or tune the mechanical properties of the patch at desire. Introduced through-pores can further serve, for example, as migration channels of cells for applications of the patches in cell culture. They also allow the stacking of patches while having connection channels and, thus, provide thicker scaffold structures.

4.3.4 Designed Mechanical Characteristics

The crosslinking degree and the patterns and combinations of the levels of porosity of a patch can influence its mechanical characteristics. Due to the pattern of HC and LC regions, local mechanical differences occur within the patch laterally. The overall mechanical characteristic of each patch type, meanwhile, results from an interplay of these regions, which is determined by the geometrical pattern of the masks. To illustrate this feature of the patches, selected patches, which are shown in Figure 4.7, are investigated regarding their mechanical characteristics. The patches

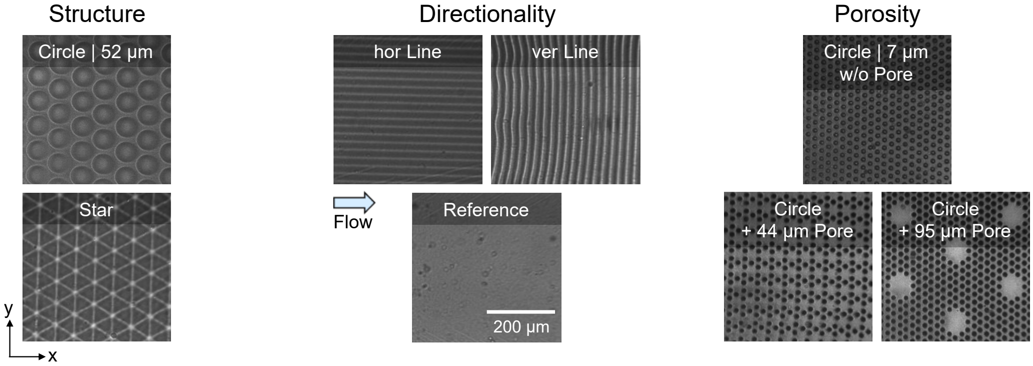

Figure 4.7: Selected patches for the investigation of their mechanical characteristics, grouped according to geometrical variations: structure, directionality, and porosity. Scale bar (200 µm) applies to all micrographs.

are classified according to their geometry and the associated influence on their mechanical properties (compare Table 5 in the Appendix for geometric parameters of the patches). By comparing these patches according to their classifications, the influence of the individual aspects of the patches' patterns on their mechanical characteristics is investigated.

Compression

The mechanical characteristics of the patches were determined by performing lateral compression experiments inside a microfluidic channel, which has the yz-dimensions of the patches and is schematically displayed in Figure 4.8a. The microfluidic channel used for the compression experiments has a filter structure at the end of the channel, which restricts the patches and lets the surrounding water permeate. Hence, the patches were pressed against the filter, as shown in Figure 4.8a for the *circle* patch. Micrographs of the uncompressed, the maximal compressed, and the end state of each patch type are displayed in Figures 2, 3, and 4 in the Appendix. For the quantitative investigation of the patches' compression ability, the area visible in the top view was measured as a function of the applied pressure. Since a linear pressure ramp was applied, the pressure change is proportional to time. The change of the normalized area over applied pressure is visualized in Figure 4.8b, showing the averaged curve progression of the eight selected patch types. Monitoring the patches' surface area during compression reveals the compression ability of the patches depending on their geometrical pattern.

The analysis of the compression curves allows to categorize the behavior of patches into three distinct compression regimes: linear, plateau, and reverse compression. According to the linear regime, the area of the patch decreases linearly with increasing pressure, like the curve of the *w/o pore* patch. During the plateau regime, the patch area linearly decreases to a certain minimum surface area before staying constant, similar to the curve

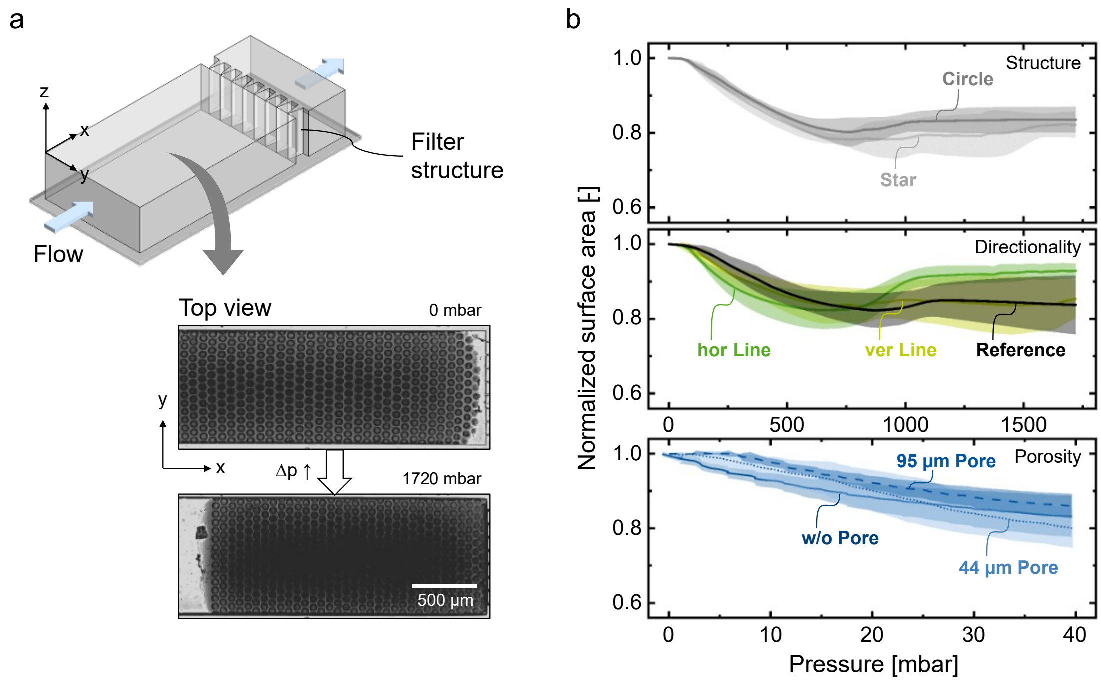

Figure 4.8: Lateral compression of selected patches. (a) Schematic microfluidic channel geometry and experimental compression process, exemplarily shown for a patch with circle-shaped HC regions with 52 µm diameter in a hexagonal arrangement (circle | 52 µm). Scale bar (500 µm) applies to all micrographs. (b) Compression behavior of the patches is displayed by the change in their surface area over increasing applied pressure, grouped according to geometrical variations: structure, directionality, and porosity.

of the *circle* patch. The reverse compression regime is characterized by an initial strong decrease in patch area over applied pressure followed by a reversal, as visible for the curve of the *hor line* patch. This unexpected behavior is attributed to changes in force distribution caused by the patch blocking the filter structure of the microfluidic channel. Since the HC regions are denser than the LC regions, they block the microfluidic channel to a greater extent. Thus, patches with a great proportion of HC regions preferably exhibit this compression behavior. The three distinct compression regimes classify the patches' compression behavior, and the specific regime observed is influenced by various porosity features of the patches' geometrical patterns. The method and results described above require a detailed simulation study to correlate porosity features with quantitative mechanical behavior. However, this is beyond the scope of this contribution.

The structure of HC regions of the patches significantly affects their compression behavior. *Star* patches all compress according to the reverse compression regime, whereas only some *circle* patches show a reverse compression and the others a plateau compression (compare Figure 5 in the Appendix). On average, the *star* patch type compresses more than the *circle* patch type despite having the same proportion of HC and LC regions. This difference is likely due to the thinner HC regions in *star* patches. Additionally, *star* patches show greater variability in compression, highlighting the role of structural geometry in mechanical performance. Hence, the structure of the HC regions of the patches influences the regime, the maximum degree, and the consistency of the patches' compression.

Directionality within the patch pattern is a critical determinant of mechanical response. The *hor line* and *ver line* patch types possess horizontal or vertical HC lines when viewed from the top (compare Figure 4.7), and thus, their lines are in flow or perpendicular to the compressive flow, respectively. These *line* patches exhibit distinctly different compression behaviors despite having the same pattern rotated by 90°. *Hor line* patches with HC lines in flow demonstrate consistent and substantial reverse compression, while *ver line* patches with perpendicular lines display more variability and divergent compression regimes for individual patches (compare Figure 6 in the Appendix). This suggests that directional alignment influences force distribution, making it an important consideration in material design.

Porosity only slightly affects the patches' compression behavior, though it does not alter the compression regime. Patches with different porosity levels compress similarly according to a linear regime. This uniformity is attributed to the consistent underlying patch pattern, indicating that porosity affects the flexibility and the local deformation capacity but not the fundamental compression response. Compared to the other patch types, the *porosity* patches were compressed at a significantly smaller pressure range since they started to intrude the 5 µm large pores of the filter beyond 40 mbar and thereby rupture at their LC regions. This squeezing and rupture behavior is indicative of a distinctly different mechanical behavior compared to the other patch types. However, their compression extent compares well with the other patches.

Squeezing

The direction of the applied force matters in determining the local mechanical characteristic of a patch, which highly depends on the patch geometry. A new chip design allowed for so-called squeezing experiments (compare Figure 4.9a). These allow to investigate the local compression of the patches in the y-direction in addition to the longitudinal and overall compression in the x-direction investigated via compression experiments. These mechanical characteristics are relevant for potential future applications, such as insertion of patches into a confined space. During squeezing experiments, the patches were squeezed through a 225 µm wide constriction of a microfluidic channel having the same width (y-direction) and height (z-direction) dimensions as the patches. Due to the height restriction, the patches could not buckle but remained in their 2D geometry. Figure 4.9a displays the squeezing of a *circle* patch. The width of the constriction corresponds to a quarter of the channel and patch width, resulting in a compression of the patches inside the constriction by 75 %. The patches need to compress locally to surpass the constriction since the dimensions of the microfluidic channel hinder any third-dimensional buckling or folding.

To quantify the squeezing potential of the different types of patches, the pressure at which the patches break through the constriction was detected, as displayed in Figure 4.9b. Furthermore, the half-through state is also depicted, which can be seen in Figure 4.9a at 1690 mbar for the shown *circle* patch. This state means the point where half of the surface area of the patch passes the constriction. Micrographs of the intrusion, the half-through, and the breakthrough state of each patch type are displayed in Figures 7, 8, and 9 in the Appendix. Depicting the breakthrough pressures of the patches while squeezing through a constriction allows to compare the patches' local compression ability depending on their geometrical pattern.

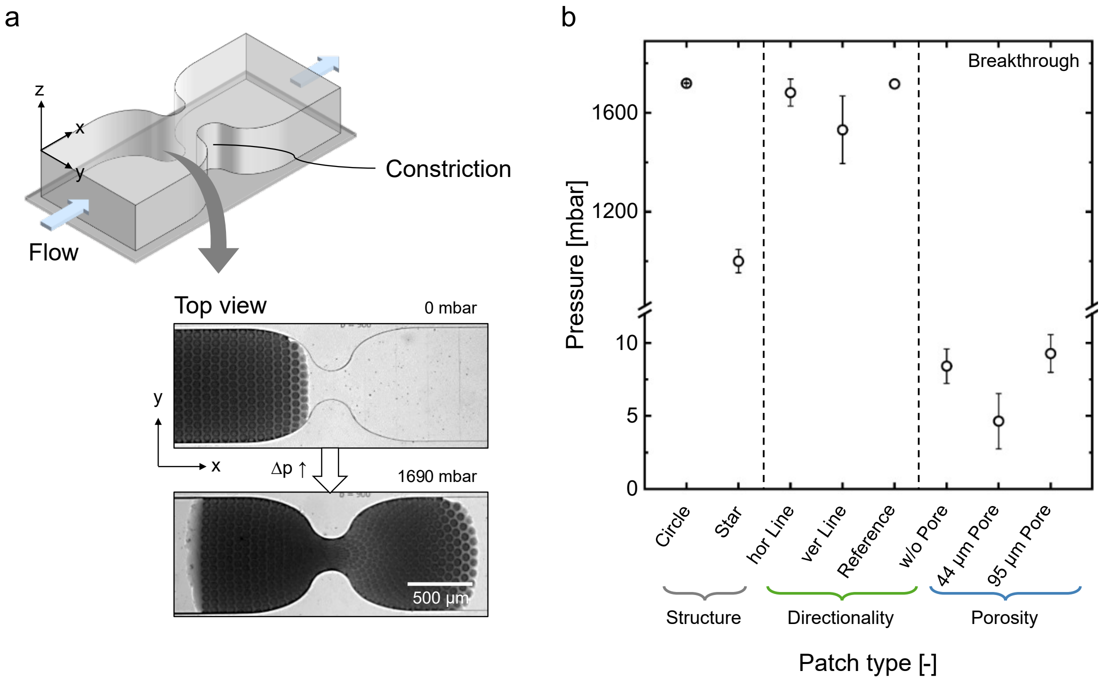

Figure 4.9: Squeezing of selected patches. (a) Schematic microfluidic channel geometry and experimental squeezing process, exemplarily shown for a patch with circle-shaped HC regions with 52 µm diameter in a hexagonal arrangement (circle | 52 µm). Scale bar (500 µm) applies to all micrographs. (b) Squeezing behavior of the patches is characterized by the pressure needed for the patches to break through the channel constriction and grouped according to geometrical variations: structure, directionality, and porosity.

The results show significant differences in breakthrough pressure between the patches of the *structure* group that have the same proportion of HC regions but different structural designs. The *star* patch type, with its thinner and more distinct HC regions, requires significantly less pressure to pass through the constriction compared to the *circle* patch type. This suggests that the structure of the HC regions, rather than just their proportion, is crucial for determining a patch's flexibility and ability to squeeze through tight spaces.

The *directionality* patch group shows how pattern directionality impacts squeezing behavior. The *ver line* patch type breaks through the constriction at a lower pressure than the *hor line* and the *reference* patches. Despite having identical patterns only differing in their directionality, the *ver line* and *hor line* patches differ in their breakthrough pressures, underscoring the significance of directionality within the patch pattern. The *reference* patch, composed entirely of HC regions, shows the highest resistance to breakthrough, often rupturing or getting stuck (compare Figure 8 in the Appendix), proposing the proportion of the HC regions to determine the squeezing ability. Notably, the *star* patch type of the *structure* group, with a higher HC proportion (49 %) than the *line* patches (29 %), still required less pressure to pass through the constriction. Hence, in addition to the directionality and the HC region proportion, the structure and arrangement of HC regions are key factors in determining a patch's mechanical response.

The degree of third-level porosity only slightly influences the patches' squeezing, but the pattern of the *porosity* group patches significantly impacts the squeezing compared to the other patches. In the *porosity* patch group, patches break through the constriction at much lower pressures (5-9 mbar) compared to the *structure* and *directionality* groups, which required at least 1000 mbar. This difference is due to the small size and low proportion (7 % or less) of HC regions of the *porosity* patches (compare Table 5 in the Appendix), making these patches highly flexible with large, interconnected LC regions. This becomes very apparent considering the patch *w/o pore* without pores. At this low proportion of HC regions, the LC regions dominate the easy breakthrough, even if no third-level porosity exists.

Among the *porosity* patches, the *44 µm pore* patch type has a lower HC proportion (4 %) than the two others and breaks through at a lower pressure, indicating that increased LC regions and greater distance between HC regions enhance flexibility. Interestingly, the presence of through-pores in the *95 µm pore* patch does not significantly affect its squeezing behavior, suggesting that the overall framework and HC region arrangement are more important than through-pores in determining flexibility and squeezing.

Figure 4.10 shows the translocation of the *porosity* patches through the constriction and reveals particular features of the process of squeezing through. The through-pores slowly deform towards the constriction, becoming highly elliptical up to disappearing visually in the constriction and relaxing back into a close to circular shape when expanding into their new state. Whether or not the patches undergo plastic deformation in general or locally to different degrees cannot be identified from the current experiments.

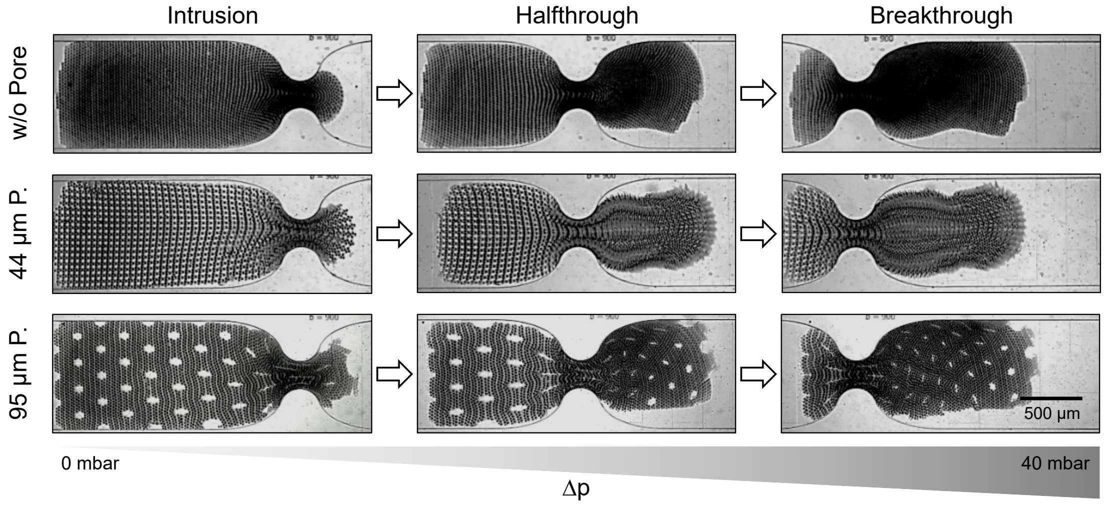

Figure 4.10: Brightfield images showing the squeezing states of the *porosity* patch types *w/o pore*, *44 µm pore*, and *95 µm pore*. Scale bar (500 µm) applies to all images. The shape of the through-pores indicates local deformation states during the translocation through the constriction.

Summary

In conclusion, the geometrical patterns of the patches determine their mechanical characteristics. As compression is favored at the LC regions within the patches, large and interconnected HC regions in a high proportion are expedient in increasing the mechanical stability of a patch. However, the proportion of HC regions shares its influence on the compression and squeezing ability with the HC structure and directionality. The induced third-level porosity only slightly changes the compression of the patches, and the squeezing was also not significantly influenced by the through-pores within the *95 µm pore* patch. But, an induced third-level porosity by changing the distance respectively arrangement of the HC regions leads to a slightly enhanced squeezing of the *44 µm pore* patch. Hence, the proportion, structure, and directionality of the HC regions mainly influence the patches' mechanical characteristics regarding compression and squeezing, whereas the investigated third-level porosity has less impact.

The high degree of freedom during hydrogel patch fabrication allows tuning of the mechanical requirements of the patches by adapting their geometrical patterns. The investigations of this section represent a foundation for predicting the mechanical characteristics of patches based on their geometrical pattern design. Shaping these patterns enables for varying mechanical requirements, such as adaptability to compression, mechanical anisotropy within patches, or varied flexibility. Using this novel fabrication procedure and combining the varying tuning factors presented in this work achieves a tailored, hierarchically structured hydrogel patch comprising cellular and gradient structural elements as desired for a targeted purpose. To engineer the mechanical properties of patches in the future based on bio-inspired designs, simulation-based hierarchical prototypes can serve as templates. [Nale2015; Ghim2024]

4.3.5 Cell Culture Scaffold with Tunable Morphology

Tissue engineering on scaffolds demands control over the mechanical properties and topography, [Liu2024; Bril2023; Solb2023] which can even, in some cases, determine cell fate. [Unad2011] Owing to the patches' remarkable tunability in both form and mechanical attributes, they are well-suited for application as cell scaffolds. To create a hydrogel scaffold suitable for cell culture, markers for cell adhesion have to be introduced to previously untreated hydrogels. Hydrogels created from synthetic polymers, such as PEGDA and PNIPAM, lack these binding sequences. In the case of PEGDA, glycidyl methacrylate (GMA) was used as a comonomer during fabrication and, thus, incorporated into the PEGDA-based hydrogel patches to present epoxy groups throughout the hydrogel and on its surface. These epoxy groups are used to enable epoxy-amine addition reactions with primary amines and, hence, to covalently bind to polypeptides such as fibronectin. [Romm2022; Kitt2023] In contrast, the PNIPAM patches were post-functionalized with fibronectin using sulfosuccinimidyl 6-(4'-azido-2'-nitrophenylamino) hexanoate (sulfo-SANPAH) as a bifunctional crosslinker. [Chan2019] With the functionalized patches, a concise cell study was performed as a proof-of-concept to investigate the reaction of cells to different topographies of the patches and their general suitability as structurally unique scaffolds.

Figure 4.11 illustrates the appearance of isolated L929 mouse fibroblast cells on specially designed patches made from PEGDA and PNIPAM materials, along with their corresponding cell areas and the patches' effective Young's moduli. The cell morphology and area vary depending on the pattern of the patches. In both material systems, PEGDA with GMA and NIPAM with BIS, the patch structure influences the cell area, as shown in Figure 4.11c. This effect was analyzed across different patch patterns, including hexagonally arranged circular HC regions with diameters of 7 µm (*circle 7 µm*) and 52 µm (*circle 52 µm*), structureless patches (*reference*), and a control without a patch (*no patch*).

Cell areas were calculated from microscopy images, depicted in Figure 4.11a for PEGDA patches and Figure 4.11b for PNIPAM patches. Cultivation was halted after two days to assess the morphology and area of isolated cells. Prolonged cultivation led to full overgrowth of the patches, causing cells to merge and lose their distinct morphologies.

In these images, after two days of cultivation, differences in cell areas and morphologies are evident. On the *circle 7 µm* patch, featuring the smallest HC regions, cells appeared more elongated and smaller in both material systems compared to other samples with different structures. This morphological difference results in the smallest cell area for this sample (see

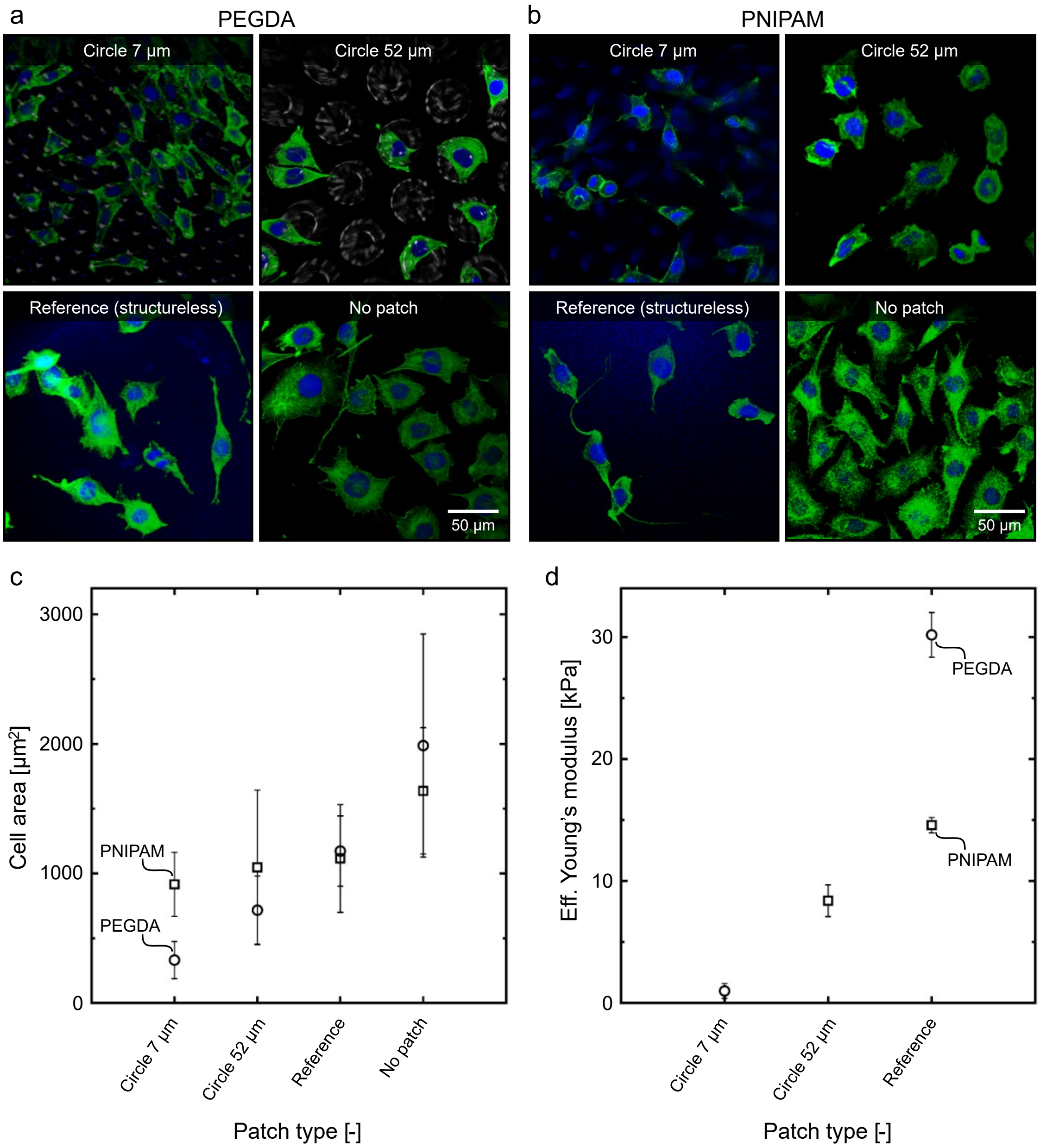

Figure 4.11: Cell cultivation (L929 mouse fibroblasts) on patches with varying structures and two different materials: (a) PEGDA patches and (b) PNIPAM patches with fibronectin coating. Patch patterns include circle-shaped HC areas with diameters of 7 µm (*Circle 7 µm*), with 52 µm diameters (*Circle 52 µm*), and structureless (*Reference*) patches. Comparison of (a-b) visual cell appearance after two days of cultivation, (c) cell area of isolated cells after this time, and (d) Young's modulus of the patches. Scale bar (50 µm) applies to all micrographs.

Figure 4.11c). Conversely, cells grown directly on the treated well bottom (*no patch*) exhibited the largest cell areas. Variations in cell area between patches likely correspond to the patch pattern, with smaller structures leading to smaller cell areas. This correlation is more pronounced for PEGDA patches, displaying a clear trend. Structured patches guide cell morphology and area, while structureless patches offer a flat surface for cell spreading.

The effects of patch pattern structure on cell properties are intricately linked with differences in material functionalization and variations in Young's modulus, making it challenging to fully disentangle their individual contributions. Notably, when comparing cell areas under both structure control conditions (compare Figure 4.11c *no patch*), the subtle differences indicate the impact of functionalization. Specifically, the *no patch* condition shows a slightly larger cell area for the functionalization used in PEGDA patches compared to the sulfo-SANPAH functionalization employed for PNIPAM patches. However, this difference is within the margin of error.

As depicted in Figure 4.11d, the effective Young's modulus appears to increase in tandem with cell area as the size of the HC regions within the patch structures increases, spanning a range of 1 to 30 kPa, which is suitable for various cell types. [Butc2009] In addition to topographical cues, cells exhibit high sensitivity to the stiffness of scaffold materials, a factor that may confound the effects of structure on cell area. [Janm2020] However, the findings from the *reference* patches suggest that Young's modulus alone cannot fully account for the observed differences in cell area. Despite significant differences in Young's modulus between the structureless PEGDA and PNIPAM *reference* patches, the resulting cell areas are almost identical (see Figure 4.11c). This indicates that while the stiffness of the patches may influence cell growth, topographical features appear to play a more pivotal role in determining cell area.

These observations underscore the need for further investigations to isolate the effects of patch topography from other influencing factors, providing a deeper understanding of the interplay between scaffold design and cell behavior. In conclusion, while functionalization and Young's modulus contribute to cell-related parameters, the pattern of the patch structure emerges as the dominant factor within the scope of this study.

After four days of cultivation, cells proliferate extensively, covering nearly the entire patch surface and aligning according to the underlying patch pattern. As depicted in Figure 4.12, cell growth is illustrated on a *circle 95 µm pore* patch (compare Figure 4.6). This patch features hexagonally arranged circular HC regions with diameters of 7 µm and edge-to-edge distances of 40 µm. The patch also incorporates through-pores with diameters of 95 µm, arranged in a hexagonal pattern with inter-pore distances of 164 µm.

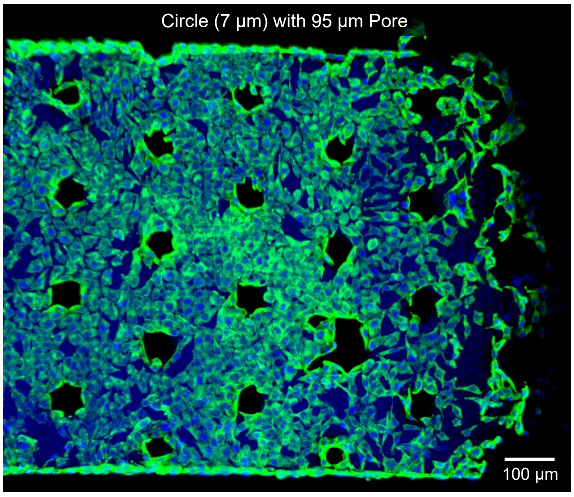

Figure 4.12: Cell cultivation (L929 mouse fibroblasts) on a *circle 95 µm pore* patch with HC regions of 7 µm diameter in a hexagonal arrangement, regularly interrupted by through-holes with 95 µm diameter. The patch material is based on the PEGDA-material system with the addition of GMA to enable fibronectin coating.

Cells exhibit a highly organized arrangement around the through-pores, effectively covering the entire patch surface area between them. These through-pores may serve as channels for cell migration in stacked configurations of multiple patches, potentially enabling three-dimensional tissue assembly with precisely tunable topography in future tissue engineering applications. Consequently, the hierarchical structuring of these patches offers a promising strategy for guiding and constraining cell propagation, facilitating the cultivation of tissue with predefined architecture and shape.

4.4 Conclusion and Outlook

This work introduces the design, characterization, and potential applications of hierarchically structured and tunable hydrogels, called patches. These patches are hierarchical cellular materials fabricated in high throughput using projection lithography in stop-flow mode. The patches are 80 µm in height and 2.25 x 0.9 mm in size, with intricate micrometer-sized features. These features consist of highly crosslinked (HC) regions, which are patterned by the transparency mask during fabrication and, as a result, are adjustable in size, shape, and crosslinking degree. These HC regions are connected by low crosslinked (LC) regions, whereas the HC/ LC geometry, the material properties, the porosity, the mechanical properties, and the functionalization of the patches can be customized.

This study on hydrogel patches identifies key parameters that influence patch formation, including radiant exposure, radiant power, and exposure time during polymerization for two material systems based on PEGDA and PNIPAM. An optimal diameter-to-distance ratio of HC regions of about 0.4 is found for reliable patch formation, emphasizing the importance of geometrical patterns. By altering the mask design, the porosity and mechanical characteristics of the patches can be further fine-tuned, enabling the formation of extra regions with through-pores embedded into the patch, featuring accurately crafted topologies of spatially varied crosslinking densities. The proportion and connectivity of the HC regions determine the patches' mechanical characteristics, along with their structure and directionality. These investigations serve as a benchmark to design patches with desired characteristics.

The potential application of the patches as cell scaffolds is explored, demonstrating their suitability for tissue engineering and cell behavior studies. The customizable nature of the patches makes them ideal for observing cellular responses in different environments. Beyond cellular applications, these patches have potential uses in non-cellular fields, such as separation processes and water absorption.

5 Conclusion and Future Perspectives

This thesis analyzes the characteristics of microgels and how to tailor them, focusing on their porous structure, thermal response, magnetic motion, and designed architecture. These particular characteristics were altered for complex-shaped microgels by adjusting their fabrication via stop-flow lithography (SFL), providing anisometric microgels in high resolution, high throughput, and comparably low cost. The presented investigations showcase high customizability, precise tuning, and future prediction of the microgels' characteristics.

Porous Structure and Thermal Response The porous structure of rod-shaped microgels was adjusted by inducing the cononsolvency effect during their fabrication based on free-radical photopolymerization. The presence of a water-methanol mixture as the solvent in the reaction solution leads to altered polymer interactions, resulting in a thinner polymeric network of the microgels with a finer structure and elongated pores. The applied cononsolvency effect additionally changes the appearance of the microgels, increasing their aspect ratio for increased methanol content. Thereby, the microgel length increases in the swollen state, whereas it decreases in the collapsed state, leading to a significantly enhanced collapsing degree for microgels fabricated with a methanol content of 30-50 wt%. The collapsing and swelling kinetics are also affected, being accelerated for an increased methanol content and exhibiting distinct inhomogeneous swelling patterns depending on the methanol content.

Magnetically-Induced Motion By adding magnetically aligned ellipsoidal magnetic nanoparticles to the reaction solution during SFL, complex-shaped microgels with a predefined magnetic moment were fabricated. These microgels align within a magnetic field, and their motion is controllable. The direction of the magnetic moment was indicated by the alignment direction of the magnetic nanospindles prior to polymerization, which enabled overcoming the microgels' shape-dependent magnetic moment. As a result, the microgels synchronously rotate along a predefined rotation axis within a rotational magnetic field up to a certain critical rotation rate. A higher nanospindle content and a higher magnetic field strength enhance this rotation, and the shape of the microgels significantly influences their rotation capability. The magnetic complex-shaped microgels were additionally positioned inside a microfluidic channel, demonstrating spatio-temporal flow control.

Designed Architecture In addition to individual micrometer-sized complex-shaped microgels, millimeter-sized hierarchically structured hydrogels with designed architecture were created. Despite their size, these so-called patches provide micrometer-sized features whose pattern is defined during fabrication. The patches comprise at least two crosslinking degrees, expressed in highly crosslinked features and low crosslinked regions in between, which are more porous and lower in height. Parameters for a reliable patch formation were investigated with regard to the material system, the polymerization parameters, and the mask pattern. These parameters also directly relate to the mechanical properties of the patches, whereas the proportion of the highly crosslinked regions and their pattern-related connectivity mainly determine the patches' compressibility. The patches are highly tunable, and their use as cell cultivation platforms was demonstrated as one possible application.

Future Perspectives Adapting the shape, porous structure, thermal response, magnetic motion, and architecture of microgels enhances the positive characteristics of microgels and allows to customize them for applications. These various characteristics provide the microgels with unique improvements that may be combined in the future. Anisometric microgels are beneficial compared to spherical microgels as they provide higher surface area, enhanced diffusion efficiency, and anisometric response to external forces. [Liu2024] Adapting the porous structure allows for a change in the loading capacity and stiffness of microgels and directly influences the response time to external stimuli like temperature. [Mou2014] The adjustable thermal response provides an expanded response spectrum and local inhomogeneities during swelling. Ordering the microgels is realized by their induced magnetic response for all applications needing a high order of structure or motion control. Even larger and stable architectures with multiple internal crosslinking degrees are provided by the patches, further configuring the architectures' mechanical properties.

In particular, all these tailorable characteristics are crucial for using microgels as building blocks for tissue scaffolds, which is probably their most promising application. The porosity ensures nutrient supply or enables drug loading [Slau2009], whereas the thermal response enhances the imitation of the cells' environment, provides controlled drug release, or enables cell harvesting. [Hump2014; Wen2019; Schm2010] The alignment of the anisometric microgels due to their magnetic motion provides directionality for guided cell growth [Brau2022] and the micrometer-sized architecture significantly affects the cells' behavior, like their interaction, morphology, or differentiation. [Qazi2022; Babu2021; Solb2023] Tailoring these microgel characteristics enables precisely fitting the environment to the respective cell type, either for comprehensively investigating cell behavior for defined environments or for in vivo tissue scaffolds. Beyond that, anisometric microgels with precisely tunable characteristics are relevant for diverse applications, ranging from encryption units over adsorbents to micromachines. [Tian2020; Foud2023; Liu2024]

Abbreviations and Symbols

Abbreviations

$\dot{\mathrm{R}}$	Reactive free radical
$\mathrm{RM}_n\mathrm{M}_m$	Nonreactive polymer chain
$\mathrm{RM}_n\mathrm{OO}$	Nonreactive oxidized entity
$\mathrm{R}\dot{\mathrm{M}}_i$	Reactive radical intermediate
ABM	Penicillin/streptomycin/amphotericin B
BET	Brunauer-Emmett-Teller
BIS	*N*, *N*'-Methylene bisacrylamide
DAPI	4',6-Diamidino-2-phenylindole
DMD	Digital micromirror device
DMSO	Dimethyl sulfoxide
FBS	Fetal bovine serum
FESEM	Field emission scanning electron microscopy
GMA	Glycidyl methacrylate
HC	Highly crosslinked
IUPAC	International Union of Pure and Applied Chemistry
LAP	Lithium phenyl-2,4,6-trimethyl-benzoyl phosphinate
LC	Low crosslinked

LCST	Lower critical solution temperature
M	Pre-polymer molecule
M^n	Average molecular weight
MAP	Microporous annealed particle
MEHQ	4-Methoxyphenole
MWCO	Molecular weight cut-off
NP	Nanoparticle
OIL	Oxygen inhibition layer
PBS	Phosphate-buffered saline
PDMS	Poly(dimethylsiloxane)
PEG	Poly(ethylene glycol)
PEGDA	Poly(ethylene glycol) diacrylate
PFA	Paraformaldehyde
PI	Photo-initiator
PNIPAM	Poly(*N*-isopropyl acrylamide)
PRINT	Particle replication in non-wetting templates
PVCL	Poly(*N*-vinyl caprolactam)
RT	Room temperature
SAXS	Small-angle x-ray scattering
SDS	Sodium dodecyl sulfate
SEM	Scanning electron microscopy
SFL	Stop-flow lithography

SPION	Superparamagnetic iron oxide nanoparticle
Sulfo-SANPAH	Sulfosuccinimidyl 6-(4’-azido-2’-nitrophenylamino) hexanoate
TEM	Transmission electron microscopy
Triton^{TM} X-100	4-(1,1,3,3-Tetramethylbutyl)-phenyl-polyethylene glycol
Tween-20	Polyoxyethylene (20) sorbitan monolaurate
UCST	Upper critical solution temperature
VPT	Volume phase transition
VPTT	Volume phase transition temperature
w/o	Without
µPTV	Microparticle tracking velocimetry

Symbols

ω_C	Critical rotation rate	[rpm]
A	Area	$[m^2]$
H	Radiant exposure	$[mJ\,mm^{-2}]$
P	Radiant power	[mW]
t	Exposure time	[ms]

Bibliography

[Abra2003] M. Abramoff, P. Magalhães, and S. J. Ram. “Image Processing with ImageJ”. *Biophotonics International* 11 (2003). (Cit. on p. 71).

[Agra2018] G. Agrawal and R. Agrawal. “Functional Microgels: Recent Advances in Their Biomedical Applications”. *Small* 14.39 (2018). DOI: `10.1002/smll.201801724` (cit. on pp. 13, 90).

[Aize2020] J. Aizenberg and P. A. Levkin. “Assembly of Materials Building Blocks into Integrated Complex Functional Systems”. *Advanced Functional Materials* 30.26 (2020). DOI: `10.1002/adfm.202002785` (cit. on p. 90).

[Alap2019] Y. Alapan et al. “Shape-Encoded Dynamic Assembly of Mobile Micromachines”. *Nature Materials* 18.11 (2019). DOI: `10.1038/s41563-019-0407-3` (cit. on p. 66).

[Alke2021] A. S. Alketbi et al. “Impact of PEGDA Photopolymerization in Micro-Stereolithography on 3D Printed Hydrogel Structure and Swelling”. *Soft Matter* 17.30 (2021). DOI: `10.1039/d1sm00483b` (cit. on p. 1).

[Alza2021] H. Alzanbaki, M. Moretti, and C. A. Hauser. “Engineered Microgels: Their Manufacturing and Biomedical Applications”. *Micromachines* 12.1 (2021). DOI: `10.3390/mi12010045` (cit. on pp. 1, 3, 4).

[Babu2021] S. Babu et al. “Controlling Structure with Injectable Biomaterials to Better Mimic Tissue Heterogeneity and Anisotropy”. *Advanced Healthcare Materials* 10.11 (2021). DOI: `10.1002/adhm.202002221` (cit. on pp. 2, 38, 41, 90–92, 131).

[Babu2022] S. Babu et al. “How do the Local Physical, Biochemical, and Mechanical Properties of an Injectable Synthetic Anisotropic Hydrogel Affect Oriented Nerve Growth?” *Advanced Functional Materials* (2022). DOI: `10.1002/adfm.202202468` (cit. on pp. 19, 30, 66, 67).

[Bach2015] H. Bachman et al. “Ultrasoft, Highly Deformable Microgels”. *Soft Matter* 11.10 (2015). DOI: `10.1039/c5sm00047e` (cit. on p. 40).

[Baro2006] B. Baroli. “Photopolymerization of Biomaterials: Issues and Potentialities in Drug Delivery, Tissue Engineering, and Cell Encapsulation Applications”. *Journal of Chemical Technology and Biotechnology* 81.4 (2006). DOI: `10.1002/jctb.1468` (cit. on pp. 1, 4).

[Beeb2000] D. J. Beebe et al. “Functional Hydrogel Structures for Autonomous Flow Control inside Microfluidic Channels”. *Nature* 404.6778 (2000). DOI: `10.1038/35007047` (cit. on p. 66).

[Bell2020] D. J. Bell, D. Roedder, and M. Wessling. “Monodisperse Porous Microspheres with pH-Responsive Permeability and Reactivity”. *ACS Applied Polymer Materials* 2.2 (2020). DOI: `10.1021/acsapm.9b01135` (cit. on pp. 38, 40).

[Bhar2022] S. Bharadwaj et al. “Cononsolvency of Thermoresponsive Polymers: Where we are now and where we are going”. *Soft Matter* 18.15 (2022). DOI: `10.1039/d2sm00146b` (cit. on p. 40).

[Bisw2011] C. S. Biswas et al. “Synthesis and Characterization of Porous Poly(N-Isopropylacrylamide) Hydrogels Prepared in Ethanol-Water Mixtures”. *Journal of Applied Polymer Science* 121.4 (2011). DOI: `10.1002/app.33783` (cit. on pp. 38, 40, 47).

[Bisw2012] C. S. Biswas et al. “Synthesis, Characterization, and Drug Release Properties of Poly(N-Isopropylacrylamide) Gels Prepared in Methanol-Water Cononsolvent Medium”. *Journal of Applied Polymer Science* 125.3 (2012). DOI: `10.1002/app.36318` (cit. on pp. 38, 40, 46–48).

[Bong2009] K. W. Bong, D. C. Pregibon, and P. S. Doyle. “Lock Release Lithography for 3D and Composite Microparticles”. *Lab on a Chip* 9.7 (2009). DOI: `10.1039/b821930c` (cit. on pp. 25, 41).

[Bong2014] K. W. Bong, J. Lee, and P. S. Doyle. “Stop Flow Lithography in Perfluoropolyether (PFPE) Microfluidic Channels”. *Lab on a Chip* 14.24 (2014). DOI: `10.1039/c4lc00877d` (cit. on p. 41).

[Bouh2018] I. Bouhid de Aguiar et al. “Compressive Resistance of Granular-Scale Microgels: From Loose to Dense Packing”. *Colloids and Surfaces A: Physicochemical and Engineering Aspects* 553 (2018). DOI: `10.1016/j.colsurfa.2018.05.064` (cit. on p. 81).

[Brau2022] D. L. Braunmiller et al. “Pre-Programmed Rod-Shaped Microgels to Create Multi-Directional Anisogels for 3D Tissue Engineering”. *Advanced Functional Materials* 32.50 (2022). DOI: `10.1002/adfm.202202430` (cit. on pp. 20–22, 66–68, 92, 131).

[Bril2023] M. Bril et al. “Shape-Morphing Photoresponsive Hydrogels Reveal Dynamic Topographical Conditioning of Fibroblasts”. *Advanced Science* 10.31 (2023). DOI: `10.1002/advs.202303136` (cit. on pp. 90, 122).

[Bulu2023] S. Bulut et al. “Tuning the Porosity of Dextran Microgels with Supramacromolecular Nanogels as Soft Sacrificial Templates”. *Small* 19.45 (2023). DOI: `10.1002/smll.202303783` (cit. on pp. 40, 91).

[Butc2009] D. T. Butcher, T. Alliston, and V. M. Weaver. “A Tense Situation: Forcing Tumour Progression”. *Nature Reviews Cancer* 9.2 (2009). DOI: `10.1038/nrc2544` (cit. on p. 125).

[Call2023] S. J. P. Callens et al. “Emergent Collective Organization of Bone Cells in Complex Curvature Fields”. *Nature Communications* 14.1 (2023). DOI: `10.1038/s41467-023-36436-w` (cit. on pp. 30, 92).

[Cava2017] A. Cavallo et al. “Photo-Crosslinked Poly(Ethylene Glycol) Diacrylate (PEGDA) Hydrogels from Low Molecular Weight Prepolymer: Swelling and Permeation Studies”. *Journal of Applied Polymer Science* 134.2 (2017). DOI: `10.1002/app.44380` (cit. on p. 81).

[Chan2019] Y. Chandorkar et al. “Cellular Responses to Beating Hydrogels to Investigate Mechanotransduction”. *Nature Communications* 10.1 (2019). DOI: `10.1038/s41467-019-11475-4` (cit. on pp. 62, 123).

[Chen2006] H. Cheng, L. Shen, and C. Wu. “LLS and FTIR Studies on the Hysteresis in Association and Dissociation of Poly (N-Isopropylacrylamide) Chains in Water”. *Macromolecules* 39.6 (2006). DOI: `10.1021/ma052561m` (cit. on pp. 17, 18, 39, 59).

[Chen2021] R. Chen et al. “In Situ Self-Assembly of Gold Nanorods with Thermal-Responsive Microgel for Multi-Synergistic Remote Drug Delivery”. *Advanced Composites and Hybrid Materials* 5.3 (2021). DOI: `10.1007/s42114-021-00306-0` (cit. on p. 62).

[Chet2013] A. Chetty et al. “A Versatile Characterization of Poly (N-Isopropylacrylamideco-N, N’-Methylene-Bis-Acrylamide) Hydrogels for Composition, Mechanical Strength, and Rheology”. *eXPRESS Polymer Letters* 7.1 (2013). DOI: 10.3144/expresspolymlett.2013.9 (cit. on pp. 40, 45).

[Chir2015] N. Chirani et al. “History and Applications of Hydrogels”. *Journal of Biomedical Sciences* 4.02 (2015). DOI: 10.4172/2254-609X.100013 (cit. on p. 2).

[Choi2011] E. Choi et al. “Formation of Hydrogel Membranes in Microchannels and its Applications”. In*2011 IEEE International Conference on Robotics and Biomimetics*. IEEE, 2011, pp. 1890–1894. DOI: 10.1109/ROBIO.2011.6181566 (cit. on p. 90).

[Chu2007] L.-Y. Chu et al. “Monodisperse Thermoresponsive Microgels with Tunable Volume-Phase Transition Kinetics”. *Advanced Functional Materials* 17.17 (2007). DOI: 10.1002/adfm.200700379 (cit. on pp. 14, 39).

[Chun2008] S. E. Chung et al. “Guided and Fluidic Self-Assembly of Microstructures Using Railed Microfluidic Channels”. *Nature Materials* 7.7 (2008). DOI: 10.1038/nmat2208 (cit. on pp. 25, 29).

[Corn2003] R. M. Cornell, U. Schwertmann, et al. *The Iron Oxides: Structure, Properties, Reactions, Occurrences, and Uses*. Vol. 664. Wiley Weinheim, 2003. DOI: 10.1002/3527602097 (cit. on p. 22).

[Cui2018] J. Cui et al. “Fabrication of Perfusable 3D Hepatic Lobule-Like Constructs through Assembly of Multiple Cell Type Laden Hydrogel Microstructures”. *Biofabrication* 11.1 (2018). DOI: 10.1088/1758-5090/aaf3c9 (cit. on p. 92).

[Darl2020] N. J. Darling et al. “Click by Click Microporous Annealed Particle (MAP) Scaffolds”. *Advanced Healthcare Materials* 9.10 (2020). DOI: 10.1002/adhm.201901391 (cit. on p. 27).

[Dend2006] D. Dendukuri et al. “Continuous-Flow Lithography for High-Throughput Microparticle Synthesis”. *Nature Materials* 5.5 (2006). DOI: 10.1038/nmat1617 (cit. on p. 24).

[Dend2007a] D. Dendukuri, T. A. Hatton, and P. S. Doyle. “Synthesis and Self-Assembly of Amphiphilic Polymeric Microparticles”. *Langmuir* 23.8 (2007). DOI: `10.1021/la062512i` (cit. on pp. 41, 92).

[Dend2007b] D. Dendukuri et al. “Stop-Flow Lithography in a Microfluidic Device”. *Lab on a Chip* 7.7 (2007). DOI: `10.1039/b703457a` (cit. on pp. 6–8, 24, 43, 95).

[Dend2008] D. Dendukuri et al. “Modeling of Oxygen-Inhibited Free Radical Photopolymerization in a PDMS Microfluidic Device”. *Macromolecules* 41.22 (2008). DOI: `10.1021/ma801219w` (cit. on pp. 4–6, 9, 10, 12, 43, 47, 61, 102, 112).

[Deut2024] A. T. Deutsch Lukatsky et al. “Hydrogels Based on Crosslinked Polyethylene Glycol Diacrylate and Fish Skin Gelatin”. *European Polymer Journal* 210 (2024). DOI: `10.1016/j.eurpolymj.2024.112990` (cit. on p. 3).

[Dudo2015] J. Dudowicz, K. F. Freed, and J. F. Douglas. “Communication: Co-solvency and Cononsolvency Explained in terms of a Flory-Huggins Type Theory”. *Journal of Chemical Physics* 143.13 (2015). DOI: `10.1063/1.4932061` (cit. on p. 40).

[Dunc2012] W. J. Duncanson et al. “Microfluidic Synthesis of Monodisperse Porous Microspheres with Size-Tunable Pores”. *Soft Matter* 8.41 (2012). DOI: `10.1039/c2sm25694k` (cit. on pp. 38, 40).

[Eddi2004] D. T. Eddington and D. J. Beebe. “Flow Control with Hydrogels”. *Advanced Drug Delivery Reviews* 56.2 (2004). DOI: `10.1016/j.addr.2003.08.013` (cit. on p. 66).

[El-S2013] I. M. El-Sherbiny and M. H. Yacoub. “Hydrogel Scaffolds for Tissue Engineering: Progress and Challenges”. *Global Cardiology Science and Practice* 2013.3 (2013). DOI: `10.5339/gcsp.2013.38` (cit. on p. 2).

[Fair2009] B. D. Fairbanks et al. “Photoinitiated Polymerization of PEG-diacrylate with Lithium phenyl-2, 4, 6-trimethylbenzoylphosphinate: Polymerization Rate and Cytocompatibility”. *Biomaterials* 30.35 (2009). DOI: `10.1016/j.biomaterials.2009.08.055` (cit. on p. 5).

[Feng2016] Q. Feng et al. “Mechanically Resilient, Injectable, and Bioadhesive Supramolecular Gelatin Hydrogels Crosslinked by Weak Host-Guest Interactions Assist Cell Infiltration and In Situ Tissue Regeneration”. *Biomaterials* 101 (2016). DOI: `10.1016/j.biomaterials.2016.05.043` (cit. on p. 38).

[Flor1943] P. J. Flory and J. Rehner. “Statistical Mechanics of Cross-Linked Polymer Networks II. Swelling”. *The Journal of Chemical Physics* 11.11 (1943). DOI: `10.1063/1.1723792` (cit. on pp. 14, 17).

[Foud2023] R. Foudazi et al. “Porous Hydrogels: Present Challenges and Future Opportunities”. *Langmuir* 39.6 (2023). DOI: `10.1021/acs.langmuir.2c02253` (cit. on pp. 13, 14, 16, 38–40, 111, 131).

[Fu2019] J. Fu et al. “Hydrogel Properties and Applications”. *Journal of Materials Chemistry B* 7.10 (2019). DOI: `10.1039/c9tb90023c` (cit. on p. 1).

[Gan2023] Z. Gan et al. “One-Step Generation of Porous GelMA Microgels by Droplet-Based Chaotic Advection Effect”. *Advanced Materials Technologies* 8.4 (2023). DOI: `10.1002/admt.202201102` (cit. on p. 40).

[Garc2020] B. Garcia-Pinel et al. “Magnetically Active PNIPAM Nanosystems as Temperature-Sensitive Biocompatible Structures for Controlled Drug Delivery”. *Artificial Cells, Nanomedicine, and Biotechnology* 48.1 (2020). DOI: `10.1080/21691401.2020.1773488` (cit. on pp. 38, 39, 62).

[Gauv2012] R. Gauvin et al. “Microfabrication of Complex Porous Tissue Engineering Scaffolds using 3D Projection Stereolithography”. *Biomaterials* 33.15 (2012). DOI: `10.1016/j.biomaterials.2012.01.048` (cit. on pp. 30, 31, 92).

[Gera2023] J. L. Gerardo-Nava et al. “Transformative Materials to Create 3D Functional Human Tissue Models In Vitro in a Reproducible Manner”. *Advanced Healthcare Materials* 12.20 (2023). DOI: `10.1002/adhm.202301030` (cit. on pp. 3, 27, 90–92).

[Ghim2024] A. Ghimire et al. “Hierarchical Nested Honeycomb-Based Energy Absorbers: Design Factors and Tailorable Mechanical Properties”. *Interface Focus* 14.3 (2024). DOI: `10.1098/rsfs.2023.0066` (cit. on p. 122).

[Gjor2022] N. Gjorevski et al. “Tissue Geometry Drives Deterministic Organoid Patterning”. *Science* 375.6576 (2022). DOI: `10.1126/science.aaw9021` (cit. on pp. 30, 90, 92).

[Grif2006] D. J. Griffon et al. “Chitosan Scaffolds: Interconnective Pore Size and Cartilage Engineering”. *Acta Biomaterialia* 2.3 (2006). DOI: `10.1016/j.actbio.2005.12.007` (cit. on pp. 38, 41).

[Grif2015] D. R. Griffin et al. “Accelerated Wound Healing by Injectable Microporous Gel Scaffolds Assembled from Annealed Building Blocks”. *Nature Materials* 14.7 (2015). DOI: `10.1038/nmat4294` (cit. on pp. 27, 28, 38, 91).

[Guer2019] L. P. B. Guerzoni et al. “Cell Encapsulation in Soft, Anisometric Poly(Ethylene) Glycol Microgels Using a Novel Radical-Free Microfluidic System”. *Small* 15.20 (2019). DOI: `10.1002/smll.201900692` (cit. on pp. 38, 41).

[Haki2014] N. Hakimi et al. “One-Step Two-Dimensional Microfluidics-Based Synthesis of Three-Dimensional Particles”. *Advanced Materials* 26.9 (2014). DOI: `10.1002/adma.201304378` (cit. on pp. 6, 10–12, 20, 24, 26, 27, 61, 67, 68, 102).

[Han2017] K. Han et al. “Sequence-Encoded Colloidal Origami and Microbot Assemblies from Patchy Magnetic Cubes”. *Science Advances* 3.8 (2017). DOI: `10.1126/sciadv.1701108` (cit. on p. 66).

[Haq2017] M. A. Haq, Y. Su, and D. Wang. “Mechanical Properties of PNIPAM Based Hydrogels: A Review”. *Materials Science and Engineering: C* 70 (2017). DOI: `10.1016/j.msec.2016.09.081` (cit. on pp. 4, 13, 15, 16).

[Hert2013] Y. Hertle and T. Hellweg. “Thermoresponsive Copolymer Microgels”. *Journal of Materials Chemistry B* 1.43 (2013). DOI: `10.1039/c3tb21143f` (cit. on p. 16).

[Hesk1968] M. Heskins and J. E. Guillet. “Solution Properties of Poly (N-Isopropylacrylamide)”. *Journal of Macromolecular Science—Chemistry* 2.8 (1968). DOI: `10.1080/10601326808051910` (cit. on p. 15).

[Hess2018] T. Hessberger, L. B. Braun, and R. Zentel. “Interfacial Self-Assembly of Amphiphilic Dual Temperature Responsive Actuating Janus Particles”. *Advanced Functional Materials* 28.21 (2018). DOI: `10.1002/adfm.201800629` (cit. on pp. 29, 30, 92).

[Hild2022] M. Hildebrandt et al. “SAXS Investigation of Core–Shell Microgels with High Scattering Contrast Cores: Access to Structure Factor and Volume Fraction”. *Macromolecules* 55.7 (2022). DOI: `10.1021/acs.macromol.2c00100` (cit. on p. 55).

[Hübs2015] N. Hübsch et al. “Matrix Elasticity of Void-Forming Hydrogels Controls Transplanted-Stem-Cell-Mediated Bone Formation”. *Nature Materials* 14.12 (2015). DOI: `10.1038/nmat4407` (cit. on pp. 38, 41).

[Hump2014] J. D. Humphrey, E. R. Dufresne, and M. A. Schwartz. “Mechanotransduction and Extracellular Matrix Homeostasis”. *Nature Reviews Molecular Cell Biology* 15.12 (2014). DOI: `10.1038/nrm3896` (cit. on pp. 39, 131).

[Hwan2008] D. K. Hwang, D. Dendukuri, and P. S. Doyle. “Microfluidic-Based Synthesis of Non-Spherical Magnetic Hydrogel Microparticles”. *Lab on a Chip* 8.10 (2008). DOI: `10.1039/b805176c` (cit. on pp. 19–21, 66, 67).

[Hwan2017] M. Y. Hwang et al. “Generation and Characterization of Monodisperse Deformable Alginate and PNIPAM Microparticles with a Wide Range of Shear Moduli”. *Soft Matter* 13.34 (2017). DOI: `10.1039/c7sm01079f` (cit. on p. 40).

[Itoh2003] H. Itoh and T. Sugimoto. “Systematic Control of Size, Shape, Structure, and Magnetic Properties of Uniform Magnetite and Maghemite Particles”. *Journal of Colloid and Interface Science* 265.2 (2003). DOI: `10.1016/S0021-9797(03)00511-3` (cit. on pp. 22, 67).

[Janm2020] P. A. Janmey, D. A. Fletcher, and C. A. Reinhart-King. “Stiffness Sensing by Cells”. *Physiological Reviews* 100.2 (2020). DOI: `10.1152/physrev.00013.2019` (cit. on pp. 2, 14, 38, 90, 125).

[Karg2019] M. Karg et al. “Nanogels and Microgels: From Model Colloids to Applications, Recent Developments, and Future Trends”. *Langmuir* 35.19 (2019). DOI: `10.1021/acs.langmuir.8b04304` (cit. on pp. 1, 38).

[Kim2008] P. Kim et al. “Soft Lithography for Microfluidics: A Review”. *BioChip Journal* 2.1 (2008). (Cit. on p. 42).

[Kim2009] D. Kim et al. “Synthesis of Uniform Ferrimagnetic Magnetite Nanocubes”. *Journal of the American Chemical Society* 131.2 (2009). DOI: `10.1021/ja8086906` (cit. on p. 22).

[Kim2011] L. N. Kim et al. “Single Exposure Fabrication and Manipulation of 3D Hydrogel Cell Microcarriers”. *Lab on a Chip* 11.1 (2011). DOI: `10.1039/c0lc00369g` (cit. on pp. 10, 11, 24, 26, 27, 30, 31, 61).

[Kitt2023] Y. Kittel et al. “Varying the Stiffness and Diffusivity of Rod-Shaped Microgels Independently through Their Molecular Building Blocks”. *Angewandte Chemie, International Edition in English* 62.44 (2023). DOI: `10.1002/anie.202309779` (cit. on pp. 14, 46, 90, 105, 106, 123).

[Krüg2019] A. J. Krüger et al. “Compartmentalized Jet Polymerization as a High-Resolution Process to Continuously Produce Anisometric Microgel Rods with Adjustable Size and Stiffness”. *Advanced Materials* 31.49 (2019). DOI: `10.1002/adma.201903668` (cit. on pp. 24, 40).

[Lee2009] S. A. Lee et al. “Three-Dimensional Fabrication of Heterogeneous Microstructures Using Soft Membrane Deformation and Optofluidic Maskless Lithography”. *Lab on a Chip* 9.12 (2009). DOI: `10.1039/b819999j` (cit. on p. 26).

[Lee2010] H. Lee et al. “Colour-Barcoded Magnetic Microparticles for Multiplexed Bioassays”. *Nature Materials* 9.9 (2010). DOI: `10.1038/nmat2815` (cit. on p. 67).

[Lei2007] K. F. Lei et al. “A Vortex Pump-Based Optically-Transparent Microfluidic Platform for Biotech and Medical Applications”. *Proceedings of the Institution of Mechanical Engineers, Part H: Journal of Engineering in Medicine* 221.2 (2007). DOI: `10.1243/09544119JEIM189` (cit. on p. 66).

[Li1990] Y. Li and T. Tanaka. “Kinetics of Swelling and Shrinking of Gels”. *The Journal of Chemical Physics* 92.2 (1990). DOI: `10.1063/1.458148` (cit. on p. 17).

[Ligo2014] S. C. Ligon et al. “Strategies to Reduce Oxygen Inhibition in Photoinduced Polymerization”. *Chemical Reviews* 114.1 (2014). DOI: `10.1021/cr3005197` (cit. on pp. 6, 8).

[Lin1999] S.-Y. Lin, K.-S. Chen, and L. Run-Chu. “Drying Methods Affecting the Particle Sizes, Phase Transition, Deswelling/Reswelling Processes and Morphology of Poly (N-Isopropylacrylamide) Microgel Beads”. *Polymer* 40.23 (1999). DOI: `10.1016/S0032-3861(98)00872-6` (cit. on p. 111).

[Liu2017] M. Liu et al. “Injectable Hydrogels for Cartilage and Bone Tissue Engineering”. *Bone Research* 5.1 (2017). DOI: `10.1038/boneres.2017.14` (cit. on p. 38).

[Liu2024] Y. Liu, Z. Chen, and J. Xu. “Recent Advances in the Microfluidic Generation of Shape-Controllable Hydrogel Microparticles and their Applications”. *Green Chemical Engineering* 5.1 (2024). DOI: `10.1016/j.gce.2023.02.002` (cit. on pp. 2, 3, 6, 13, 14, 23, 24, 68, 90, 92, 122, 131).

[Löls2018] J. Lölsberg et al. “3D Nanofabrication inside Rapid Prototyped Microfluidic Channels Showcased by Wet-Spinning of Single Micrometre Fibres”. *Lab on a Chip* 18.9 (2018). DOI: `10.1039/C7LC01366C` (cit. on p. 42).

[Lope2017] C. G. Lopez and W. Richtering. “Does Flory–Rehner theory quantitatively describe the swelling of thermoresponsive microgels?” *Soft Matter* 13.44 (2017). DOI: `10.1039/c7sm01274h` (cit. on p. 17).

[Lu2006] Y. Lu et al. “A Digital Micro-Mirror Device-Based System for the Microfabrication of Complex, Spatially Patterned Tissue Engineering Scaffolds”. *Journal of Biomedical Materials Research, Part A* 77.2 (2006). DOI: `10.1002/jbm.a.30601` (cit. on pp. 30, 31, 92).

[Lu2010] Y. Lu et al. “Origin of Hysteresis Observed in Association and Dissociation of Polymer Chains in Water”. *PCCP Physical Chemistry Chemical Physics* 12.13 (2010). DOI: `10.1039/b918969f` (cit. on pp. 17, 39, 59).

[Lüke2022] A. Lüken et al. “Fabrication, Flow Assembly, and Permeation of Microscopic Any-Shape Particles”. *Small* 18.15 (2022). DOI: `10.1002/smll.202107508` (cit. on p. 24).

[Mahm2011] M. Mahmoudi et al. “Superparamagnetic Iron Oxide Nanoparticles (SPIONs): Development, Surface Modification and Applications in Chemotherapy”. *Advanced Drug Delivery Reviews* 63.1-2 (2011). DOI: `10.1016/j.addr.2010.05.006` (cit. on pp. 22, 66).

[Mali2017] V. Malik et al. “Hybrid Magnetic Iron Oxide Nanoparticles with Tunable Field-Directed Self-Assembly”. *Nanoscale* 9.38 (2017). DOI: `10.1039/c7nr04518b` (cit. on pp. 22, 23, 67, 68).

[Maru2006] S. Maruo and H. Inoue. “Optically Driven Micropump Produced by Three-Dimensional Two-Photon Microfabrication”. *Applied Physics Letters* 89.14 (2006). DOI: `10.1063/1.2358820` (cit. on p. 66).

[Matt2006] M. Matteucci et al. “Compact Micropumping System Based on LIGA Fabricated Microparts”. *Microelectronic Engineering* 83.4-9 (2006). DOI: `10.1016/j.mee.2006.01.259` (cit. on p. 66).

[Miks2022] C. E. Miksch et al. “4D Printing of Extrudable and Degradable Poly-(Ethylene Glycol) Microgel Scaffolds for Multidimensional Cell Culture”. *Small* 18.36 (2022). DOI: `10.1002/smll.202200951` (cit. on pp. 27, 91).

[Mou2014] C.-L. Mou et al. “Monodisperse and Fast-Responsive Poly (N-Isopropylacrylamide) Microgels with Open-Celled Porous Structure”. *Langmuir* 30.5 (2014). DOI: `10.1021/la4046379` (cit. on pp. 13, 14, 38–40, 56, 131).

[Mour2021] A. Mourran et al. “Microgel that Swims to the Beat of Light”. *The European Physical Journal E* 44.6 (2021). DOI: `10.1140/epje/s10189-021-00084-z` (cit. on pp. 62, 66).

[Nale2015] S. E. Naleway et al. “Structural Design Elements in Biological Materials: Application to Bioinspiration”. *Advanced Materials* 27.37 (2015). DOI: `10.1002/adma.201502403` (cit. on pp. 92, 122).

[News2019] J. P. Newsom, K. A. Payne, and M. D. Krebs. “Microgels: Modular, Tunable Constructs for Tissue Regeneration”. *Acta Biomaterialia* 88 (2019). DOI: `10.1016/j.actbio.2019.02.011` (cit. on pp. 2, 38).

[Noth2019] K. Nothdurft et al. "Enrichment of Methanol inside PNIPAM Gels in the Cononsolvency-Induced Collapse". *PCCP Physical Chemistry Chemical Physics* 21.41 (2019). DOI: `10.1039/c9cp04383g` (cit. on pp. 40, 56).

[Nune2010] J. Nunes et al. "Multifunctional Shape and Size Specific Magneto-Polymer Composite Particles". *Nano Letters* 10.4 (2010). DOI: `10.1021/nl904152e` (cit. on pp. 20–22, 67).

[OBri2011] F. J. O'Brien. "Biomaterials & Scaffolds for Tissue Engineering". *Materials Today* 14.3 (2011). DOI: `10.1016/S1369-7021(11)70058-X` (cit. on p. 2).

[Ocañ1999] M. Ocaña, M. P. Morales, and C. J. Serna. "Homogeneous Precipitation of Uniform -Fe2O3Particles from Iron Salts Solutions in the Presence of Urea". *Journal of Colloid and Interface Science* 212.2 (1999). DOI: `https://doi.org/10.1006/jcis.1998.6042` (cit. on pp. 22, 68).

[Ouya2020] L. Ouyang et al. "Void-free 3D Bioprinting for In-situ Endothelialization and Microfluidic Perfusion". *Advanced Functional Materials* 30.26 (2020). DOI: `10.1002/adfm.201909009` (cit. on p. 91).

[Pape2007] B. J. Papenburg et al. "One-Step Fabrication of Porous Micropatterned Scaffolds to Control Cell Behavior". *Biomaterials* 28.11 (2007). DOI: `10.1016/j.biomaterials.2006.12.023` (cit. on pp. 30, 92).

[Pasz2005] M. J. Paszek et al. "Tensional Homeostasis and the Malignant Phenotype". *Cancer Cell* 8.3 (2005). DOI: `10.1016/j.ccr.2005.08.010` (cit. on p. 38).

[Patr2022] M. D. Patrick et al. "Injectable Nanoporous Microgels Generate Vascularized Constructs and Support Bone Regeneration in Critical-Sized Defects". *Scientific Reports* 12.1 (2022). DOI: `10.1038/s41598-022-19968-x` (cit. on p. 46).

[Paul2015] K. S. Paulsen, D. Di Carlo, and A. J. Chung. "Optofluidic Fabrication for 3D-Shaped Particles". *Nature Communications* 6.1 (2015). DOI: `10.1038/ncomms7976` (cit. on p. 41).

[Pelt2010] R. Pelton. "Poly (N-Isopropylacrylamide)(PNIPAM) is never Hydrophobic". *Journal of Colloid and Interface Science* 348.2 (2010). DOI: `10.1016/j.jcis.2010.05.034` (cit. on p. 15).

[Pfaf2024] B. N. Pfaff, C. C. Flanagan, and D. R. Griffin. “Microporous Annealed Particle (MAP) Scaffold Pore Size Influences Mesenchymal Stem Cell Metabolism and Proliferation Without Changing CD73, CD90, and CD105 Expression Over Two Weeks”. *Advanced Biology* 8.2 (2024). DOI: 10.1002/adbi.202300482 (cit. on pp. 27, 91).

[Pich2010] A. Pich and W. Richtering. *Chemical Design of Responsive Microgels*. Vol. 234. Springer, 2010. DOI: 10.1007/978-3-642-16379-1 (cit. on pp. 4, 15, 16).

[Plam2017] F. A. Plamper and W. Richtering. “Functional Microgels and Microgel Systems”. *Accounts of Chemical Research* 50.2 (2017). DOI: 10.1021/acs.accounts.6b00544 (cit. on pp. 39, 40).

[Qazi2022] T. H. Qazi et al. “Anisotropic Rod-Shaped Particles Influence Injectable Granular Hydrogel Properties and Cell Invasion”. *Advanced Materials* 34.12 (2022). DOI: 10.1002/adma.202109194 (cit. on pp. 27, 28, 90–92, 131).

[Ques2011] M. Quesada-Pérez et al. “Gel Swelling Theories: The Classical Formalism and Recent Approaches”. *Soft Matter* 7.22 (2011). DOI: 10.1039/c1sm06031g (cit. on p. 17).

[Raj 2023] K. Raj M et al. “Bio-Inspired Microfluidics: A Review”. *Biomicrofluidics* 17.5 (2023). DOI: 10.1063/5.0161809 (cit. on p. 91).

[Raue2022] S. B. Rauer et al. “Porous PEDOT:PSS Particles and their Application as Tunable Cell Culture Substrate”. *Advanced Materials Technologies* 7.1 (2022). DOI: 10.1002/admt.202100836 (cit. on pp. 38, 40).

[Ried2016] M. S. Riederer et al. “Injectable and Microporous Scaffold of Densely-Packed, Growth Factor-Encapsulating Chitosan Microgels”. *Carbohydrate Polymers* 152 (2016). DOI: 10.1016/j.carbpol.2016.07.052 (cit. on p. 38).

[Rodr2017] F. Rodrıguez-Dıaz, A. Castellanos-Suárez, and A. Lozsán. “A Phenomenological Order Approach to the Volume Phase Transition in Microgel Particles”. *PCCP Physical Chemistry Chemical Physics* 19.25 (2017). DOI: 10.1039/c7cp02567j (cit. on p. 16).

[Roll2005] J. P. Rolland et al. “Direct Fabrication and Harvesting of Monodisperse, Shape-Specific Nanobiomaterials”. *Journal of the American Chemical Society* 127.28 (2005). DOI: `10.1021/ja051977c` (cit. on p. 24).

[Romm2022] D. Rommel et al. “Functionalized Microgel Rods Interlinked into Soft Macroporous Structures for 3D Cell Culture”. *Advanced Science* 9.10 (2022). DOI: `10.1002/advs.202103554` (cit. on pp. 27, 38, 41, 91, 92, 123).

[Rose2017] J. C. Rose et al. “Nerve Cells Decide to Orient inside an Injectable Hydrogel with Minimal Structural Guidance”. *Nano Letters* 17.6 (2017). DOI: `10.1021/acs.nanolett.7b01123` (cit. on pp. 30, 66, 67, 92).

[Rose2020a] J. C. Rose et al. “How Much Physical Guidance is Needed to Orient Growing Axons in 3D Hydrogels?” *Advanced Healthcare Materials* 9.21 (2020). DOI: `10.1002/adhm.202000886` (cit. on p. 67).

[Rose2020b] J. C. Rose et al. “Predicting the Orientation of Magnetic Microgel Rods for Soft Anisotropic Biomimetic Hydrogels”. *Polymer Chemistry* 11.2 (2020). DOI: `10.1039/C9PY01008D` (cit. on pp. 21, 22, 67).

[Saad2023] M. Saadli et al. “Thermally and Magnetically Programmable Hydrogel Microactuators”. *Small* n/a.n/a (2023). DOI: `10.1002/smll.202207035` (cit. on p. 67).

[Sabh2016] M. Sabharwal et al. “Analysis of Catalyst Layer Microstructures: From Imaging to Performance”. *Fuel Cells* 16.6 (2016). DOI: `10.1002/fuce.201600008` (cit. on p. 46).

[Sade2012] R. Sadeghi and F. Jahani. “Salting-in and Salting-out of Water-Soluble Polymers in Aqueous Salt Solutions”. *Journal of Physical Chemistry B* 116.17 (2012). DOI: `10.1021/jp300665b` (cit. on p. 81).

[Sanc2019] L. M. Sanchez et al. “Effect of PAA-Coated Magnetic Nanoparticles on the Performance of PVA-Based Hydrogels Developed to be Used as Environmental Remediation Devices”. *Journal of Nanoparticle Research* 21.3 (2019). DOI: `10.1007/s11051-019-4499-0` (cit. on p. 66).

[Saxe2014] S. Saxena et al. “Microgel Film Dynamics Modulate Cell Adhesion Behavior”. *Soft Matter* 10.9 (2014). DOI: `10.1039/C3SM52518J` (cit. on p. 38).

[Sche2014] C. Scherzinger et al. “Cononsolvency of Poly-N-Isopropyl Acrylamide (PNIPAM): Microgels versus Linear Chains and Macrogels”. *Current Opinion in Colloid & Interface Science* 19.2 (2014). DOI: `10.1016/j.cocis.2014.03.011` (cit. on pp. 40, 45, 56).

[Schm2010] S. Schmidt et al. “Adhesion and Mechanical Properties of PNIPAM Microgel Films and Their Potential Use as Switchable Cell Culture Substrates”. *Advanced Functional Materials* 20.19 (2010). DOI: `10.1002/adfm.201000730` (cit. on pp. 38, 39, 62, 131).

[Scot2022] A. Scotti et al. “How Softness Matters in Soft Nanogels and Nanogel Assemblies”. *Chemical Reviews* 122.13 (2022). DOI: `10.1021/acs.chemrev.2c00035` (cit. on p. 38).

[Shin1987] A. Shine and R. Armstrong. “The Rotation of a Suspended Axisymmetric Ellipsoid in a Magnetic Field”. *Rheologica Acta* 26 (1987). DOI: `10.1007/BF01331973` (cit. on p. 23).

[Sier2014] B. Sierra-Martin et al. “Structure and Polymer Dynamics within PNIPAM-Based Microgel Particles”. *Advances in Colloid and Interface Science* 205 (2014). DOI: `10.1016/j.cis.2013.11.001` (cit. on pp. 14–17, 39).

[Slau2009] B. V. Slaughter et al. “Hydrogels in Regenerative Medicine”. *Advanced Materials* 21.32-33 (2009). DOI: `10.1002/adma.200802106` (cit. on pp. 38, 131).

[Solb2023] A. A. Solbu et al. “Assessing Cell Migration in Hydrogels: An Overview of Relevant Materials and Methods”. *Materials Today Bio* 18 (2023). DOI: `10.1016/j.mtbio.2022.100537` (cit. on pp. 90, 122, 131).

[Stoc2022] F. Stockmeier et al. “Measurement of Electrokinetically Induced Hydrodynamics at Ion-Selective Interfaces Using 3D Micro Particle Tracking Velocimetry (µPTV)”. *MethodsX* 9 (2022). DOI: `10.1016/j.mex.2022.101814` (cit. on p. 72).

[Suh2012a] S. K. Suh et al. “Synthesis of Magnetic Hydrogel Microparticles for Bioassays and Tweezer Manipulation in Microwells”. *Microfluidics and Nanofluidics* 13.4 (2012). DOI: `10.1007/s10404-012-0977-8` (cit. on pp. 67, 81).

[Suh2012b] S. K. Suh et al. “Synthesis of Nonspherical Superparamagnetic Particles: In Situ Coprecipitation of Magnetic Nanoparticles in Microgels Prepared by Stop-Flow Lithography”. *Journal of the American Chemical Society* 134.17 (2012). DOI: `10.1021/ja209245v` (cit. on pp. 19, 20, 67).

[Sui2011] X. Sui et al. “Probing the Collapse Dynamics of Poly(N-Isopropylacrylamide) Brushes by AFM: Effects of Co-Nonsolvency and Grafting Densities”. *Small* 7.10 (2011). DOI: `10.1002/smll.201002229` (cit. on pp. 39, 40).

[Sulu2017] E. Sulu et al. “Synthesis, Characterization, and Drug Release Properties of Macroporous Dual Stimuli Responsive Stereo Regular Nanocomposites Gels of Poly(N-Isopropylacrylamide) and Graphene Oxide”. *Journal of Porous Materials* 24.2 (2017). DOI: `10.1007/s10934-016-0272-2` (cit. on pp. 40, 47).

[Sun2008] B. Sun et al. “A FTIR and 2D-IR Spectroscopic Study on the Microdynamics Phase Separation Mechanism of the Poly (N-Isopropylacrylamide) Aqueous Solution”. *Macromolecules* 41.4 (2008). DOI: `10.1021/ma702062h` (cit. on pp. 17, 39, 59).

[Sung2021] B. Sung, M.-H. Kim, and L. Abelmann. “Magnetic Microgels and Nanogels: Physical Mechanisms and Biomedical Applications”. *Bioengineering & Translational Medicine* 6.1 (2021). DOI: `10.1002/btm2.10190` (cit. on p. 66).

[Sutu2022] A. C. Suturin et al. “Annealing High Aspect Ratio Microgels into Macroporous 3D Scaffolds Allows for Higher Porosities and Effective Cell Migration”. *Advanced Healthcare Materials* 11.24 (2022). DOI: `10.1002/adhm.202200989` (cit. on pp. 27, 91).

[Tana1979] T. Tanaka and D. J. Fillmore. “Kinetics of Swelling of Gels”. *The Journal of Chemical Physics* 70.3 (1979). DOI: `10.1063/1.437602` (cit. on p. 17).

[Tana2008] F. Tanaka, T. Koga, and F. M. Winnik. “Temperature-Responsive Polymers in Mixed Solvents: Competitive Hydrogen Bonds Cause Cononsolvency”. *Physical Review Letters* 101.2 (2008). DOI: `10.1103/PhysRevLett.101.028302` (cit. on pp. 18, 40).

[Terr2002] A. Terray, J. Oakey, and D. W. Marr. “Microfluidic Control Using Colloidal Devices”. *Science* 296.5574 (2002). DOI: `10.1126/science.1072133` (cit. on p. 66).

[Thor2011] J. B. Thorne, G. J. Vine, and M. J. Snowden. “Microgel Applications and Commercial Considerations”. *Colloid and Polymer Science* 289 (2011). DOI: `10.1007/s00396-010-2369-5` (cit. on p. 1).

[Tian2020] Y. Tian and L. Wang. “Complex Three-Dimensional Microparticles from Microfluidic Lithography”. *Electrophoresis* (2020). DOI: `10.1002/elps.201900322` (cit. on pp. 6, 23, 24, 30, 31, 90, 131).

[Unad2011] H. V. Unadkat et al. “An Algorithm-Based Topographical Biomaterials Library to Instruct Cell Fate”. *PNAS* 108.40 (2011). DOI: `10.1073/pnas.1109861108` (cit. on pp. 30, 91, 92, 122).

[Wan2008] J. Wan et al. “Controllable Microfluidic Production of Microbubbles in Water-in-Oil Emulsions and the Formation of Porous Microparticles”. *Advanced Materials* 20.17 (2008). DOI: `10.1002/adma.200800628` (cit. on pp. 38, 40).

[Wang2010] H. Wang et al. “Injectable Cardiac Tissue Engineering for the Treatment of Myocardial Infarction”. *Journal of Cellular and Molecular Medicine* 14.5 (2010). DOI: `10.1111/j.1582-4934.2010.01046.x` (cit. on p. 38).

[Weig2023] N. Weigel et al. “Fabrication of Thermoresponsive and Multimaterial Hydrogel Sheets by Spatially Controlled Aspiration and Interconnection of Microgel Building Blocks”. *Advanced Materials Technologies* 8.23 (2023). DOI: `10.1002/admt.202300374` (cit. on pp. 29, 91).

[Wen2019] Y. Wen et al. “A Responsive Porous Hydrogel Particle-Based Delivery System for Oncotherapy”. *Nanoscale* 11.6 (2019). DOI: `10.1039/c8nr09990a` (cit. on pp. 38–40, 131).

[Wisc2020] C. Wischnewski and J. Kierfeld. “Snapping Elastic Disks as Microswimmers: Swimming at Low Reynolds Numbers by Shape Hysteresis”. *Soft Matter* 16.30 (2020). DOI: `10.1039/d0sm00741b` (cit. on p. 62).

[Wolf2020] H. J. M. Wolff et al. “Soft Temperature-Responsive Microgels of Complex Shape in Stop-Flow Lithography”. *Lab on a Chip* 20.2 (2020). DOI: `10.1039/c9lc00749k` (cit. on pp. 6, 7, 9, 38, 39, 41, 43, 70, 95, 106).

[Wolf2021] H. J. M. Wolff. “Fabrication of Tailored Microgels in Continuous Processes”. Dissertation. RWTH Aachen University, 2021 (cit. on pp. 5, 9–12, 102).

[Xia1998] Y. Xia and G. M. Whitesides. “Soft Lithography”. *Angewandte Chemie, International Edition* 37.5 (1998). DOI: `10.1002/(SICI)1521-3773` (cit. on p. 42).

[Xion2022] Y. Xiong et al. “Recent Progress on Microfluidic Devices with Incorporated 1D Nanostructures for Enhanced Extracellular Vesicle (EV) Separation”. *Bio-Design and Manufacturing* 8.19 (2022). DOI: `10.1007/s42242-022-00195-2` (cit. on p. 90).

[Xu2013] J. Xu et al. “Future of the Particle Replication in Nonwetting Templates (PRINT) Technology”. *Angewandte Chemie, International Edition* 52.26 (2013). DOI: `10.1002/anie.201209145` (cit. on p. 24).

[Xue2017] B. Xue, V. Kozlovskaya, and E. Kharlampieva. “Shaped Stimuli-Responsive Hydrogel Particles: Syntheses, Properties and Biological Responses”. *Journal of Materials Chemistry B* 5.1 (2017). DOI: `10.1039/c6tb02746f` (cit. on p. 62).

[Yang2010] C. Yang et al. “Preparation of Monodisperse Magnetic Polymer Microspheres by Swelling and Thermolysis Technique”. *Langmuir* 26.7 (2010). DOI: `10.1021/la903659z` (cit. on pp. 19, 66).

[Yavi2022] F. M. Yavitt et al. “4D Materials with Photoadaptable Properties Instruct and Enhance Intestinal Organoid Development”. *ACS Biomaterials Science & Engineering* 8.11 (2022). DOI: `10.1021/acsbiomaterials.1c01450` (cit. on p. 91).

[Yazd2020] M. K. Yazdi et al. “Hydrogel Membranes: A Review”. *Materials Science and Engineering: C* 114 (2020). DOI: `10.1016/j.msec.2020.111023` (cit. on p. 90).

[Yin2022] J. Yin et al. “Precisely Defining Local Gradients of Stimuli-Responsive Hydrogels for Complex 2D-to-4D Shape Evolutions”. *Small* 18.2 (2022). DOI: `10.1002/smll.202104440` (cit. on p. 62).

[Yong2022] H. Yong and J.-U. Sommer. “Cononsolvency Effect: When the Hydrogen Bonding between a Polymer and a Cosolvent Matters”. *Macromolecules* 55.24 (2022). DOI: `10.1021/acs.macromol.2c01428` (cit. on p. 40).

[Yoon2020] J. Yoon and W. Park. “Microsized 3D Hydrogel Printing System Using Microfluidic Maskless Lithography and Single Axis Stepper Motor”. *BioChip Journal* 14.3 (2020). DOI: `10.1007/s13206-020-4310-4` (cit. on pp. 25, 26).

[Zhan2017] H. Zhang, A. Mourran, and M. Möller. “Dynamic Switching of Helical Microgel Ribbons”. *Nano Letters* 17.3 (2017). DOI: `10.1021/acs.nanolett.7b00015` (cit. on p. 62).

[Zhan2018] H. Zhang et al. “Soft Mechanical Metamaterials with Unusual Swelling Behavior and Tunable Stress-Strain Curves”. *Science Advances* 4.6 (2018). DOI: `10.1126/sciadv.aar8535` (cit. on p. 62).

[Zhou2022] C. Zhou et al. “Tailoring 3D Shapes of Polyhedral Milliparticles by Adjusting Orthogonal Projection in a Microfluidic Channel”. *Journal of Polymer Science* 60.11 (2022). DOI: `10.1002/pol.20210953` (cit. on p. 25).

Appendix

Porous Structure Modification for Tuned Thermal Behavior

Table 1: Length in the swollen and collapsed state of microgels fabricated with varying methanol contents (0-50 wt%) in the reaction solution. The collapsing degree arises from the length difference between the states (swollen length - collapsed length) divided by the length in the swollen state.

Methanol content [wt%]	Swollen length [µm]	Collapsed length [µm]	Collapsing degree [%]
0	98.4 ± 2.0	50.1 ± 2.8	49.0 ± 3.8
10	99.2 ± 6.5	53.1 ± 2.5	46.5 ± 5.3
20	97.4 ± 3.4	53.7 ± 2.2	44.8 ± 3.4
30	102.9 ± 5.0	41.2 ± 1.8	60.0 ± 5.5
40	126.7 ± 12.9	38.9 ± 3.9	69.3 ± 14.1
50	153.2 ± 10.0	36.6 ± 3.7	76.1 ± 12.6

Table 2: Width and aspect ratio of swollen and collapsed microgels as a function of their methanol content (0-50 wt%) during fabrication. The aspect ratio is calculated as length divided by width of the microgels.

Methanol content [wt%]	Swollen width [µm]	Collapsed width [µm]	Swollen aspect ratio [-]	Collapsed aspect ratio [-]
0	33.6 ± 1.5	16.6 ± 0.6	2.9 ± 0.2	3.0 ± 0.3
10	35.4 ± 1.4	19.4 ± 1.8	2.8 ± 0.3	2.7 ± 0.4
20	34.5 ± 1.3	18.2 ± 1.0	2.8 ± 0.2	3.0 ± 0.3
30	34.4 ± 1.2	15.0 ± 4.2	3.0 ± 0.3	2.7 ± 0.9
40	38.3 ± 1.6	11.8 ± 1.2	3.3 ± 0.5	3.3 ± 0.7
50	38.3 ± 2.6	6.7 ± 2.2	4.0 ± 0.5	5.5 ± 2.4

Table 3: Maximum velocities during collapsing and swelling of microgels depending on the methanol content (0-50 wt%) during fabrication. The acceleration factor shows to which extent the swelling is faster than the collapsing for the respective sample by dividing swelling by collapsing velocity.

Methanol content [wt%]	Maximum collapsing [µm/s]	Maximum swelling [µm/s]	Acceleration factor [-]
0	0.51 ± 0.10	1.51 ± 0.42	2.95 ± 1.38
10	0.22 ± 0.03	1.19 ± 0.31	5.43 ± 2.26
20	0.41 ± 0.03	0.97 ± 0.31	2.38 ± 0.92
30	0.61 ± 0.08	1.48 ± 0.72	2.42 ± 1.49
40	0.87 ± 0.22	3.19 ± 1.25	3.64 ± 2.37
50	0.96 ± 0.28	3.90 ± 2.10	4.06 ± 3.36

Magnetic Actuation for Controlled Motion

Table 4: Mean critical rotation rates ω_C of all complex-shaped microgels investigated in Section 3.3.2 towards free rotation in an applied magnetic field. Impeller-shaped microgels have a contact surface area of 1048 ± 21 μm^2 and a volume of 97000 ± 2000 μm^3, whereas the snowflake-shaped microgels have a 2.0 times larger surface area of 2138 ± 164 μm^2 and a 1.8 times larger volume of 178000 ± 14000 μm^3.

Microgel shape [-]	Maghemite content [wt%]	Field strength [mT]	Critical rotation rate [rpm]
Impeller	0.02	68	21.5 ± 2.3
	0.08		32.2 ± 1.8
	0.16		34.2 ± 2.8
Impeller	0.08	6	5.3 ± 0.3
		36	22.2 ± 1.3
		68	32.2 ± 1.8
Impeller	0.08	68	32.2 ± 1.8
Snowflake			79.8 ± 3.2

Patterned Crosslinking for Designed Architecture

Patch Overview

Table 5 gives an overview of all patch types, listing the dimensions of the used mask and within the patches. These dimensions vary by factor 5.46 as the optic-related characteristical value of the used SFL setup. The spot distances are indicated as center-to-center distances apart from specially labeled values that additionally indicate edge-to-edge distances. All mentioned patch types in Table 5 were fabricated out of PNIPAM. PEGDA patches were investigated with regard to their formation and cell cultivation, comprising the following patch types: *circle (7 µm)/ w/o pore*, *circle*

Table 5: Patch overview of all addressed patch dimensions. Distances are indicated as center-to-center distances of the respective spots apart from specially labeled values that additionally indicate edge-to-edge distances.

Patch type	Spot shape	Spot arrangement	Spot diameter [µm] (mask/ patch)	Spot distance [µm] (mask/ patch)	Proportion of HC regions [%]
Circle (7 µm)/ w/o Pore	circle	hexagonal	40 / 7	140 / 26 edge: 100/ 18	7
Circle D90	circle	hexagonal	40 / 7	90 / 16 edge: 50/ 9	18
Circle D240	circle	hexagonal	40 / 7	240 / 44 edge: 200/ 37	3
Circle d30	circle	hexagonal	30 / 5	130 / 24 edge: 100/ 18	5
Circle d60	circle	hexagonal	60 / 11	160 / 29 edge: 100/ 18	13
Circle (52 µm)	circle	hexagonal	282 / 52	382 / 70	49
Square	square	hexagonal	250 / 46	382 / 70	49
Snowflake	snowflake	hexagonal	270 / 50	382 / 70	49
Star	star	hexagonal	380 / 70	382 / 70	49
44 µm Pore	circle	hexagonal	40 / 7	140 / 26	4
95 µm Pore	circle	hexagonal	40 / 7	140 / 26	7
hor Line	rectangle	linear	40 / (2250 x) 7	140 / 26	29
ver Line	rectangle	linear	40 / 7 (x 900)	140 / 26	29
Reference	-	-	-	-	100

(52 µm), *reference*, and *95 µm pore*. The patches are classified according to their geometry and the associated investigations. The *circle (7 µm)/ w/o pore* patch serves as the basic patch type. The patches of the *formation* groups were used to identify the ideal spot distance to diameter ratio by adapting either the distance or the diameter of the circle-shaped spots. The group *structure* consists of four patch types that all have the same irradiated surface area, resulting in equal areas of highly crosslinked (HC) and low crosslinked (LC) regions. The *porosity* group compares the effect of

patches' third level of porosity. The last patch group concerns the induced *directionality* of patches.

Patch Pipette Aspiration

Pipette Aspiration Experimentals For the pipette aspiration experiments, a single patch was transferred onto a microscope slide (26 x 76 x 1 mm, VWR) within a water droplet. The slide was placed under an inverse light microscope (DM IL LED, Leica), and a high-speed camera (Phantom VEO 640 L, Metek) was mounted to record the experiments. For aspiration of the patch, a pipette tip was wetted with a tween-20 solution (5 v%), placed over the sedimentated patch, and aspirated it.

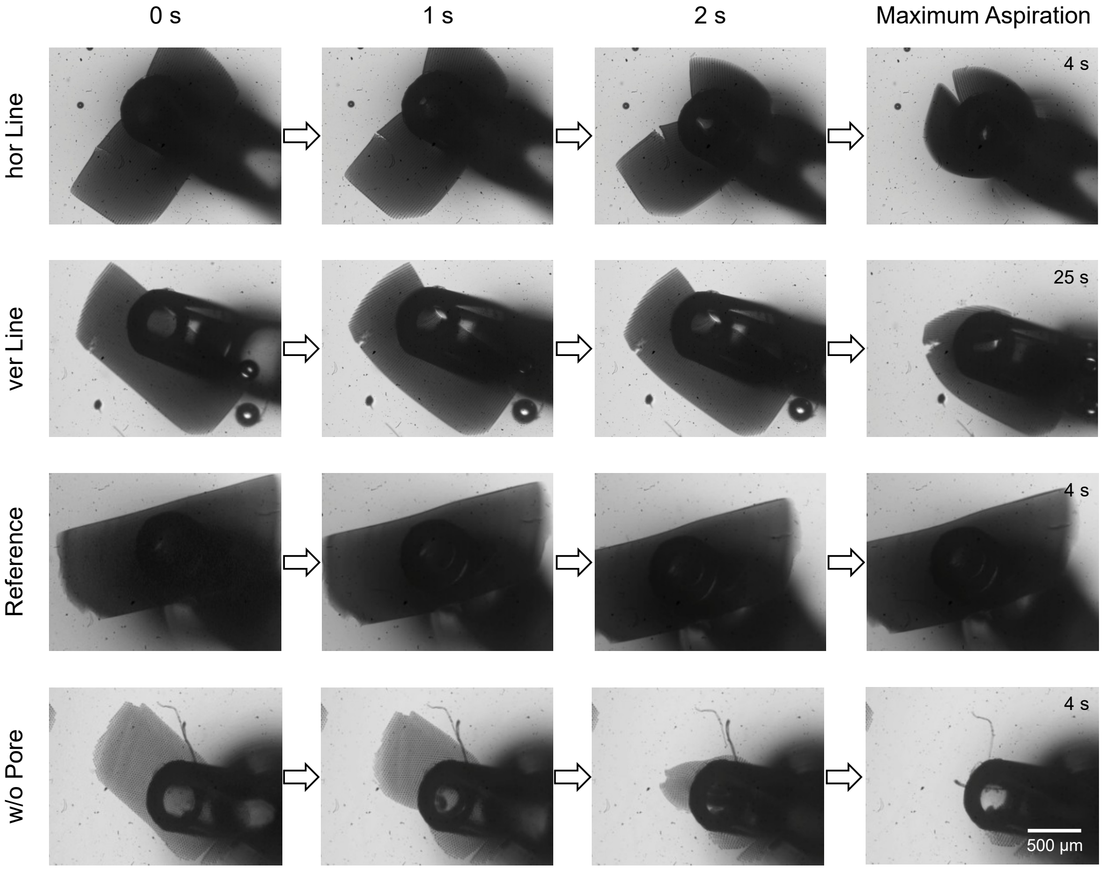

Figure 1: Pipette aspiration of all *directionality* group patches and the basic patch type *circle (7 µm)/ w/o pore*, showing their folding capability and flexibility. Scale bar (500 µm) applies to all images.

Compression

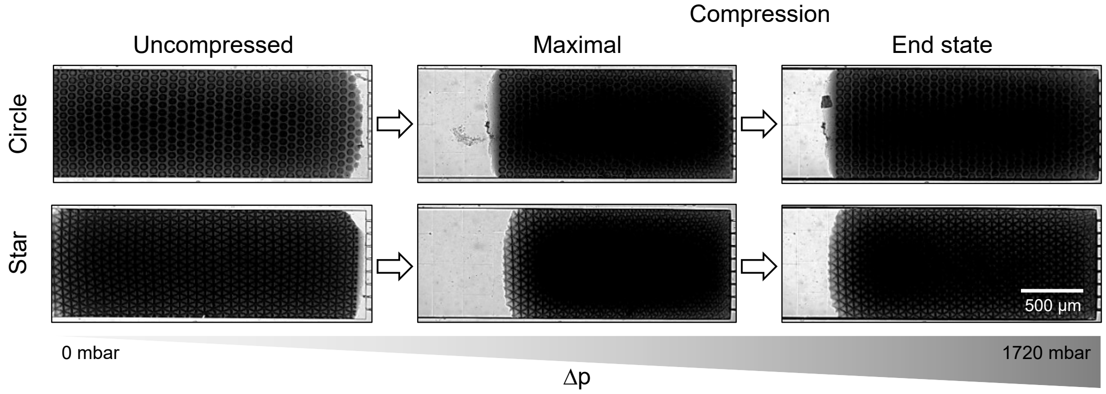

Figure 2: Compression states of the *structure* patch types *circle* and *star*. Scale bar (500 µm) applies to all images.

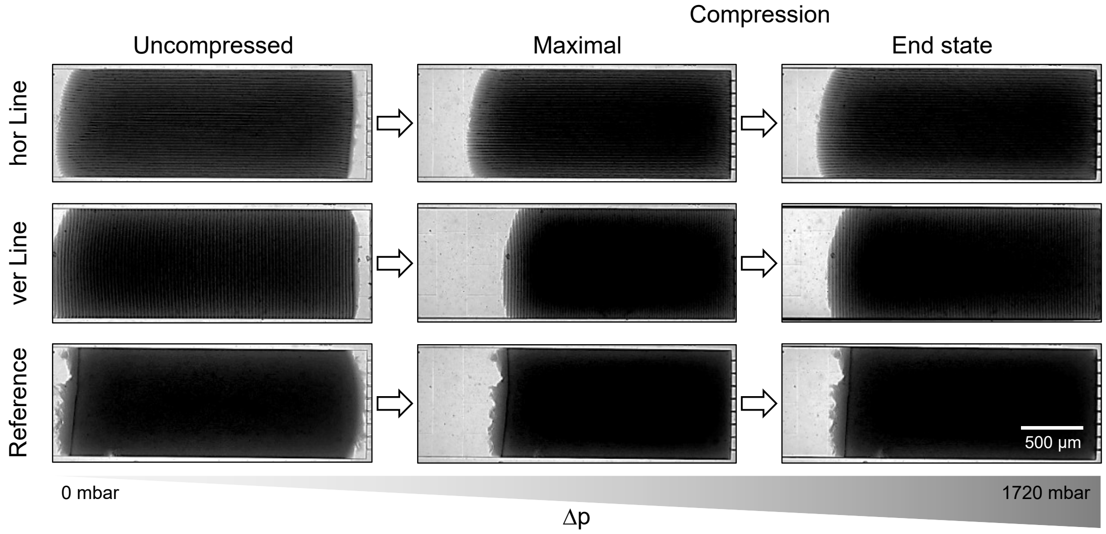

Figure 3: Compression states of the *directionality* patch types *hor line*, *ver line*, and *reference*. Scale bar (500 µm) applies to all images.

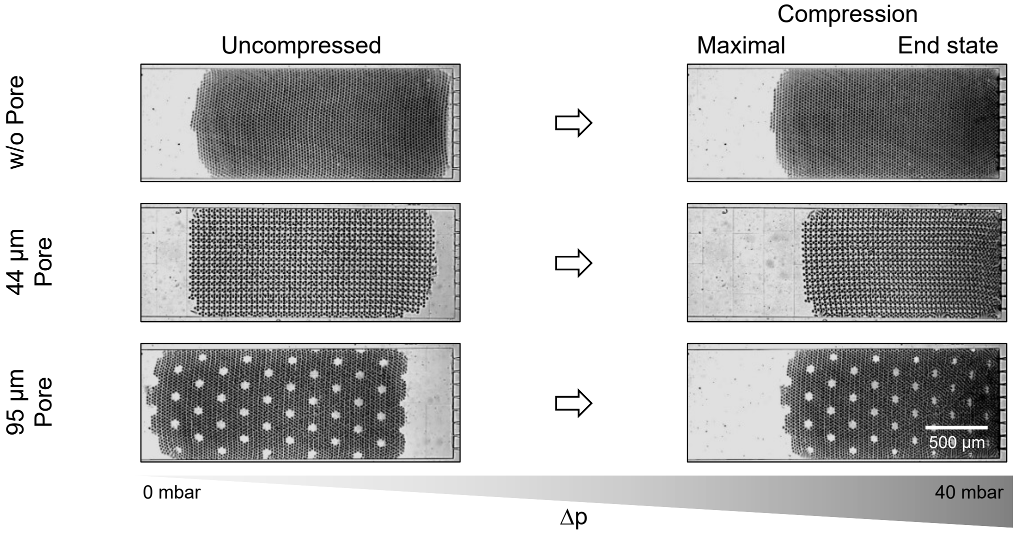

Figure 4: Compression states of the *porosity* patch types *w/o pore*, *44 µm pore*, and *95 µm pore*. The maximal and the end state compression are equal for these patch types. Scale bar (500 µm) applies to all images.

Table 6: Compression values.

	Maximum compression		End state compression		Reversion
Patch type [-]	Applied pressure [mbar]	Normalized surface area [-]	Applied pressure [mbar]	Normalized surface area [-]	Reversed surface area [-]
Circle	932 ± 293	0.80 ± 0.04	1721 ± 0	0.84 ± 0.03	0.27 ± 0.08
Star	881 ± 285	0.74 ± 0.04	1719 ± 1	0.82 ± 0.04	0.30 ± 0.13
hor Line	675 ± 62	0.82 ± 0.05	1720 ± 0	0.93 ± 0.02	0.59 ± 0.12
ver Line	926 ± 471	0.79 ± 0.07	1720 ± 1	0.85 ± 0.05	0.39 ± 0.12
Reference	900 ± 428	0.79 ± 0.07	1720 ± 1	0.84 ± 0.08	0.48 ± 0.07
w/o Pore	39.6 ± 0.6	0.83 ± 0.06	39.6 ± 0.6	0.83 ± 0.06	-
44 µm P.	39.7 ± 0.5	0.80 ± 0.05	39.7 ± 0.5	0.80 ± 0.05	-
95 µm P.	40.5 ± 0.5	0.86 ± 0.03	40.5 ± 0.5	0.86 ± 0.03	-

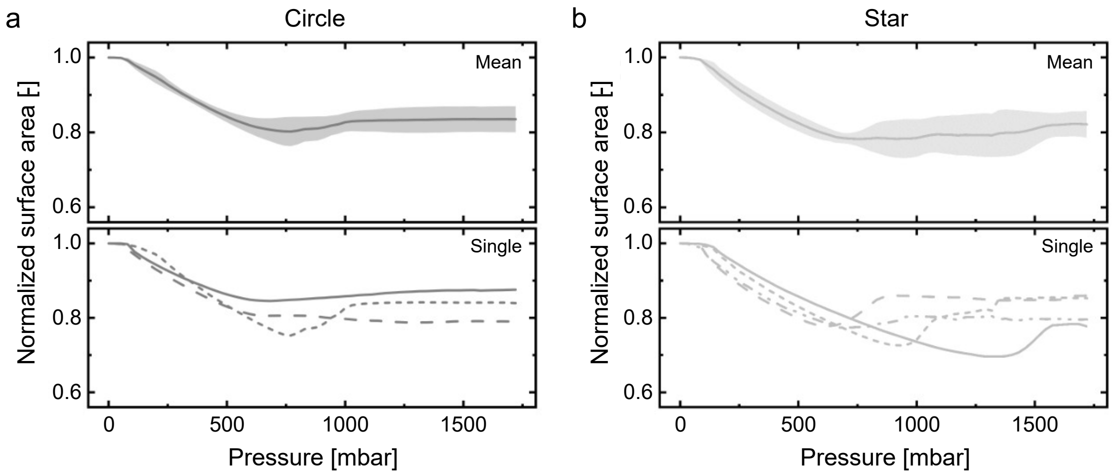

Figure 5: Single compression curves of all investigated (a) *circle* and (b) *star* patches and their respective means.

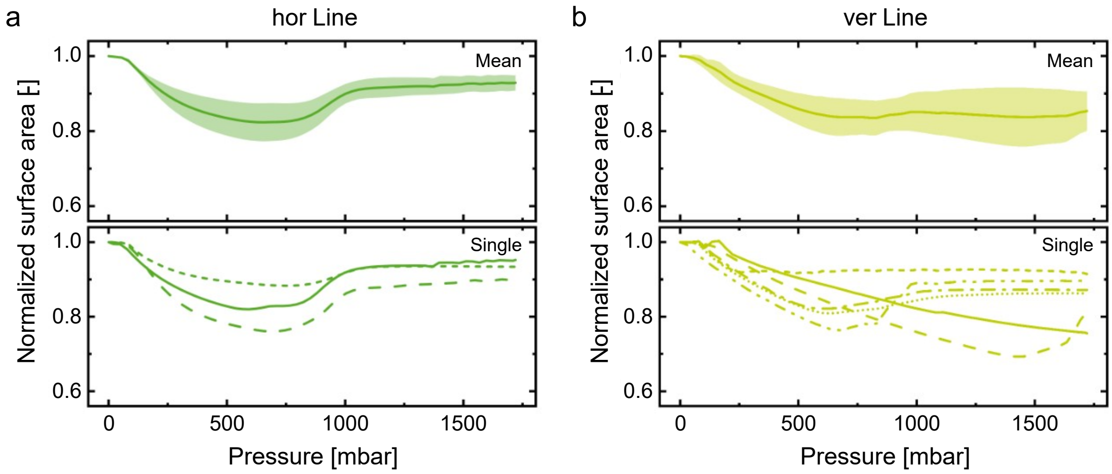

Figure 6: Single compression curves of all investigated (a) *hor line* and (b) *ver line* patches and their respective means.

Squeezing

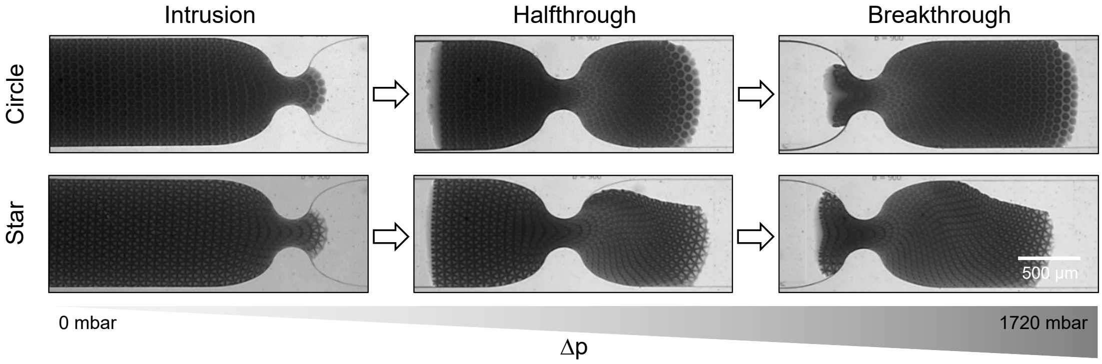

Figure 7: Squeezing states of the *structure* patch types *circle* and *star*. Scale bar (500 µm) applies to all images.

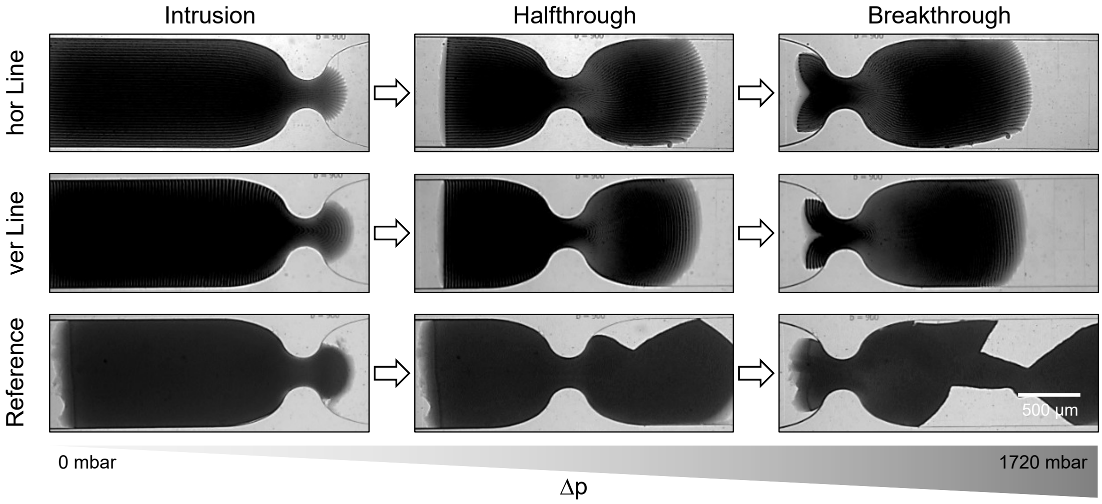

Figure 8: Squeezing states of the *directionality* patch types *hor line*, *ver line*, and *reference*. Scale bar (500 µm) applies to all images.

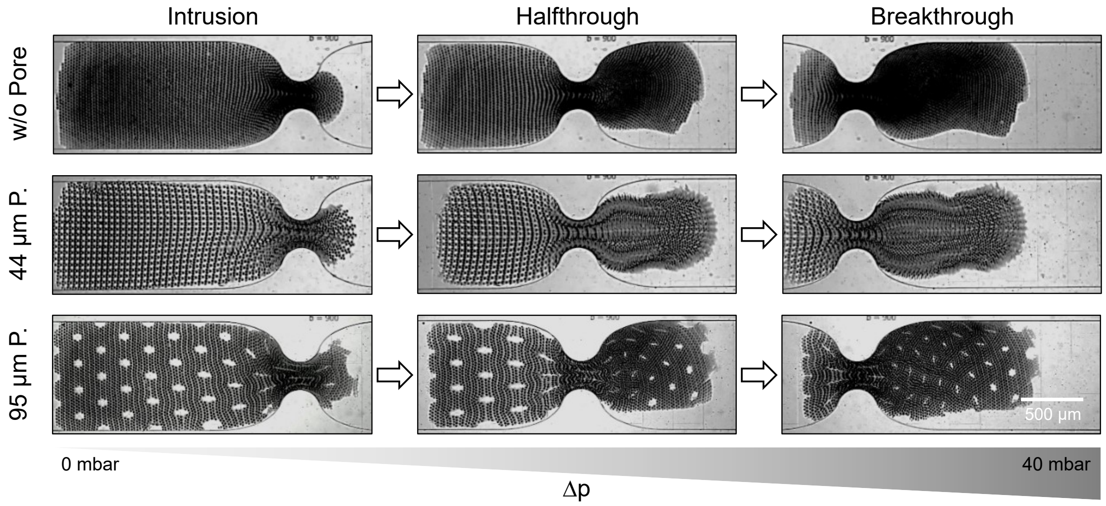

Figure 9: Squeezing states of the *porosity* patch types *w/o pore*, *44 µm pore*, and *95 µm pore*. Scale bar (500 µm) applies to all images.

Table 7: Squeezing values. The relative time and pressure between the halfthrough and the breakthrough states arise from dividing the halfthrough through the breakthrough value each. A value of 1 equals similar values for both states, and the lower the relative value, the higher the difference in pressure or time between these states.

			Half- vs. Breakthrough	
Patch type [-]	Halfthrough pressure [mbar]	Breakthrough pressure [mbar]	Relative time [-]	Relative pressure [-]
Circle	1690 ± 25	1719 ± 2	0.67 ± 0.15	0.98 ± 0.01
Star	899 ± 49	1001 ± 47	0.89 ± 0.01	0.90 ± 0.02
hor Line	1605 ± 143	1682 ± 55	0.95 ± 0.06	0.95 ± 0.06
ver Line	1302 ± 110	1531 ± 137	0.85 ± 0.06	0.85 ± 0.05
Reference	1716 ± 0	1717 ± 0	0.88 ± 0.00	1.00 ± 0.00
w/o Pore	8.6 ± 1.2	8.4 ± 1.2	0.89 ± 0.01	1.02 ± 0.06
44 µm P.	4.4 ± 1.6	4.6 ± 1.9	0.90 ± 0.02	0.97 ± 0.09
95 µm P.	8.6 ± 1.1	9.3 ± 1.3	0.94 ± 0.02	0.93 ± 0.04

Cell Cultivation

Table 8: Cell cultivation values.

Patch material [-]	Patch type [-]	Cell area [µm^2]	Eff. Young's modulus [kPa]
PEGDA	Circle 7 µm	331 ± 144	1.0 ± 0.6
	Circle 52 µm	717 ± 263	-
	Reference	1173 ± 271	30.2 ± 1.8
	No patch	1987 ± 860	-
PNIPAM	Circle 7 µm	916 ± 248	-
	Circle 52 µm	1046 ± 597	8.4 ± 1.3
	Reference	1116 ± 415	14.6 ± 0.6
	No patch	1637 ± 488	-

DOI: 10.18154/RWTH-2025-03604

Aachener
Verfahrenstechnik

RWTH AACHEN UNIVERSITY